Correlated Many-Electron Phenomena in the Quantum Hall Regime:

Electronic Liquid-Crystal Phases and Spin Phase Transition

Dissertation
zur Erlangung des Doktorgrades
des Fachbereichs Physik
der Universität Hamburg

vorgelegt von

Gerardo Gamez-Corrales
aus Hermosillo, Mexico

Hamburg
2007

Gutachter der Dissertation:

Prof. Dr. Klaus von Klitzing

Prof. Dr. Daniela Pfannkuche

Gutachter der Disputation:

Prof. Dr. Klaus von Klitzing

Prof. Dr. Detlef Heitmann

Datum der Disputation:

24. September 2007

Vorsitzender des Prüfungsausschusses:

Dr. Alexander Chudnovskiy

Vorsitzender des Promotionsausschusses:

Prof. Dr. Günter Huber

MIN-Dekan der Fakultät des Departments Physik:

Prof. Dr. Arno Frühwald

Abstract

Electrons confined to two dimensions, cooled down to millikelvin temperatures and subjected to a strong perpendicular magnetic field form some of the most remarkable collective states of matter. In this dissertation, we have carried out local probe and transport studies on collective phenomena associated with two of these exotic states induced by strongly interacting electrons. The collective phenomena studied are: (a) The electronic liquid-crystal phases that emerge in partially filled high Landau levels ($N \geq 2$). (b) The spin phase transition that occurs at filling factor $\nu = 2/3$.

The correlated phases in high Landau levels, which are responsible for reentrant integer Hall quantization and anisotropic transport, were studied in transport under non-equilibrium conditions by imposing a dc current drive. In these studies, we have observed that the dc drive has a stabilizing influence on the orientation of the anisotropic phase at half-filling if dc-drive and easy direction coincide, while the easy-direction of conduction is rotated to point along the direction of the dc-current otherwise. At quarter fillings, the dc drive induces anisotropic transport behavior consistent with stripe order. Furthermore, we have observed that this emergent anisotropic phase also undergoes a current induced reordering. Initially, dc-drive and easy direction are perpendicular, but with increasing drive they align.

Using a single-electron transistor, we studied the spin phase transition at filling $\nu = 2/3$. In these studies, we were able to follow the evolution of localized states across the first-order spin transition by measuring the local electronic compressibility. Localized-state spectra reveal the hysteretic behaviour accompanying the transition. This hysteresis is due to the formation of domains of different spin polarization. Using electrostatic gating we varied the size of the sample undergoing the phase transition. For submicrometer dimensions the hysteresis disappears, indicating domain sizes in excess of 500 μm.

Zusammenfassung

Zweidimensionale Elektronengase unter starken senkrechten Magnetfeldern und Temperaturen von einigen Milli-Kelvin bilden infolge der starken Wechselwirkung untereinander bemerkenswerte kollektive Zustände aus. In dieser Dissertation wurden zwei dieser exotischen Phänomene untersucht: 1. die elektronischen flüssig-kristallinen Phasen, bei teilgefüllten, höherzahligen Landau Niveaus ($N \geq 2$), 2. der Spin-Phasenübergang, bei Füllfaktor $\nu = 2/3$.

Die korrelierten Phasen bei höheren Füllfaktoren, die eine wiederkehrende ganzzahlige Hall-Quantisierung zeigen wurden mittels DC-Transportmessungen unter Nichtgleichgewichtsbedingungen untersucht. Bei diesen Experimenten konnten wir beobachten, dass der Gleichstrom eine stabilisierende Wirkung auf die Ausrichtung der anisotropen Phase bei halbem Füllfaktor hat, sofern Strom- und Vorzugsrichtung von vorneherein übereinstimmen, anderenfalls kommt es zu einer Ausrichtung der Vorzugsrichtung entlang der Stromrichtung. Bei Füllfaktoren von 1/4 induziert der Gleichstrom ein anisotropes Transportverhalten, was für die "stripe order" zu erwarten ist. Diese auftretende anisotrope Phase zeigte ferner eine durch den Anregungsstrom induzierbare Neuorientierung. Während Stromrichtung und Vorzugsrichtung bei kleinen Anregungsströmen noch orthogonal zueinander ausgerichtet sind, kommt es bei einer Erhöhung des Stromes zu einer Parallelisierung beider Richtungen.

Unter Verwendung von Einzelelektronentransistoren wurde der Spin-Phasenübergang bei ν=2/3 untersucht. Aus der Messung der lokalen Elektronen-Kompressibilität konnte die Entwicklung der lokalisierten Zustände über den Spin-Phasenübergang der 1. Ordnung hinweg nachvollzogen werden. Die Spektren der lokalisierten Zustände zeigen deutlich das Hystereseverhalten während des Phasenüberganges, als Folge der Ausbildung von Domänen mit unterschiedlicher Spin-Polarisation. Die effektive Probengröße konnte durch Gatter variiert werden. Dabei wurde beobachtet, dass die Hysterese im Submicrometer-Bereich verschwindet, was eine Domänengröße von mehr als $500\mu m$ bedeutet.

Contents

Symbols and Abbreviations

ac	alternating current.
a.u.	arbitrary units.
B	External magnetic field.
B^*	Effective magnetic field experienced by CFs.
CDW	Charge Density Wave.
CF	Composite Fermion.
CF-LL	Composite fermion Landau levels.
dc	direct current.
e	Electron charge.
ϵ	Dielectric function of the background material.
ELC	Electron Liquid Crystal.
E_Z	Zeeman energy.
E_F	Fermi energy.
FQHE	Fractional Quantum Hall Effect.
$\hbar\omega_C$	Cyclotron energy.
I	Electrical current.
IQHE	Integer Quantum Hall Effect.
LL	Landau level.
LLL	Lowest Landau level.
ℓ	Magnetic length ($\ell = \sqrt{\hbar/eB}$).
m_b	Electron band mass ($m_b = 0.067m_e$ in GaAs).
m_e	Electron mass in vacuum.
MBE	Molecular Beam Epitaxy.

N	Landau level index.
NMR	Nuclear magnetic resonance.
ν	Filling factor of electrons.
ν^*	Filling factor of composite fermions.
Φ_0	Elementary magnetic flux quanta ($\Phi_0 = h/e$).
QHR	Quantum Hall Regime.
R_H	Hall resistance.
R_K	The von Klitzing constant ($R_K = h/e^2$).
R_L	Longitudinal resistance.
RIQHE	Reentrant Integer Quantum Hall Effect.
SET	Single Electron Transistor.
T	Temperature.
2D	Two-dimensional.
2DES	Two-dimensional electron system.
V_C	Coulomb energy.
V_L	Longitudinal voltage.
V_H	Hall voltage.
vdP	van der Pauw.
ω_C	Cyclotron frequency.
z	Position in 2D ($z = x + iy$).

Chapter 1

Introduction

The collective behavior of electrons in a two-dimensional system is a fundamental issue in condensed matter physics. In the past 25 years, studies on the behavior of electrons confined in a two-dimensional plane have revealed a plethora of new physical phenomena associated with correlated many-electron states that emerge due to the strong electron-electron interactions. Preeminent among these phenomena is the fractional quantum Hall effect; a quantum phenomenon that is the result of the condensation of a collection of electrons into a new state of matter. Their discovery and explanation in the early 1980s [1, 2] marked the beginning of a new era in the field of the strongly correlated electron systems. Nowadays, investigations on ultra clean two-dimensional electron systems subjected to a perpendicular magnetic field and cooled down to millikelvin temperatures continue to disclose some of the most exotic collective state of matter [3, 4].

The remarkable diversity of collective states that emerge in the quantum Hall regime have turned the 2DES into a fascinating playground to investigate fundamental electron-electron interactions. The prominent manifestation of electronic interactions in a 2DES subjected to a perpendicular magnetic field is due to the massive degeneracy of the Landau levels that form when the kinetic energy becomes quantized. This quenching of the kinetic energy makes the system particularly susceptible to Coulomb correlations. The collective phenomena most intensively studied are those associated with the fractional quantum Hall states. These states correspond to incompressible quantum liquids with fractionally charged excitations, that exhibit the fractional quantum Hall effect [5]. Another important collective ground states that emerge in the quantum Hall regime is the Wigner crystal [6, 7]. In this state the electrons arrange themselves on the vertices of a triangular lattice. Recently there has been evidence

also for the existence of exotic phases that resemble liquid crystals [8].

In this work I will present experiments in which we have explored two different classes of correlated many-electron states in the quantum Hall regime: the electronic liquid-crystal phases that emerge when more than two Landau levels are populated and the fractional quantum Hall state at filling $2/3$ of the lowest Landau level which undergoes a spin phase transition. Although the origin of these two collective phenomena are distinct, they have a common characteristic. Two or more electronic phases coexist and compete resulting in charge pattern or domain formation. These patterns and domains are formed by the charge [8] and spin [9] degrees of freedom and stabilized by competing interactions.

Most studies focusing on electron-electron correlation effects in 2DES have been done at sufficiently high magnetic fields so that only the lowest Landau level is partially filled, i.e., the degeneracy of the Landau level is such that it can accommodate all the electrons. In this so-called extreme quantum limit the most pronounced fractional quantum Hall states occur. These states have been the source of a tremendous amount of interesting physics. Recently the physics in the extreme quantum limit has been enriched further by paying close attention to the internal spin degree of freedom [10]. In the fractional quantum Hall regime some ground states differ only in the configuration of the electron spins, which is determined by the interplay between the Coulomb and Zeeman energies. Under certain conditions, a spin-unpolarized fractional quantum Hall state competes in energy with the spin-polarized fractional quantum Hall state. Spin phase transitions can occur between unpolarized, partially polarized, and fully spin-polarized fractional quantum Hall liquids. Our studies focus on the spin phase transition that occurs at filling factor $\nu = 2/3$. It is believed that such a transition is accompanied by domain formation of different spin orientation separated by domain walls. In many aspects, this transition resembles a ferromagnetic first order phase transition. To date, the ferromagnetic character of the spin phase transition has been revealed through hysteretic behavior in macroscopic transport experiments. In this work, we use a single electron transistor to measure the local compressibility and explore this transition from a microscopic point of view.

Fractional quantum Hall states do not only occur in the partially filled lowest $N = 0$ Landau level. Also in the second $N = 1$ Landau level a number of fractional quantum Hall states have been observed [11, 12]. Naively, one might expect similar behavior for higher $N \geq 2$ Landau levels as for the partially filled lowest Landau level, since we usually consider

completely filled lower lying Landau levels as forming an inert background. However this is incorrect. Recent transport studies on state-of-the-art samples have disclosed new collective states in high index Landau levels [13, 14]. These states are quite distinct from the fractional quantum Hall states. Among the main findings of these states are strong anisotropies in the resistivity near half-filling of these higher Landau levels and the observation of re-entrant Hall quantization around quarter-fillings. Although the precise nature of these phases is still unclear, they are believed to be charge density waves exhibiting different long range ordered density patterns [15]: stripes and multi-electron bubbles. The coexistence of a partially filled high index Landau levels with multiple completely filled lower lying Landau levels, modifies the balance between the repulsive and the attractive components of the Coulomb interaction, so that Laughlin-like states [2] are no longer the favoured ground state of the system. The system prefers to break up into domains composed of a mixture of the two adjacent integer fillings instead of condensing into a fractional quantum Hall liquid. The morphology of these charge density patterns depends on the filling of the partially filled level. Near half filling, the pattern consists of stripes of alternating integer filling. Near one and three-quarter fillings, a bubble phase emerges made up of bubbles of one integer filling, immersed in a sea of the other integer filling. The bubbles form triangular crystal similar to the Wigner crystal. The stripe morphology accounts for anisotropies in the resistivity, whereas re-entrant Hall quantization is expected for the bubble phase. A more sophisticated model describes these states more accurately as quantum liquid crystal phases [8]. This model takes into account quantum fluctuations in the system. The electronic liquid-crystal states are classified according to the symmetries they fulfil: smectic phase, nematic phase, stripe crystal, and isotropic liquid phases. In order to improve our understanding of these correlated phases, we have studied these phases in transport under non-equilibrium conditions by imposing a dc current drive. The additional dc current modifies these phases in a controlled manner allowing us to gain a better insight into their nature and properties.

1.1 Organization of this thesis

This thesis comprises six chapters:

Chapter two surveys some important concepts pertaining to the quantum Hall regime. The two-dimensional electron system is introduced. A brief introduction to the integer and

fractional quantum Hall effects is presented. A recent model of localization in the quantum Hall regime, which includes Coulomb interaction is also presented.

Chapter three presents the technical background needed to carry out the experiments. Section 3.1 describes the sample design as well as the geometry of the devices used in these studies. Subsequently, the transport and local probe techniques are described in sections 3.2 and 3.3 respectively.

Chapter four is devoted to the correlated phases in high index Landau levels. An overview of the main experimental evidence for the existence of these phases is presented and described in the first section. The charge-density-wave and the electron liquid-crystal models are introduced in section 4.2. The main results of this chapter come from a study of these phase under non-equilibrium conditions by imposing a dc current drive. The remainder of this chapter presents evidence consistent with current induced anisotropy and reordering of the electron liquid crystal phases.

Chapter five presents results on the spin phase transition at filling factor $\nu = 2/3$ using a local probe technique. With a stationary single-electron transistor the localized states across the spin are investigated. In the first section a brief introduction to the physics of the spin transition as well as experimental evidence from transport studies for its existence is presented. Section 5.3 presents the microscopic manifestation of this first-order spin phase transition. The phase transition is accompanied by hysteresis as shown in section 5.4. Finally, in section 5.5 the typical domain size is estimated.

Chapter six summarizes the main findings of the research performed in this dissertation.

Appendix A presents details of the sample fabrication.

Chapter 2

The Quantum Hall Regime

A two-dimensional electron system exhibits the quantum Hall regime when it is subjected to a strong perpendicular magnetic field, and cooled down to kelvin temperatures[1]. The electrons under these conditions are mathematically described by the Hamiltonian [17]

$$H = \sum_j \frac{1}{2m_b}\left[\frac{\hbar}{i}\nabla_j + e\vec{A}(\vec{r_j})\right]^2 + \frac{e^2}{\epsilon}\sum_{j<k}\frac{1}{|\vec{r_j}-\vec{r_k}|} + \sum_j U(\vec{r_j}) + g\mu_B\vec{B}\cdot\vec{S} \tag{2.1}$$

The first term on the right side is the kinetic energy in the presence of a constant external magnetic field $\vec{B} = \nabla \times \vec{A}$, the second term is the Coulomb interaction energy, the third term is a potential that incorporates the effects of the uniform positive background and disorder, and the last term corresponds to the Zeeman energy. Due to the applied magnetic field, the kinetic energy of the 2D electrons is quenched and the energy spectrum is converted into a ladder of massively degenerate Landau levels, each separated by the cyclotron energy gap.

The physics in the quantum Hall regime is governed by the competition between these four energy scales. Apart from the energy scale introduced by the disorder potential, these energies are as follows for GaAs based 2DES:
the cyclotron energy

$$\hbar\omega_C = \hbar\frac{eB}{m_b} \approx 20B[T]K, \tag{2.2}$$

the Coulomb energy

$$V_C \equiv \frac{e^2}{\epsilon\ell} \approx 50\sqrt{B[T]}K, \tag{2.3}$$

[1]Recently, the quantum Hall effect was observed at room temperature in graphene [16]

the Zeeman energy

$$E_Z = 2g\mu_B \vec{B} \cdot \vec{S} = \frac{g}{2}\frac{m_b}{m_e}\hbar\omega_C \approx 0.3B[T]K \tag{2.4}$$

The Zeeman energy is defined as the energy required to flip a spin. μ_B is the Bohr magneton $\mu_B = e\hbar/2m_b$.

Equations 2.2-2.4 give the energy in Kelvin (K), with B[T] in Tesla (T). Here, the following values were used: band mass of electrons $m_b = 0.067m_e$ (m_e is the electron mass in vacuum); dielectric constant $\epsilon = 12.6$; Landé g-factor $g = -0.44$. Another relevant parameter in the quantum Hall regime is the magnetic length, ℓ_B, which is defined as:

$$\ell_B = \left(\frac{\hbar}{eB}\right)^{1/2} \approx \frac{25}{\sqrt{B[T]}}nm. \tag{2.5}$$

The present chapter attempts to introduce the basic elements required to understand some of the most relevant concepts in the quantum Hall regime. This, in turn, serves as an introduction for chapters 4 and 5, which describe experiments carried out in the limit where the Coulomb interaction energy dominates.

2.1 Preliminaries

2.1.1 Two-Dimensional Electron Systems

A two-dimensional electron system (2DES) is created by confining electrons to a plane using a suitable confinement potential [18]. In these systems, electrons can move along the plane but are bound to it in the perpendicular direction. In practice, there are several ways to place electrons in a plane, but the most adequate for studying correlation effects is to confine the electrons to an interface between two crystalline semiconductors with different energy band gaps [19].

Nowadays the best quality 2DESs[2] have been obtained at the Gallium-Arsenide/ Aluminium-Gallium-Arsenide $(GaAs/Al_xGa_{1-x}As)$ interface. The interface between these two semiconductor crystals can be grown with mono-atomic-layer precision using molecular beam epitaxy (MBE) machines [20, 21]. This is because the two semiconductors crystals have almost the same crystal structure leading to a nearly stress-free interface. Upon doping the

[2]For the purposes of this work, a measure of the 2DES's quality is its mobility. The higher the mobility, the better the 2DES's quality.

AlGaAs material with donor impurities (in this case, silicon Si donors) placed at a distance away from the interface, electrons are introduced into the system [22]. Since the AlGaAs has a larger band gap than GaAs, electrons residing in the n-doped region of the AlGaAs find it energetically favorable to transfer to the lower energy conduction band of GaAs. This causes an accumulation of charge on the GaAs side of the interface. The charge imbalance generates an electric field normal to the interface, which bends the bands and a quasi-triangular confinement potential develops for the conduction electrons on the GaAs side, as shown in Fig. 2.1a. This potential causes a quantization of the electron energy, and leads to so-called electric subbands E_i (i is the subband index). Since the energy difference between these electric subbands is on the order of 10 meV (100 K), at low temperatures and for densities below 5-6$\times 10^{11}$ cm^{-2} all electrons reside in the lowest subband of the quasi-triangular potential well. An alternative way to form a 2DES is to confine the electrons in a GaAs quantum well which is flanked on either side by an AlGaAs barriers. This case is depicted in Fig. 2.1b.

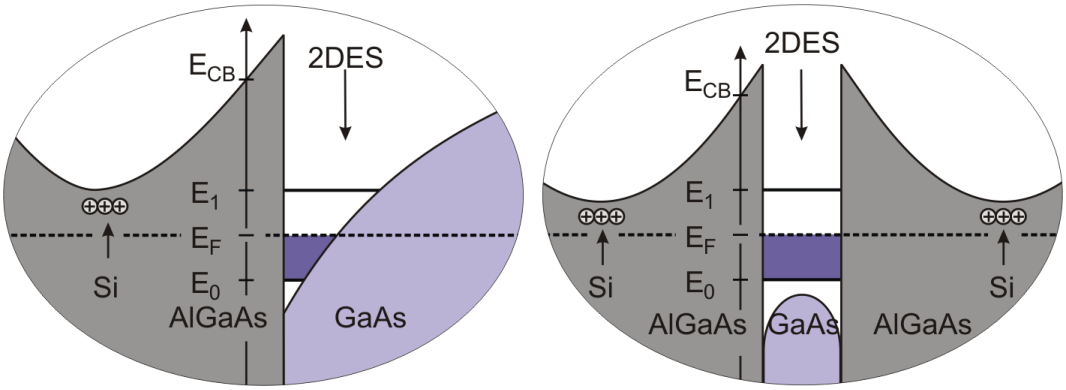

Figure 2.1: Schematic representation of the conduction bands in modulation-doped AlGaAs/GaAs samples. Since the conduction band edge of GaAs lies lower in energy than AlGaAs, electrons transfer from the doped AlGaAs region to the undoped GaAs to form a 2DES at the interface between GaAs and AlGaAs (a), or in the GaAs quantum well (b). The lowest two electric subbands E_0 and E_1 as well as the Fermi energy E_F are shown.

In both structures described above the 2DES is spatially separated from the ionized dopants. As a result, the scattering of electrons by the ionized impurity potential is significantly reduced, meaning that the electrons in the 2DES are essentially free to move in the plane. It turns out this is crucial for many of the phenomena observed in these systems: by reducing

the electron-impurity interaction and the disorder, the interaction among the electrons gives rise to a variety of collective phenomena that are not destroyed by the weak disorder.

2.1.2 Landau Quantization

Now we consider the effect of a strong magnetic field perpendicular to a noninteracting 2DES. Under this condition, the Lorentz force causes the electrons to move onto circular orbits. Quantum mechanics dictates that an electron orbit can only enclose a flux equal to an integer multiple of the elementary flux quanta $\Phi_0 = h/e$. Hence, the orbital motion becomes quantized. The quantum description of the system can be obtained by solving the Schrödinger equation using the Hamiltonian in 2.1 (ignoring interaction and the Zeeman term). In the Landau gauge $\vec{A} = (0, Bx, 0)$, where $\vec{B} = B\hat{z}$ is the magnetic field pointing in the z-direction, the problem is reduced to a shifted harmonic oscillator equation [23] ignoring the interaction term. Thus, one can solve for the eigenfunctions Ψ_{nk} whose eigenenergies E_{nk} are given by

$$E_{nk} = E_n = (n + \frac{1}{2})\hbar\omega_c \tag{2.6}$$

where n is an non-negative integer, and $\hbar\omega_c$ is the cyclotron energy (see Eq. 2.2). Note that the magnetic field has induced a condensation of the continuous energy spectrum of the noninteracting 2DES into a discrete set of highly degenerate levels. These levels are known as Landau levels, and are equally spaced by the cyclotron energy gaps. In the disorder-free case, these gaps between the levels are void of electronic states.

However, the Eq. 2.6 only describes that part of the electron energy associated with its orbital motion. To this we must add the spin contribution. The Zeeman effect splits each Landau level (LL) into two levels separated by the Zeeman energy E_Z (see Eq. 2.4).

The degeneracy of Landau states mentioned above corresponds to the fact that the eigenenergies are function of a single quantum number n, however 2D electrons have two degrees of freedom so there is a missing quantum number k which is responsible for a large degeneracy of each LL. This degeneracy may be regarded as follows: Many electronic orbits of equal size can be placed in different positions along the plane of a given 2DES. The number of states available in each spin-split LL is $n_L = eB/h$. Since this quantity increases with B, to keep the total electron density of the system constant, the Fermi energy E_F has to move so that fewer and fewer LLs are occupied with increasing B. The number of spin-split LLs occupied at a given B is defined as *the filling factor*. The filling factor can be calculated as

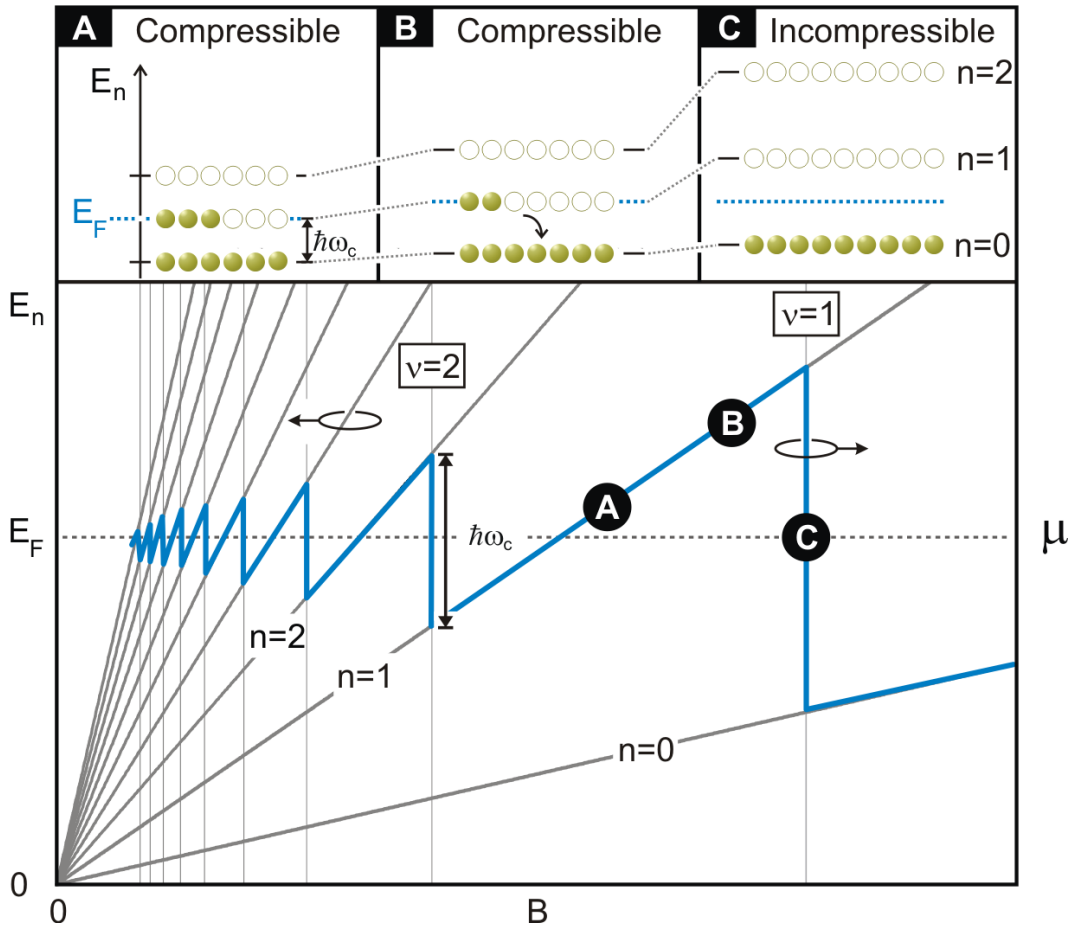

Figure 2.2: Upper panels: Schematic representation of three Landau levels, $n = 0, 1, 2$, in a nine-electron system for three different values of the magnetic field. Here the splitting due to spin degeneracy is neglected for simplicity. In the panel-A, the magnetic field is such that some electrons reside in the $n = 0$ as well as in the $n = 1$ Landau level. When the strength of the magnetic field is increased, the degeneracy of states in each Landau level increases, and electrons in the $n = 1$ LL drop into empty states with lower energy of the $n = 0$ LL (panel-B). When the magnetic field is high enough, the upper LL will be entirely emptied and all electrons reside in the lowest level, panel-C. Lower figure: Fan of Landau energies E_n for $n = 0, 1..., 9$ and the variation of the chemical potential μ at $T = 0$ with magnetic field B.

the ratio between the number of electrons per unit area n_e and the number of states per unit area available in each spin-split LL n_L

$$\nu = \frac{n_e}{n_L} = \frac{n_e h}{eB}. \tag{2.7}$$

Associated with the magnetic field are the flux quanta. Thus, the filling factor can be rephrased in terms of elementary magnetic flux quanta Φ_0 as the ratio of the number of electrons to the number of elementary flux quanta threading the sample: $\nu = n_e\Phi_0/B$, where $\Phi_0 = h/e$. Whenever the electron density n_e is an integral multiple of the density of states per LL n_L, i.e., when ν takes an integer value, there will be a jump of the chemical potential. In this case the system is said to be *incompressible* (panel C in Fig. 2.2) in the sense that removal of a single flux quanta by lowering the field, or adding a single electron into the system, requires to overcome the energy gap between the LLs. As ν deviates from the integer value, i.e., when the LL is only partially full, the chemical potential will vary continuously as the density is changed because in this situation the LL can accommodate an extra charge with a small energy cost. In this case, the system is *compressible* (Fig. 2.2 panels A and B). Hence, the compressibility of a system provides a tool to understand the type of ground state formed in an electronic system [24]. For instance a 2DES with fixed carrier density, tuning the strength of a perpendicular magnetic field, the chemical potential shows sharp sawtooth-like oscillations indicating that the ground state changes from insulating (incompressible) to metallic (compressible) as is schematically depicted in the Fig. 2.2. Here, the sharp drops are at integer filling factors where there is a gap in energy between two adjacent LLs. As explained in the next section, the presence of these gaps combined with the existence of localized states, induced by disorder, leads to an effect in the transport properties called the quantum Hall effect.

2.2 Quantum Hall Effects

The quantum Hall effect (QHE) appears when electrons confined to two dimensions are subjected to a strong perpendicular magnetic field. This phenomenon is a quantum-mechanical version of the classical Hall effect discovered by Edwin Hall in 1879. In the classical Hall effect, a current I is imposed through the sample and a magnetic field B is applied perpendicular to it. A voltage drop V_L develops along the direction of the current flow. The ratio of

V_L to I is just the ordinary resistance of the material or longitudinal resistance $R_L = V_L/I$. Simultaneously, a second voltage V_H develops within the specimen perpendicular to the current path. Due to the Lorentz force, the moving charges are deflected towards the side of the sample and give rise to charge accumulation on one boundary of the sample and charge depletion at the other. This, in turn, produces the Hall voltage V_H perpendicular to both the current direction and the magnetic field. The charge accumulation continues until equilibrium is reached; this happen when the electrostatic force resulting from the charge separation cancels the magnetic force. Considering this steady state, a classical calculation would give that the Hall resistance $R_H = V_H/I$ rises linearly with the magnetic field while the longitudinal resistance R_L remains essentially constant at small magnetic field. If n_e is the carrier concentration of the material, the classical Hall resistance is expressed as:

$$R_H = B/en_e. \tag{2.8}$$

While this expression for the Hall resistance discovered by Edwin Hall was expected to remain valid in high magnetic fields and at low temperatures, Klaus von Klitzing in 1980 discovered that when the electrons are confined to two dimensions the situation is dramatically different [25]. For this discovery von Klitzing was awarded the 1985 Nobel Prize in Physics.

Fig. 2.3 depicts the outcome of one of our transport measurements performed on a very clean sample. Here, the Hall resistance R_H (upper curve) and the longitudinal resistance R_L (lower curve) are shown as a function of magnetic field B at a temperature less than 20 mK. Basically, there are two main differences between the classical Hall effect and the quantum Hall effect, which can be noticed phenomenologically from these data. One can observe that the Hall resistance instead of rising linearly with magnetic field, shows plateaux around specific field values, contrasting with the result expected from Eq. 2.8. Second, associated with each of these plateaux is a drop to zero in the longitudinal resistance R_L of the same magnetic field range, indicating that there is no dissipation. But, the most remarkable aspect is that on the plateau regions the Hall resistance R_H is quantized in units of h/e^2 in the following way:

$$R_H = (h/e^2)(1/\nu) \tag{2.9}$$

where ν are the filling factors for incompressible states. These plateaux in R_H and their accompanying vanishing of R_L are the hallmarks of the so-called quantum Hall effects. From

the Fig. 2.3 two subset of filling factors can be observed. Integer values of ν correspond to the integer quantum Hall effect (IQHE), while the fractional fillings correspond to the fractional quantum Hall effect (FQHE). Although these two effects look qualitatively similar in experiment, they are the result of quite different physics.

2.2.1 Integer Quantum Hall Effect

The IQHE and the FQHE arise whenever the 2DES becomes incompressible. The origin of the IQHE lies on the fact that the ground state at integer filling factor, $\nu = i$, consists of i Landau levels fully occupied, with a gap to excitations. Under these conditions, the filling factor ν is an integer i and the number of electrons per unit area is $n_e = in_L$. Using this relation in the expression for the classical Hall resistance (Eq. 2.8) gives exactly the values of the integer quantum Hall plateaux.

$$R_H = (h/e^2)(1/i), i = 1, 2, 3 \cdots \tag{2.10}$$

However, the gap in the energy spectrum is not the only important ingredient to explain the IQHE, because it is unable to account for the presence of plateaux in R_H and the persistence of the vanishing of R_L over extended regions of the applied magnetic field. The second crucial ingredient is the disorder in the system [26, 27]. Disorder in high-quality heterostructures is mostly due to the ionized donors placed randomly a distance away (referred to as the spacer) from the 2DES. This spatial displacement reduces the amplitude of the random potential experienced by the 2D electrons. This disorder potential varies on a length scale comparable to the spacer thickness (see Fig. 2.4a). If this length scale is large compared to the magnetic length, then the LLs simply follow the topography of the potential as shown in Fig. 2.4b.

In a magnetic field electrons move along contours of constant potential. In the schematic illustration of the disorder potential landscape shown in Fig. 2.4a, one can distinguish two different types of states. Equipotential lines encircling a potential hill or trapped in a valley correspond to localized states. Electrons occupying such localized states cannot contribute to current flow through the sample. A second type of states are the so-called extended states, which are associated with equipotential trajectories that extent throughout the system and can carry electrical current from the source to the drain [28]. Consequently, the sharply defined Landau levels broaden into bands composed of localized states in the tails of the broadened level and extended states at the center (see Fig. 2.4c). The energy ranges where

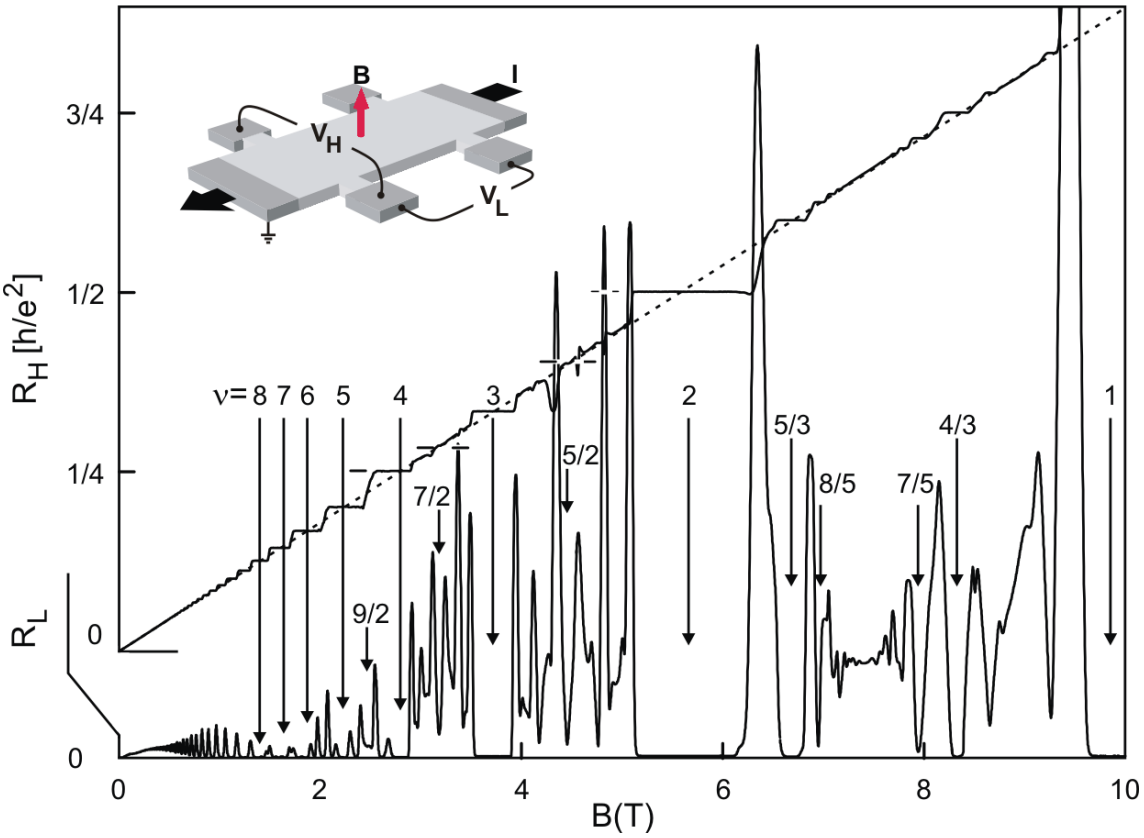

Figure 2.3: The integer quantum Hall effect is characterized by well-developed plateaux at quantized values of the Hall resistance R_H, and vanishing values of the longitudinal resistance R_L at integer values of the filling factor ν. Here the dashed diagonal line represents the classical Hall resistance, and the solid line the experimental result. Inset: standard Hall bar device for the measurement of the Hall effect. A current I is made to flow from one end of the sample to the other and a magnetic field B is applied perpendicular to the sample. Two voltages are measured: the Hall voltage V_H is measured as the potential difference between two contacts on opposite sides of the current path, while the longitudinal voltage V_L is measured as the potential difference between two contacts on the same side of the current path. The longitudinal resistance R_L and the Hall resistance R_H are defined as the ratios V_L/I and V_H/I respectively. The additional plateaux and their corresponding small vanishing values of the resistance at fractional filling factors ν correspond to the fractional quantum Hall effect. Both quantum Hall effects are discussed in the text.

only localized states are available represent a mobility gap. The existence of these localized states allows us to understand the plateaux in R_H and the vanishing of R_L over a range of magnetic fields. Because, as long as a variation in the magnetic field causes the addition or removal of electrons from the localized states, the Fermi level remains within the mobility gap and the number of occupied extended states unaltered. Bearing in mind that only the extended states contribute to the electrical transport, then the transport properties of the system remain constant. This leads to plateaux in R_H and vanishing resistance in R_L over extended regions of magnetic field.

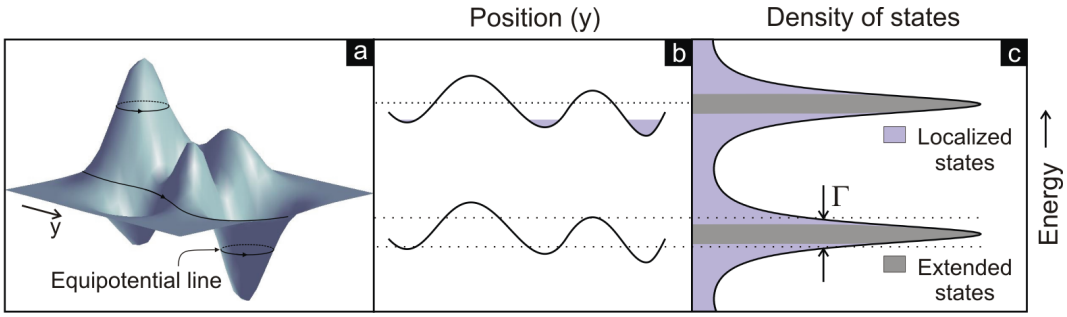

Figure 2.4: (a) Schematic illustration of a disorder potential showing closed equipotential curves encircling low or high potential regions, and an open contour connecting two opposite sides of the system. The closed contours represent localized electronic states while the open contours correspond to extended state. (b) Schematic representation of the energy fluctuations of the Landau levels as a consequence of disorder. The average magnitude of the fluctuations is equal to the broadening Γ of the Landau levels. (c) Density of states diagram for two Landau levels in a system with disorder, the bands of extended and localized states are depicted. The extended states are located at the center of each impurity-broadened Landau level while the localized states are found in the tails of the Landau levels.

Although the previous explanation provides insights into the physics of the IQHE, it does not explain the exact quantization of R_H. That can be understood by considering edge states (see Fig. 2.5a). At the boundaries of a real sample the depletion produces an upward bending of the LLs [3], as shown in Fig. 2.5b. For each LL lying below the Fermi energy E_F in the bulk, there will be an intersection with E_F in the vicinity of the sample boundaries. At the intersection an one-dimensional edge channel forms, which runs along the sample boundary. For N filled LLs, one gets N chiral edge channels along either side of the sample. Charge propagation only proceeds in one direction and backscattering is not possible. Hence, edge current transport will be dissipationless. Moreover, since the charge velocity is proportional to the slope of the LL, edge channels on opposite sides of the sample carry current in opposite directions. Classically, these edge states can be thought of as skipping orbits, which result from the reflection of electrons moving along its cyclotron orbit at the boundary of the sample (see Fig. 2.5c). The importance of these edge channels for the transport properties in the quantum Hall regime has been emphasized by a model proposed by Büttiker [29] which is based on ideas by Landauer [30] of relating two-terminal conductances to transmission probabilities by attaching different electrochemical potentials and currents to each contact. In this formalism a current flowing along a single edge channel located between two contacts at different electrochemical potential μ_1 and μ_2 is [31]

$$I = e\upsilon D(E)(\mu_1 - \mu_2) = \frac{e}{h}\Delta\mu, \tag{2.11}$$

where υ is the velocity of the electron in the channel and $D(E) = 1/2\pi\hbar\upsilon$ the density of states. Since the voltage drop between the contacts is $eV = \Delta\mu$, the two-terminal resistance of an edge state is equal to $R = h/e^2$. For N channels $R = h/Ne^2$. Now, the suppression of backscattering due to the chirality of the edge channels, implies that they form equipotential lines. Thus, the voltage drop measured by using two contacts placed along the boundary of the sample will be zero, whereas the Hall resistance measured between opposite sides of the sample will be quantized. Finally, this leads to $R_L = 0$ and $R_H = h/Ne^2$, as expected under quantum Hall conditions. This approach to the QHE is known as the edge channel model.

[3] The boundaries of the sample can be defined electrostatically, e.g. by patterned gates on the sample surface which deplete the 2DES underneath, or by etching a mesa and removing the 2DES or at least the doped layer.

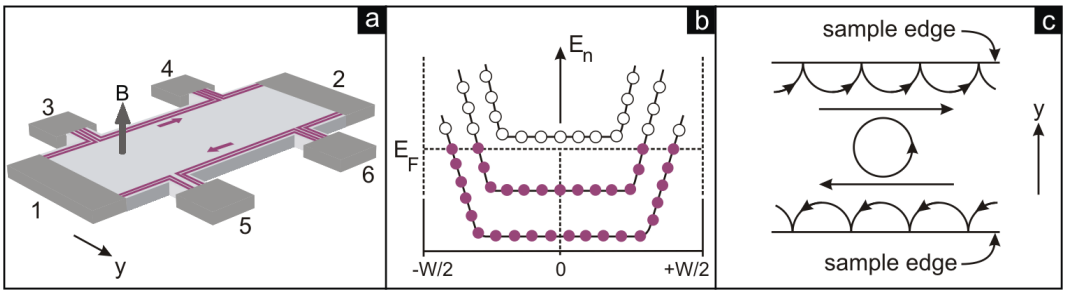

Figure 2.5: The edge-state picture of the quantum Hall effect. (a) Illustration of a Hall bar at filling factor $\nu = 2$ (spin is not included) showing two edges states (purple lines) in the vicinity of the lateral boundaries. Arrows indicate the direction of electron flow on opposite sides of the sample. The width of the Hall bar is denoted as W. (b) Energy states in the first three Landau levels in the presence of a lateral confinement potential. States below the Fermi energy (E_F) are occupied (filled circles) while states above E_F are empty (blank circles). The edge channels are located at the intersection of the Landau levels with E_F. Here, the disorder-free case is considered for simplicity. (c) In the bulk of the sample, electrons follow closed cyclotron orbits, while near the edge, the electron hits the boundary and is reflected. This results in a skipping motion along the boundary of the sample in opposite directions at the top and bottom boundary.

2.2.2 Fractional Quantum Hall Effect

Unlike the IQHE, whose origin is linked to the energy gaps in the single-particle energy spectrum, the FQHE discovered by Daniel Tsui and Horst Störmer in 1982 [1] cannot be explained within a single-particle framework. In the fractional effect R_H is quantized at $h/e^2\nu$ with ν rational fractions with odd denominators and it is accompanied by a vanishing of R_L. However, like the integer effect, the fractional effect is also the result of a gap in the excitation spectrum. This gap results from a collective state where all the electrons in the system participate in a highly correlated manner [32,5]. The essence of this highly correlated state is captured by the wave function proposed by Laughlin [2]. It describes an incompressible and homogeneous quantum liquid, whose electron distribution is such that the repulsive Coulomb interaction is minimized. According to Laughlin, when a 2DES is threaded by m elementary flux quanta per electron, i.e., at fractional filling factor $\nu = 1/m$, the electron system condenses into a highly correlated quantum liquid, which can be mathematically represented by

the following wave function [2]

$$\Psi_{1/m}(z_1, \ldots, z_{N_e}) = \prod_{j<k}(z_j - z_k)^m \exp\left[-\frac{1}{4\ell_B^2}\sum_j |z_j|^2\right], \tag{2.12}$$

for a number N_e of electrons. Here $z_j = x_j + iy_j$ is the complex notation for the location of the j^{th} electron in the 2D plane with coordinates (x_j, y_j), and m is a positive odd integer. This wave function is anti-symmetric under exchange of any two electrons, as required for fermions [33]. The electron correlation is contained in the polynomial term (or Jastrow-type term) [34], whereas the Gaussian term stems from the non-interacting case.

For $m = 3$, Eq. 2.12 describes the state at $\nu = 1/3$. The term $z_j - z_k$ represents the interaction of the j^{th} electron with all other electrons. At $\nu = 1/3$ there are three elementary flux quanta per electron, therefore the wave function of j^{th} electron will have three zeros for every other electron k it interacts with. One zero, or flux quanta, is located at the position of the j^{th} electron due to the Pauli's exclusion principle. The remaining two zeros are also placed at the position of the electron j in order to minimize the inter-particle Coulomb repulsion energy. In this way, an electron will see a three-fold zero at the positions of the other electrons and they are rearranged in such a manner as to be the furthest away from each other as possible.

As prelude to one of the main topic in this thesis, we would stress that the internal orders of FQH liquids are very different from the internal orders in other correlated systems such as crystals, superfluids, etc. The order in the latter systems can be described by order parameters associated with broken symmetries [34], whereas the order in FQH liquids is a kind of ordering that cannot be described with broken symmetries [35, 36].

Using exact diagonalization studies, Laughlin showed that the above wave function is a good description of the ground state at filling $\nu = 1/m$. He also showed that the excitations supported by this liquid correspond to fractionally charged quasi-particles. The creation of one such quasi-particle costs a finite energy. One can elucidate this process by shifting the filling factor away from $\nu = 1/m$, by either adding or removing a flux quanta. Bearing in mind that the state at $\nu = 1/m$ corresponds to having m flux quanta per electron of charge e, then the introduction or removal of a flux quanta is equivalent to add either a quasi-hole or a quasi-electron of charge $e^* = e/m$. This non-zero energy required to create such quasi-particle represents the gap in the many-body excitation spectrum, which leads to a plateau in R_H and a minimum in R_L in the FQHE.

Laughlin's wave function can also account for the states at $\nu = 1 - (1/m)$ by using particle-hole symmetry [37]. The remaining odd-denominator states, also referred to as higher-order FQH states, can be understood in either one of two schemes. One is the hierarchical model, proposed independently by Haldane [38], Halperin [39], and Laughlin [40], in which higher-order FQH states are constructed as a successive condensation of quasi-particles of the Laughlin states. When ν deviates sufficiently from exact $1/m$, the ensuing density of quasi-particles can be high enough to overcome localization. These quasi-particles can interact via their Coulomb repulsion and, at a critical density, condense themselves to form new FQH states. In turn, the quasi-particles of these new ground states will form new FHQ states. In this way, the quasi-particles of each new ground state give rise to a new fractional quantum Hall state, so that eventually all the higher-order FQHE states are covered. In summary, one can say that hierarchical FQH states are similar to Laughlin states for quasi-particles. The second scheme is based on the introduction of compound particles referred to as composite fermions [17]. These particles can be thought of as assembled from an electron and an even number of magnetic flux quanta (more precisely vortices). Electrons capture vortices to turn into composite fermions in order to minimize their interaction energy. As composite fermions move about, the vortices bound to them produce Berry phases [41], which cancel part of the Aharonov-Bohm phases originating from the applied magnetic field. Composite fermions sense an effective magnetic field that is much smaller than the applied magnetic field B. The effective magnetic field B^* is given by

$$B^* = B - 2n_e\Phi_0 \tag{2.13}$$

Similar to ordinary electrons, the composite fermions execute circular orbits in the presence of an non-zero B^*. This gives rise to the formation of their own Landau levels (CF-LL), and each time an integral number of them is completely filled, the system will exhibit an integer quantum Hall effect. The corresponding integer composite fermion filling factor, ν^*, can be related to the electron filling factor, ν, by inserting B^* in Eq. 2.7

$$\nu = \frac{\nu^*}{2\nu^* \pm 1} \tag{2.14}$$

Hence, the IQHE of composite fermions corresponds to the FQHE of electrons. For example in the composite Fermion picture $\nu = 2/3$ and $\nu = 2/5$ corresponds to having two filled Landau levels of composite fermions ($\nu^* = 2$) for negative and positive B^*.

2.3 Localization in the Quantum Hall Regime

Localization is an essential ingredient to understand the quantum Hall effect. Localized states explain the presence of plateaux in R_H and the persistence of zero R_L over a finite magnetic field range. In section 2.2.1, these localized states were associated with the single-particle drift of electrons along contours of the disorder landscape. It turns out that this single-particle picture fails to account for the microscopic manifestation of localization. Recent experiments carried out by Ilani $et\ al.$ [42] showed that the observed localized states are utterly different from those predicted by single-particle theory. These studies confirmed that the disorder potential remains essential to the observation of localized states, but in addition Coulomb interaction plays an important role, i.e., screening of the disorder potential cannot be ignored. The localized states appear only when the screening ability of the electrons is hampered because empty states are locally no longer available to rearrange and compensate the disorder potential.

2.3.1 Basic Phenomenology of Localization

The above-mentioned experiments involve local measurements of the electronic compressibility κ. This thermodynamic quantity is inversely proportional to the derivative of the chemical potential μ with respect to the electron density n, i.e., $\kappa \propto (\delta\mu/\delta n)^{-1}$. Such experiments were performed using a single-electron transistor as a local detector of the electrostatic potential (see section 3.3). A typical outcome of these experiments is depicted in Fig. 2.6a. The plot shows a color map of the inverse compressibility, $\delta\mu/\delta n$, as a function of magnetic field (B) and density (n), which is tuned by using a back gate. In this color map, incompressible and compressible behavior correspond to bright and dark regions respectively. The slope of each incompressible region in the (B, n)-plane is given by $dn/dB = e\nu/h$, where ν is integer or fractional. Hence, each incompressible region is associated with an integer or fractional quantum Hall (QH) state in the (B, n)-plane. Integer QH phases at $\nu = 1, 2, 3$ and 4, as well as the fractional QH phase at $\nu = 1/3$ are visible in this compressibility measurement. The band of horizontal lines is associated with the insulating phase at very low densities.

Figure 2.6b shows a very fine measurement of the $\nu = 1$ and $\nu = 2$ incompressible regions, which reveal that within each incompressible region there is a group of many parallel (dark) lines. In order to understand the meaning of these lines, one has to recall that the

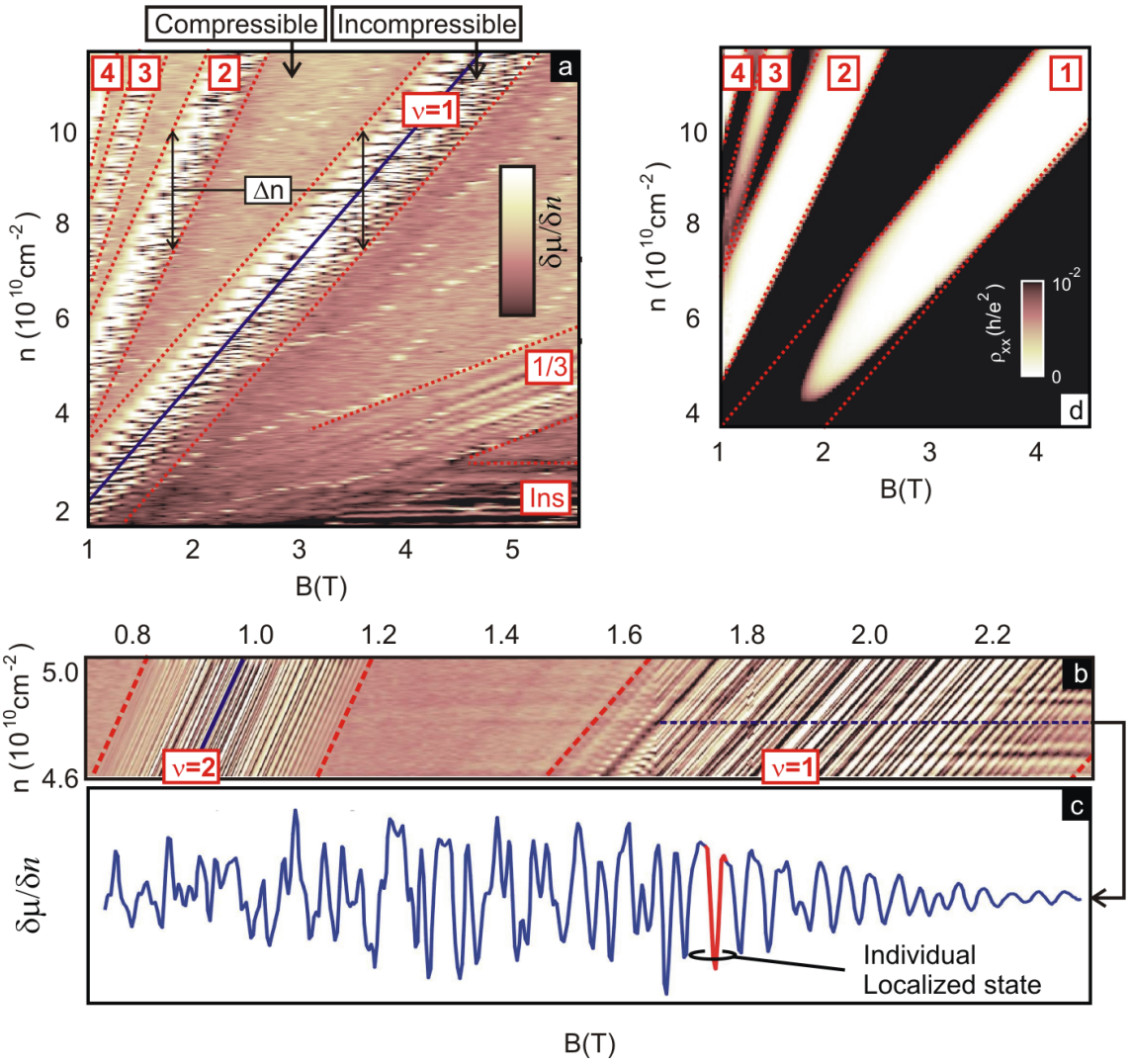

Figure 2.6: a) Color map showing a measurement of the inverse of the compressibility $d\mu/dn$ as a function of magnetic field, B, and density, n. This measurement over a large range of B and n was taken using a stationary single-electron transistor placed on the surface of a heterostructure that has a 2DES buried below the surface. Incompressible (bright) regions correspond to the quantum Hall (QH) phases of the system, whereas dark regions are associated with compressible regions. (b) This panel shows a detailed measurement of the $\nu = 1$ and $\nu = 2$ incompressible regions, many parallel (dark) lines are observable. Each line represents the evolution of the charging of an individual localized state in the density field-plane. (c) Cross section along the dotted line through a group of lines corresponding to the QH phase at $\nu = 1$. Each spike corresponds to the filling of an individual localized state. (d) Longitudinal resistance, ρ_{xx}, measured as a function of B and n. The bar in the bottom right corner gives the color scale.

QHE arises from the interplay between localized and extended states (see section 2.1.2). While extended electrons spread their charge over the entire volume of the system, a localized electron is confined to a small region in space. Therefore, as opposed to an extended state[4], whenever a single electronic charge enters a confined region, it results in a discrete jump of the local chemical potential and therefore a spike in its derivative with respect to the density $\delta\mu/\delta n$, or in the local compressibility. The meaning of each line becomes apparent taking a profile at fixed density through a group of lines (Fig. 2.6c). Based on what was discussed previously, each spike in $\delta\mu/\delta n$ represents the filling of an individual localized state, and therefore each line describes the evolution of a localized state in the (B, n)-plane.

A careful examination of the bands of localized states reveals three properties common to all bands. Firstly, the evolution of localized states within each band follows the same slope as the envelope. Secondly, the number of these state in each group remains fixed as the system evolves in the (B, n)-plane, i.e., no new states are added when the magnetic field is increased. These two observations can not be reconciled with the single-particle picture. In the single-particle picture the number of localized states would increase as the magnetic field increases due to the LL degeneracy and these states would follow arbitrary trajectories when plotting their occupation in the (B, n)-plane. Thirdly, each group of lines cover a region that has a constant width, Δn, in the (B, n)-plane. This Δn is the same for different QH phases. This observation is consistent with transport experiments carried out on the same sample as function of B and n. Fig. 2.6d shows the measured longitudinal resistivity, ρ_{xx}, where one can observe a clear correspondence between the incompressible regions where ρ_{xx} (white regions) drops to zero and the regions where localized states appear in Fig. 2.6a.

In order to accommodate these experimental manifestations of localization, a simple model that consider the interactions between the electrons and hence screening was formulated in Ref. [42]. This model will be reviewed in the next section.

2.3.2 The Dot Model

To simplify the introduction of localization driven by Coulomb interaction, let us first consider a 2DES in the vicinity of filling factor one ($\nu = 1$). At high magnetic field, far from the integer filling, the large compressibility within the LL provides nearly perfect screening of

[4]Since charge is spread over the entire system, the chemical potential will gradually change and therefore the inverse compressibility will be smooth.

the disorder potential. This is due to the fact that the density of states within the LL is large enough, so that electrons can rearrange and create a nonuniform electron density distribution, denoted as $n(\vec{r})$. The corresponding potential distribution in the plane of the 2DES is identical but opposite in sign to the bare disorder potential (see Fig. 2.7a). As explained in section 2.1.2, for a given B the local electron density in a LL, n_{LL}, cannot exceed $n_{max} = B/\Phi_0$, i.e., n_{LL} fulfills the constraints $0 \leq n_{LL} \leq n_{max}$. At the center of the LL, these constraints are irrelevant because the density fluctuations required for achieving perfect screening are smaller than n_{max}. Each electron added to the system experiences a flat screened potential and ends up being delocalized. However, as the filling factor increases towards $\nu = 1$, the required density for perfect screening in certain regions of the sample exceeds n_{max}. The system locally fails to screen the bare disorder potential (see Fig. 2.7b). These regions coexist with small compressible regions where the LL is not yet filled, i.e., regions where the density $n(\vec{r}) < n_{max}$ and screening is still active. Once a compressible region becomes surrounded by incompressible regions, it behaves as a quantum dot. Strictly speaking, since the compressible regions have a lower density inside them compared to their surroundings they are anti-dots. As the density increases further, regions corresponding to the peaks in the screening density profile start to occupy the next LL and dots form (see Fig. 2.7c). The addition and removal of charge into a dot or anti-dot is governed by Coulomb blockade physics, i.e., it occurs discretely one particle at a time. This charging produces spikes in $\delta\mu/\delta n$. Each spike corresponds to filling one localized state within a dot or anti-dot.

Let us now consider why the spectrum of localized states exhibits a constant number of lines running parallel to the line of integer filling in the (B, n)-plane. This behavior can be attributed to the fact that the disorder potential remains invariant as the magnetic field is tuned. Identical configurations of dots or anti-dots recur irrespective of the magnetic field strength. The only effect of increasing the magnetic field is to raise n_{max} and hence the value of the average density where the same dot and anti-dots reappear. Therefore, despite the increase of n_{max} with the magnetic field, the number of localized states remains constant. At different filling the same number of localized states appear, except that now the lines run parallel to the underlying filling factor in the (B, n)-plane.

The localized states appear only in regions with a width of Δn. This fact is associated with the amplitude of the bare disorder potential. Each edge of an incompressible band represents the termination of the localized states. This occurs when compressible pockets (dots

or anti-dots) form a connected network. Here the compressible pockets lose their quantum confinement and therefore lose their discrete charging spectra. This is a percolation transition from a compressible medium into an incompressible background. Within each LL exists two such percolation transitions. The first occurs when the density is $n = \Delta n_{disorder}/2$. The second transition takes place when the density is $n = n_{max} - \Delta n_{disorder}/2$. This explains why each bunch of localized states has a width of $\Delta n_{disorder}$, which is the same for different QH phases. For each energy gap in the energy spectrum no matter its origin, the screening ability of the system will be limited. Identical dots (or anti dots) will form and local charging spectra within the same band of density Δn appear.

In conclusion, this model states that the spectra of localized states are defined only by the bare disorder potential and the presence of an energy gap.

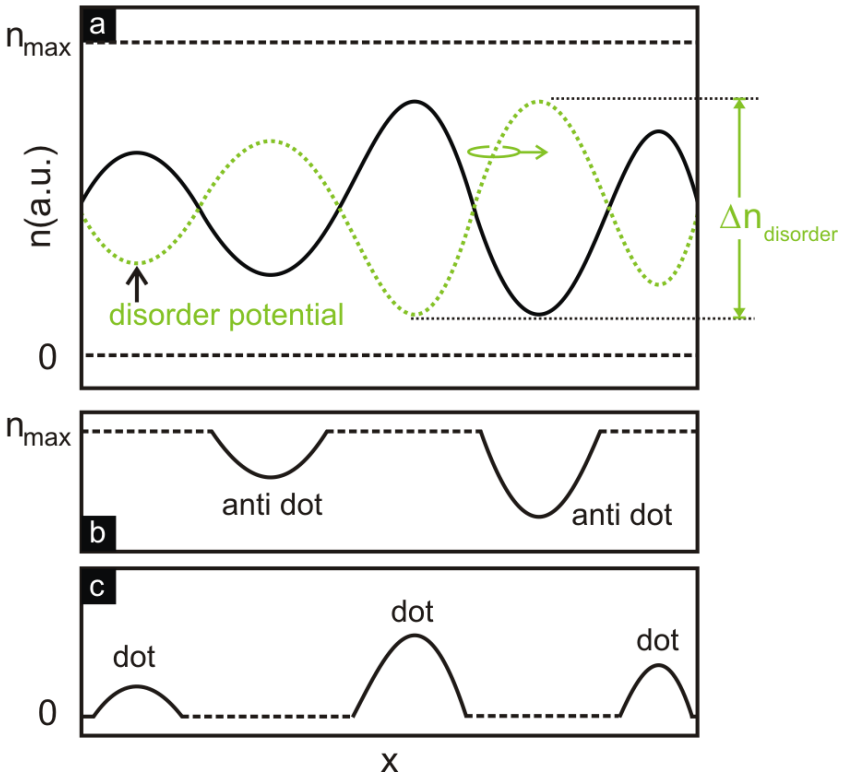

Figure 2.7: Schematic diagram illustrating the formation of dots and anti dots. (a) When a LL is partially filled, the bare disorder potential (green curve) is entirely screened by the electrons. To do so, the electrons form an inhomogeneous density profile (black curve). (b) Close to complete filling, when the allowed density n_{max} is reached the system locally turns incompressible and only certain areas (where the density is lower than n_{max}) remain compressible. These compressible regions form anti dots. (c) When the density is slightly higher than n_{max}, i.e., when the next LL starts to be filled (n_{min} indicates the allowed minimal density of the next LL), compressible areas, which form dots, emerge.

Chapter 3

Local Probe and Transport Techniques

Having presented part of the theoretical background, we now proceed to describe the samples as well as the details of the measurement techniques involved in these studies. We first review the transport measurement technique and then the local probe technique. The latter measures the local electronic compressibility using a single electron transistor.

3.1 Sample Structures and Devices

Our experiments were carried out on structures made from alternating layers of GaAs/AlGaAs. These are grown on GaAs substrates using molecular beam epitaxy by our collaborators. In this work, we have used two different wafers. The experiments described in chapter 4 were all performed on specimens cleaved from the LP8-9-01.2 wafer, a modulation-doped 30 nm wide $GaAs/Al_{0.24}Ga_{0.76}As$ quantum well, with silicon δ-doped layers placed symmetrically on either side of the well. The electron mobility is $18 \times 10^6 cm^2/Vs$ and a carrier density of $2.5 \times 10^{11} cm^{-2}$ is measured in the dark, i.e., in the absence of additional light-induced carriers. The data shown in Fig. 2.3 were taken on this wafer. A schematic drawing of the layer sequence is shown in Fig. 3.1a. The W11-27-01.1 wafer has served to carry out the experiments reported in chapter 5. This wafer consists of a $GaAs/Al_{0.32}Ga_{0.68}As$ quantum well with a width of 22 nm. The silicon δ-doping was placed 90 nm above the quantum well and provided an electron density of $0.8 \times 10^{11} cm^{-2}$. A backgate, consisting of 200 nm of heavily doped n^+-GaAs, was grown in-situ at a distance of $1.8 \mu m$ underneath the quantum well. Biasing the backgate allowed a continuous tuning of the density from 0.42 to $1.18 \times 10^{11} cm^{-2}$. The layer sequence of this wafer is depicted in Fig. 3.1b.

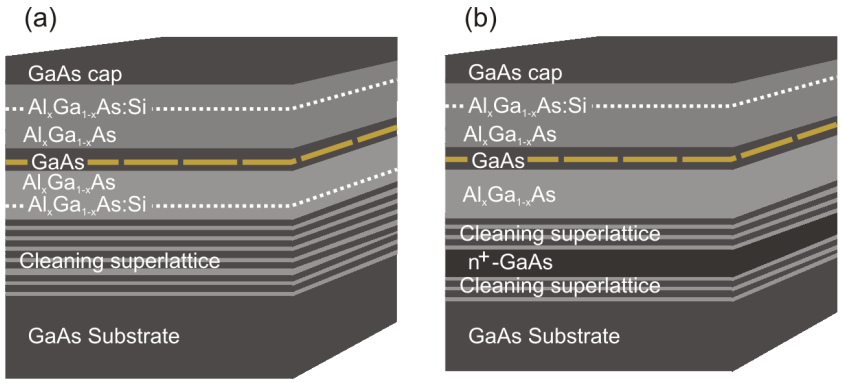

Figure 3.1: Two sketches showing the different layer sequences of the wafers utilized in this thesis. (a) Structure of the LP8-9-01.2 wafer grown by Loren Pfeiffer and Kenneth West from Bell Laboratories. (b) W11-27-01.1 wafer grown by Dieter Schuh and Gerhard Abstreiter at the Walter-Schottky Institut.

All the measurements in this thesis were performed on devices in the van der Pauw geometry. They were prepared with optical lithography. A typical arrangement of contacts used in the transport measurements of chapter 4 is depicted in Fig. 3.2. Twelve contacts were placed symmetrically around the mesa perimeter. A detailed description of the procedure for defining and contacting the devices is presented in appendix A.

The mesa definition and ohmic contacts are the only necessary processing steps in the devices used in the studies of chapter 4. However, the device used in the studies of the chapter 5 involves the fabrication of stationary single electron transistors (SETs). The devices were fabricated by Basile Verdene from the Weizmann Institute of Science in Rehovot, Israel. On the mesa, aluminum based SETs were fabricated at various locations. In Fig. 3.3a, we show a sketch of the SET on the mesa, whereas a scanning electron microscope picture of a SET is shown in Fig. 3.3b. A SET is a tunneling device whose current flow is governed by the Coulomb blockade effect [43]. The device consists of a small metallic island coupled to source and drain leads by tunnel junctions. The junctions are made from Al_2O_3, which is obtained using a controlled oxidation inside the evaporation chamber of part of the aluminum that forms either the island or the leads. As we shall explain below, with this device it is possible to measure the electronic compressibility of the 2DES.

3.2 Transport Measurement Technique

To investigate the 2DES, electrical transport is the most straightforward technique since this system can be readily contacted electrically. To resolve the small energy scales involve in the electron correlation physics described in this thesis, the sample has to be cooled down to millikelvin temperatures. We carried out the electrical measurements in a top-loading dilution refrigerator (Oxford Kelvinox TLM ^{3}He/^{4}He Dilution Refrigerator), which has a base temperature of less than 20 mK. The refrigerator acquires its cooling power from a continuous dilution of ^{3}He in ^{4}He in the mixing chamber [44]. In these experiments, once the sample is glued and wired up to a chip carrier, the chip carrier is inserted into the socket of a sample stage located in a top-loading sample holder. The sample holder, equipped with an in-situ rotating sample stage, allows to lower the sample directly into the ^{3}He/^{4}He mixture. Our dilution refrigerator is equipped with a high field superconducting magnet that can apply a magnetic field up to 15 T (Tesla).

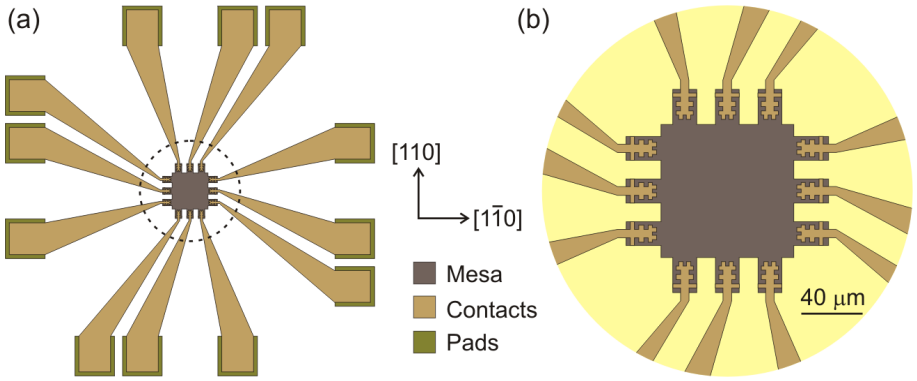

Figure 3.2: Schematic drawing of the device structure. (a) The van der Pauw geometry depicted here has twelve contacts placed along the sample perimeter. The bond pads to wire the device to the pins of a chip carrier are also shown. (b) Magnified view of the mesa to show the details of the contacts. The quality of the ohmic contacts depends on the orientation of the interface between the contacts and the 2DES with respect to the crystallographic directions. The Christmas-tree like shape used in the contacts allows to have the interface in both $[1\bar{1}0]$ and $[110]$ crystallographic directions.

A typical measurement consists of imposing an AC-current through the source and drain contact of the sample and measuring the voltage difference which appears across two po-

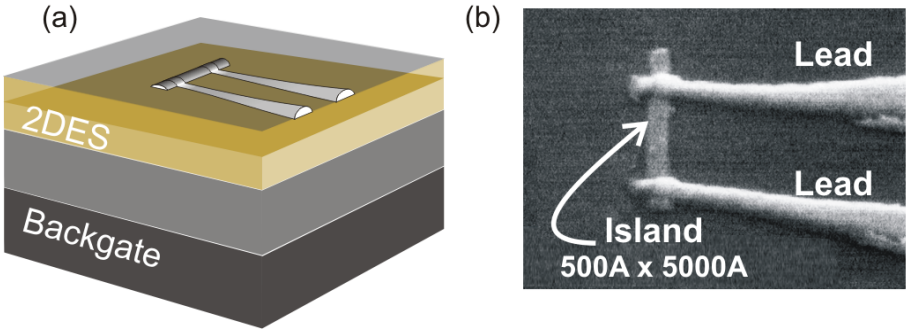

Figure 3.3: (a) Schematic drawing of the SET on the top surface of the heterostructure, which contains a 2DES and an in-situ grown backgate. (b) Scanning electron image of an aluminum based SET. The main components of the device, the source and drain leads and the small metallic island, are denoted.

tential probes. The AC-current (I_{ac}) is injected by applying an AC-voltage across a large resistor (10 MΩ) placed in series with the sample (see Fig. 3.4a.). Dividing the measured voltage by the current yields the electrical resistance, which is the key quantity we analyze in our transport measurements. These experiments were performed in a four-terminal measurement configuration. The experimental set-up is shown in Fig. 3.4a. Using a function generator (Stanford Research Systems Model DS345) a sinusoidal current with a frequency of 13 Hz and a small amplitude of 10 nA was imposed as a current excitation. The magnetic field ramp rate is also kept low in order to prevent sample heating. The voltage is detected with a lock-in amplifier (Lock-In Amplifier model SR830 DSP) with an averaging time of 1 second. Its output is finally measured with a digital multimeter (Keithley 2000) and the result is sent to the computer via a GPIB interface. The lock-in amplifiers were galvanically isolated from mains by using isolation transformers.

To investigate our sample under nonequilibrium conditions, we have performed experiments in the presence of a large DC current bias (I_{dc}). The variable I_{dc} is imposed in a floating configuration. Its direction can be chosen independently from the I_{ac} direction. When I_{ac} is parallel to I_{dc}, both excitations were applied using the same function generator (Stanford Research Systems Model DS345). However, when I_{dc} was directed perpendicular to I_{ac}, the DC bias to produce I_{dc} was generated with the help of a separate DC-voltage source (using a Yokogawa 7651 DC source) and two 50 MΩ resistors, as shown in Fig. 3.4b.

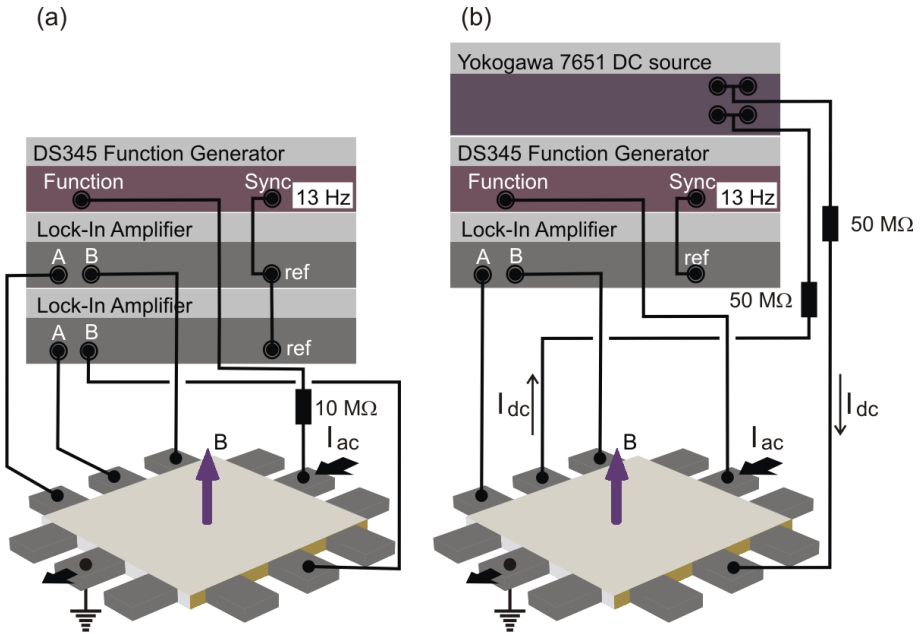

Figure 3.4: Schematic illustration of our lock-in amplifier based four-terminal technique to measure the Hall and longitudinal resistance on a square sample with twelve contacts. (a) Experimental set-up used in the measurements with only an AC-current. A function generator and a resistor of 10 MΩ is used to drive a small I_{ac} through the sample. The Hall and longitudinal voltages are measured using lock-in amplifiers. (b) Experimental set-up used in the measurements when an additional DC-current (I_{dc}) is imposed. Here the case is shown when I_{dc} is applied perpendicular to the I_{ac} direction. A DC source, together with two resistors of 50 MΩ, are used to generate the I_{dc}.

3.3 Local Probe Measurement Technique

Transport measurements allow us to probe the properties of a system from a macroscopic point of view. However, they lack the ability to disclose microscopic information about the phenomenon under study. In order to investigate the properties of a 2DES in the quantum Hall regime from a microscopic stand point, we have carried out local probe studies using a stationary single electron transistor (SET) placed on top of the sample containing the 2DES (see Section 3.1). The SET acts as an electrometer. It allows to measure the local chemical potential as well as changes in the chemical potential when the density is modulated.

3.3.1 Local Electronic Compressibility

The electronic compressibility is a thermodynamic quantity that provides information about the many-body density of states of the system [45,46,47,48]. The compressibility κ is simply related to the chemical potential μ, and density n of the system according to:

$$\kappa = \frac{1}{n^2}\left[\frac{\delta n}{\delta \mu}\right] \tag{3.1}$$

Hence, to measure compressibility locally, one has to induce a change in density and measure the corresponding change in the chemical potential. The density can be modulated by applying an oscillating bias voltage on the back gate, which couples capacitively to the 2DES. To measure the change in the chemical potential $\delta\mu$, one can use the following scheme. The electrochemical potential V of the system is defined by the sum of the chemical potential μ and the electrostatic potential ϕ, namely:

$$eV = \mu + e\phi \tag{3.2}$$

In our experiments, the 2DES is kept in equilibrium: an external voltage source fixes the electrochemical potential (see Fig.3.5). Now, suppose that the density at a certain location of the 2DES increases. As a result the local chemical potential increases. This change in the chemical potential $\delta\mu$ has to be compensated by a change in the electrostatic potential $\delta\phi$ of opposite sign, since the electrochemical potential remains fixed:

$$\delta\mu = -\delta\phi \tag{3.3}$$

Therefore, a measurement of the change in the local electrostatic potential $\delta\phi$, is sufficient to infer the change in the local chemical potential $\delta\mu$ of the system and therefore the local compressibility. The local electrostatic potential can be detected with a SET deposited on top of the sample. The 2DES then serves as the gate of the SET.

It might be worth mentioning that the chemical potential can be defined locally only when the semiclassical approximation [49, 50] is valid.

3.3.2 Using a SET as a Local Electrostatic Probe

A SET is a device whose current flow can be turned on and off by changing the voltage on a gate electrode [43, 51]. In experiments where a SET is used as a local electrostatic

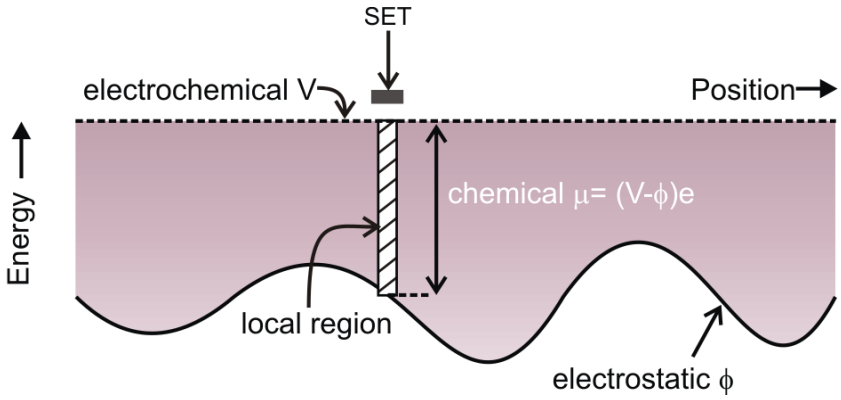

Figure 3.5: Schematic illustration of electrochemical potential V, chemical potential μ and electrostatic potential ϕ of a 2DES in electrochemical equilibrium. When the 2DES is in equilibrium, μ and $e\phi$ add up to a constant value eV. Therefore, changes in the local $e\phi$ are equal and opposite in sign to changes in μ. In the framework of the semiclassical approximation, the electrostatic potential is slowly varying within the local region limited by the shaded box. Then, the chemical potential within the local region is nearly constant or independent of position.

probe, the 2DES serves as the gate of the SET. The SET is placed on top of the surface of a heterostructure containing the 2DES, so that changes in the local electrostatic potential of the 2DES are directly reflected as changes in the current flow through the transistor.

A SET consists of a small metallic island connected to source and drain contacts with two tunnel junctions (see Fig. 3.6a). For current flow to occur through this device, an electron has to hop on the island from the source lead and off the island to the drain lead. Due to the small size of the island, the Coulomb energy for charging the island can not be ignored. This charging energy of the island is given by $U = e^2/2C$, where C is the electrostatic capacitance of the island. It is the energy difference between the top most occupied state and an empty state. If the empty state is not located within the voltage window defined by the voltage applied across the source and drain leads no current can flow. This suppression of current flow is referred to as Coulomb blockade (see bottom panels of Fig. 3.6). Therefore, before an electron can tunnel onto the dot, it has to overcome the charging gap. By applying a gate voltage, V_G, to the 2DES the level $\mu(N+1)$ can be lowered in to the voltage window of the left and right leads, μ_L and μ_R respectively, thus a single electron can tunnel on the island from the left lead and tunnel off the island to the right lead, resulting in current flow.

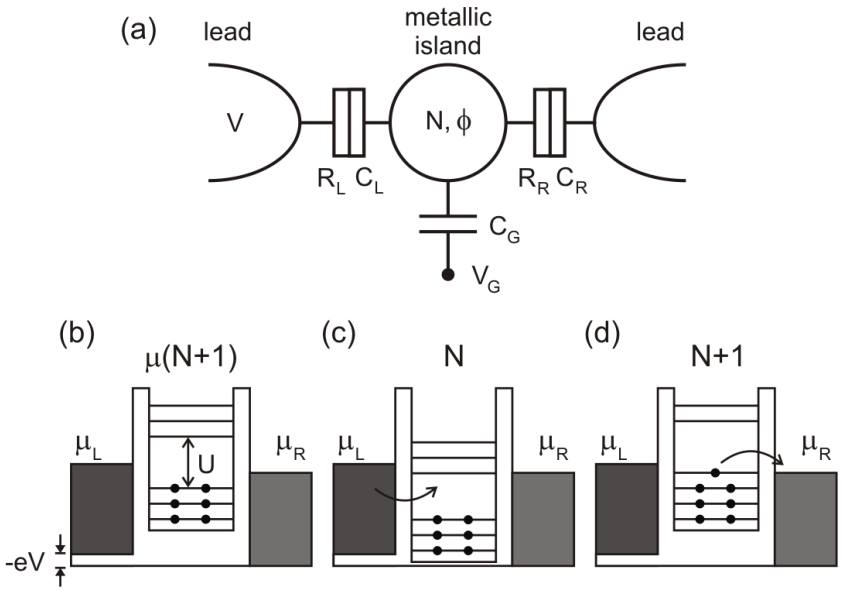

Figure 3.6: (a) Sketch of a single-electron transistor composed of a metallic island, two tunnel junctions and source and drain leads. The gate capacitatively couples to the island. In the panels (b)-(d), the Coulomb blockade is schematically illustrated. In (b) the gate voltage (V_G) is such that the number of electrons on the island remains stable and equal to N. Transport through the island is suppressed. The blockade is lifted when $\mu(N+1)$ is lowered so that it lies between the Fermi levels of the left and right leads (c). The island can then be charged and discharged and a non-zero current flows (d).

This process is repeated with increasing V_G for each charge state, leading to the so-called Coulomb-blockade oscillations [52, 53].

3.3.3 Measurements of the Electronic Compressibility

The local compressibility measurements were performed in a top-loading dilution refrigerator (Oxford Kelvinox TLM ^{3}He/^{4}He Dilution Refrigerator) with a base temperature of less than 20 mK. To carry out the compressibility measurements, it is essential to choose properly the working point of the SET, where it has maximal sensitivity. This is done in two steps. First, by analyzing the I-V curve of the SET as a function of V_{2D}, one obtains the voltage $V_{SET} = (\mu_L - \mu_R)/e$ where the transistor has maximal sensitivity. Secondly, when keeping V_{SET} fixed to this value, the optimal voltage V_{2D} where the $\delta I_{SET}/\delta V_{2D}$ is maximum is

determined. This is the optimal working point of the SET (see Fig. 3.8). Once the working point is set, it is possible to start the measurements of the electronic compressibility.

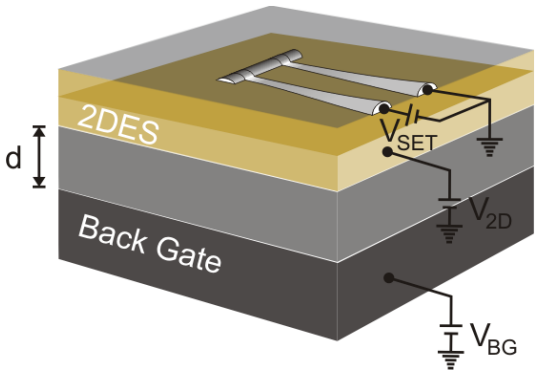

Figure 3.7: (a) Schematic illustration of the experimental set-up in the local probe studies. Here d is the separation between the 2DES and the back gate.

As explained in section 3.3.1, a DC bias is applied to the back gate in order to set the average density. On top of this constant bias, a small AC modulation is added at a frequency of 23 Hz, δV_{BG}, using a function generator (Stanford Research Systems Model DS345). It induces a small density modulation δn. An AC current signal through the SET, $\delta I_{SET}/\delta V_{BG}$, will appear. It is recorded using a lock-in amplifier (Lock-In Amplifier model SR830 DSP). To convert the detected AC current into a change of the chemical potential, $\delta\mu/\delta n$, it is necessary to know the sensitivity of the SET. The sensitivity can be measured by applying a second AC excitation at a different frequency of 33 Hz to the 2DES (instead of the back gate), δV_{2D}. The current response of the SET at this 33 Hz is measured with the help of a second lock-in amplifier, $\delta I_{SET}/\delta V_{2D}$. Combining the two signals it is possible to determine the compressibility of the 2DES in the following way:

$$\frac{\delta I_{SET}/\delta V_{BG}}{\delta I_{SET}/\delta V_{2D}} = \frac{\delta V_{2D}}{\delta V_{BG}} = \frac{C_g}{e^2}\frac{\delta \mu_{2D}}{\delta n_{2D}} \simeq \frac{\epsilon}{n^2 e^2 d}\frac{1}{\kappa} \tag{3.4}$$

where C_g and d are the capacitance and the distance between the 2DES and the back gate respectively. ϵ is the dielectric constant.

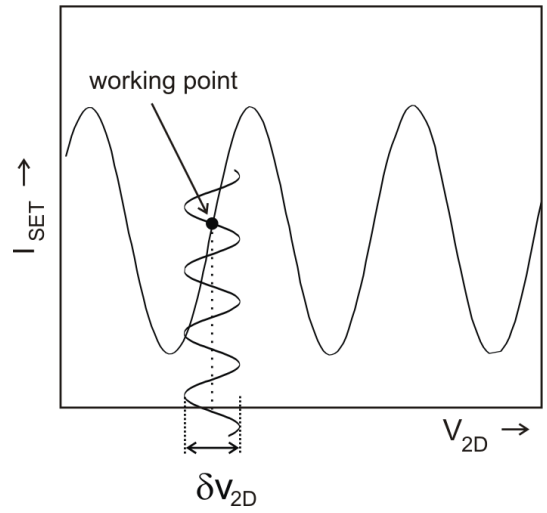

Figure 3.8: (a) Coulomb-blockade oscillations measured at fixed V_{SET} as a function of V_{2D}. The AC excitation δV_{2D} is added on top of the constant DC bias V_{2D} to measure the sensitivity of the SET.

Chapter 4

Electronic Liquid-Crystal Phases in the Quantum Hall Regime

4.1 Introduction

In the past decade strong evidence has been found for the spontaneous development of charge textures in a wide variety of electron systems with strong correlations. Among these, one might mention high-T_c superconductors [54,55,56] and quantum-Hall systems [13,14,15,8]. This tendency of the charge degree of freedom to form periodic spatial patterns is a generic feature of systems where there is a competition between repulsive and attractive forces acting on different length scales [57, 58]. A growing body of experimental [13, 14] and theoretical [15, 59, 60] evidence supports the existence of charge textures in the 2DES when high index Landau levels are partially filled.

Lilly et al. [13] as well as Du et al. [14] discovered that when a very high mobility 2DES ($\mu > 10^7 m/Vs$) is subjected to a perpendicular magnetic field of moderate strength so that multiple Landau levels ($N \geq 2$) are occupied, remarkable transport anomalies arise. Such anomalies include a strong temperature-dependent anisotropy in the longitudinal resistance when the topmost Landau level (LL) with high index is half filled. Even though the anisotropy is most pronounced at half filling of the LL, it remains considerable in a window of about $\Delta\nu \approx 0.2$ around this point. Unlike the conventional transition between plateaux, $\Delta\nu$ does not shrink as the temperature is lowered. In this same $\Delta\nu$ range, the Hall resistance varies continuously with filling. Further away from half filling, the transport is essentially isotropic

but exhibits re-entrant integer quantum Hall behavior close to one-quarter and three-quarter fillings of the level.

4.1.1 Anisotropy

Figure 4.1 shows two longitudinal resistance traces and the Hall resistance taken at T=34 mK on the LP8-9-01.2 wafer with a mobility of $18 \times 10^6 cm^2/Vs$. The two traces differ only in the contact configuration used for the measurement. All the parameters, such as the temperature and the magnitude of the current (10 nA), are kept identical in both data sets. One can observe that the longitudinal resistance (R_L) around $n + 1/2$ filling, where $n = 4, 5, ...$, develops a strong dependence on the direction of the current. At these positions, R_L shows a strong peak when the current is injected along the $[1\bar{1}0]$ direction (black curve), while a deep valley develops after rotating the current direction by 90^o (red curve), i.e., when the current flows along the $[110]$ direction. Apparently, the low resistance path prefers to be aligned along the $[110]$ direction. At present, the native symmetry breaking field responsible for this preferential orientation of the easy-axis still remains enigmatic [61,62,63]. However, subsequent studies have revealed that by tilting the magnetic field away from the sample normal, the high resistance direction can be changed from its original orientation to the in-plane magnetic field direction [64,65]. The direction of the anisotropy also flips by 90^o as a function of the density [66]. Equally striking is the fact that no anisotropy is found around $\nu = 7/2$ and $\nu = 5/2$ [1]. Although not shown in the figure, these resistance anisotropies around half-filling are also absent in the lowest Landau level $N = 0$. This suggests that something dramatic is happening to the ground state of the 2DES as soon as the third and higher LLs become populated. Based on this observation, together with the spontaneous development of the anisotropy as the temperature is lowered below 100 mK [67], suggest that a collective effect rather than a single-particle effect is responsible for these transport anomalies.

[1] The longitudinal resistance in the vicinity of $\nu = 5/2$ and $7/2$ becomes strongly anisotropic as the sample is tilted [64].

4.1.2 Re-entrant quantum Hall behaviour

Anisotropic transport is not the only interesting feature in the transport in high index Landau levels. Figure 4.2a shows a blow-up of the data of the same 2DES when the spin up $N = 2$-LL is filled ($4 < \nu < 5$). Apart from the anisotropy around $\nu = 9/2$ in the longitudinal resistance, one can observe that the resistance drops essentially to zero near $\nu = 4.25$ and 4.75, as indicated by the arrows (and labeled with RIQHE). This vanishing of R_L separated from the adjacent IQH states by small isotropic satellite peaks, which shrink as T is lowered, suggest that FQH states may be present. Indeed, these zero resistance states are accompanied by plateaux in the Hall resistance, but they are quantized at the Hall resistance of the nearby integer quantum Hall states $h/4e^2$ and $h/5e^2$. Hence, FQH states can be discarded as the origin of these insulating phases. As we discussed in chapter 2, the IQHE results from the localization of quasi-particles in the disorder potential. Thus, the re-entrance of the IQHE away from the precise integer fillings, reflects that these quasi-particles become localized again, even when their density increases. It seems likely that a mechanism alternative to single-particle localization is at work, which gives rise to a collective insulating state.

4.2 Theoretical Approaches

Two years prior to the experiments of Lilly et al. [13] and Du et al. [14], Koulakov et al. [15] and Moessner et al. [59] suggested on the basis of Hartree-Fock calculations that Coulomb interactions may lead to stripe or charge-density wave (CDW) formation close to half filling of high index LLs. Numerical exact diagonalization studies on a 2DES with 12 electrons in the $N \geq 2$ LL showed consistency with this charge-density-wave-ordering in the system [68]. However, the temperature dependence can for instance not be explained in this oversimplified model. By considering thermal and quantum fluctuations about the Hartree-Fock state, Fradkin and Kivelson introduced a more sophisticated electronic liquid-crystal picture [8, 69, 70] which explains the temperature dependence and captures the key transport features observed. The distinct electronic liquid-crystals that come out of their model are a more realistic scenario for explaining the above described transport phenomena as well as to other results disclosed in our investigations.

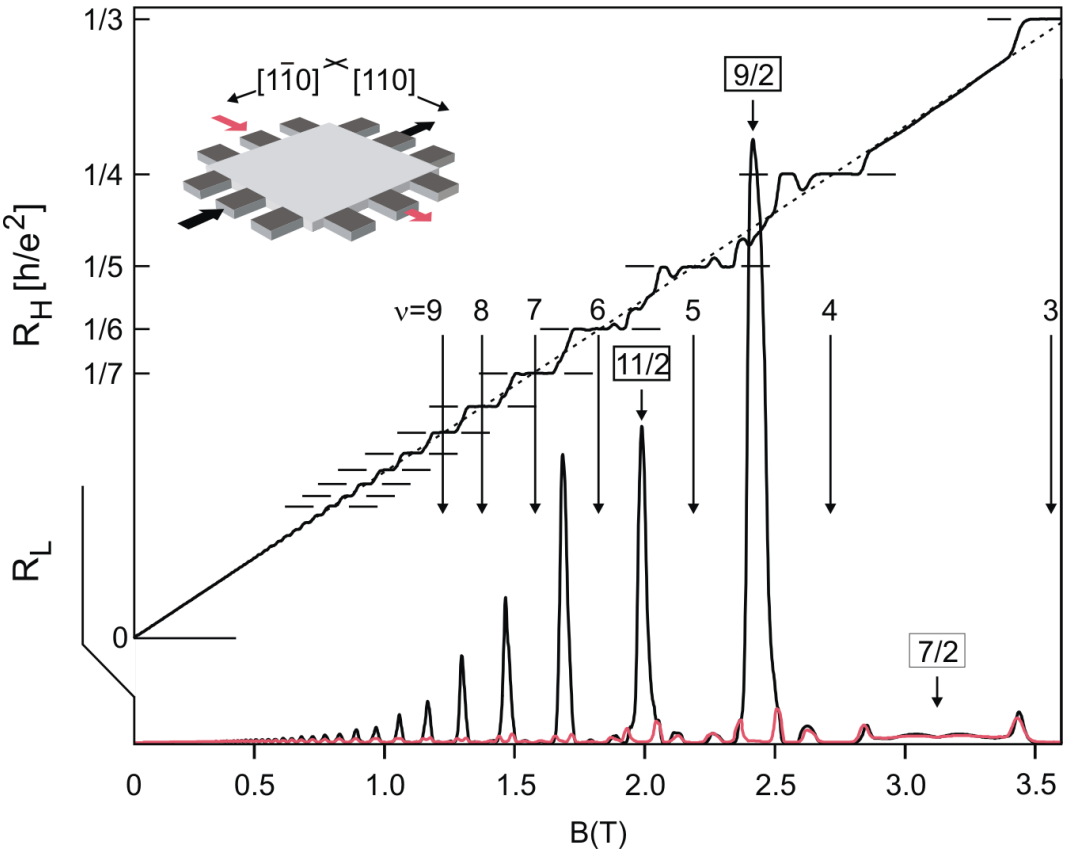

Figure 4.1: Longitudinal resistances R_L for two different orientations of the current: lower black curve for current along $[1\bar{1}0]$ direction and the red curve corresponds to R_L measured with current flow along $[110]$ direction. Also shown is the Hall resistance R_H (upper black curve). Data are taken at $T = 34mK$. A strong anisotropy in R_L develops around $\nu = 9/2$ ($N = 2$ Landau level), whereas transport around $\nu = 7/2$ in the $N = 1$ Landau level is isotropic suggesting that different correlation physics is at work. The inset depicts the current flow configurations in our square van der Pauw mesa geometry for recording these data.

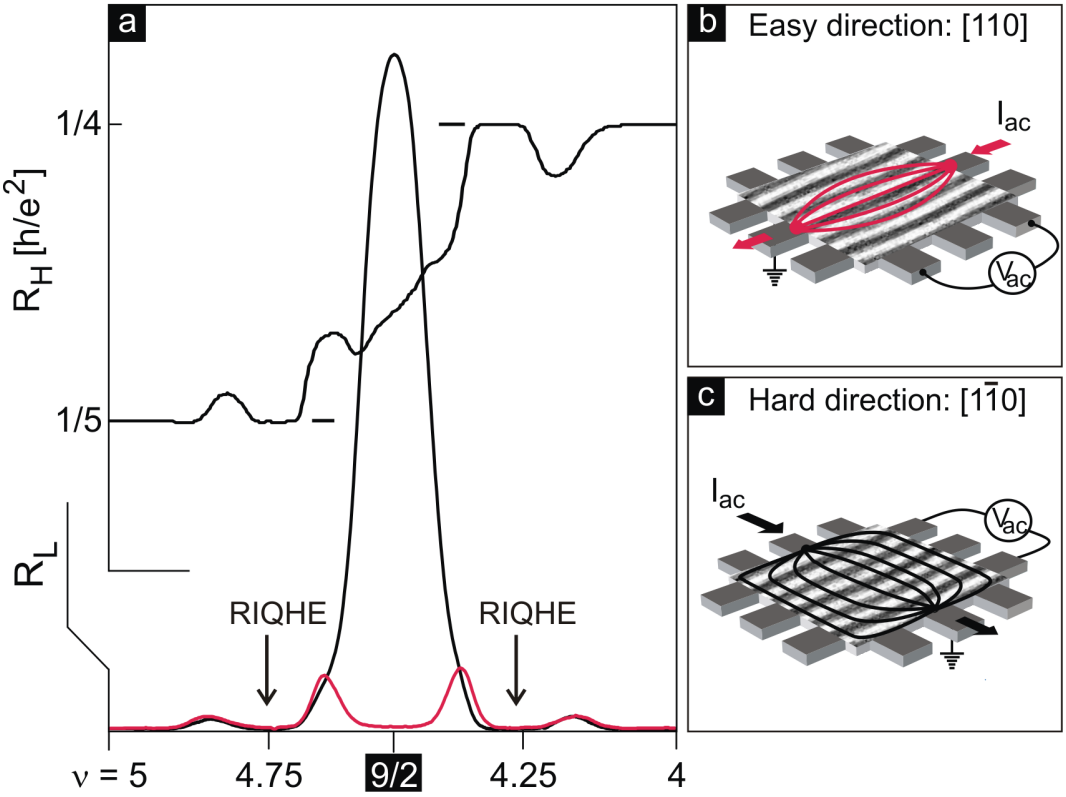

Figure 4.2: (a) Zoom in around $\nu = 9/2$ of Fig. 4.1. Arrows indicate the locations of RIQHE states. Panels (b) and (c) depict the measurement configurations and the corresponding current distribution.

4.2.1 Charge Density Waves

The notion of a charge density wave (CDW) as a possible candidate for the ground state of a 2DES in a perpendicular magnetic field was put forward by Fukuyama et al. [71] even before the discovery of the quantum Hall effect. Their idea was put on the side with the subsequent discovery and explanation of the FQHE, where the Laughlin-type liquid states showed to have energies lower than the states with CDW order. Recent Hartree-Fock calculations by Koulakov et al. [15] and Moessner and Chalker [59] have found that states with CDW order have energies lower than the Laughlin-type states in high index partially filled Landau levels ($N \geq 2$). These calculations focused on the case of zero temperature and have predicted the existence of CDWs of different order. The appearance of CDW with different spatial

configurations is triggered by a competition between the short-range attractive (exchange) and the long-range repulsive (direct) components of the Coulomb interaction. The formation of a striped phase in the Nth Landau level is predicted when it is close to half full, while an isotropic bubble phase is favorable as one moves away from half filling. The striped phase consists of parallel stripes of alternating integer filling factors $\nu = 2N + 1$ and $\nu = 2N$. The width of these stripes is on the order of the cyclotron radius R_c, i.e., on the order of 100 nm. Deviations from half filling leads to an areal increase of the stripes with the majority filling factor until they form a sea with clusters of minority filling immersed in it. The bubble phase consists of these clusters of minority filling factor ordered in a triangular lattice and immersed in the sea of the majority integer filling. The same calculations predicted that in the flanks of the Landau level a hierarchy of bubble phases, where the number of electrons per bubble changes from ...3,2 and eventually 1, which corresponds to a Wigner crystal (a triangular lattice of one-electron bubbles) [72], as one approaches integer filling. A density-matrix renormalization group study has supported this conclusion [73].

Now let us discuss the formation of the correlated phases in high Landau levels. It is known that a conventional charge density wave is favored by the exchange interaction and suppressed by its high electrostatic energy cost [74]. However, in high Landau levels one can form a charge density wave without incurring the electrostatic energy cost. To understand how this can happen, let us consider the shape of the wave function for electrons in high Landau levels. In the symmetric gauge, the wave function of single electron state resembles a ring [15, 23], which has a diameter given by the cyclotron radius $R_c = \ell_B\sqrt{2N+1}$ (N is the LL index) and a width given by the magnetic length $\ell_B = \sqrt{\hbar/eB}$ (see Fig. 4.3c). This picture of extended rings becomes more exact for high Landau levels (see Fig. 4.3c). Due to the ringlike shape of the wave functions, it is possible to distinguish between the local density of guiding centers (i.e., the filling factor) and the local charge density. While the former is very inhomogeneous, the variations of the latter are rather small. Therefore, what we really have is a guiding center density wave rather than a conventional charge density wave. The energy of the system can be represented as the difference of the Hartree (direct) and exchange components. Since the direct component is sensitive to the charge density variations, it does not increase too much. However, the variations of the filling factor are important. This leads to a considerable gain in exchange energy. Hence, while the gain in exchange energy is considerable, there is not much electrostatic energy penalty to have the guiding centers

cluster into stripes.

The stripe and bubble phase scenarios capture qualitatively the observed transport phenomena (anisotropic transport and re-entrant integer quantum Hall effect) in the experiment. In the stripe regime, all the high mobility samples with densities below [2] $2.9 \times 10^{11}\ cm^{-2}$ show that the hard transport direction (high resistance path) is aligned along the $[1\bar{1}0]$ crystallographic direction, and the stripes are oriented along the $[110]$ direction, which we will refer to as the easy direction. Because current channeling [75], resistance anisotropies in square samples can be as high as $R_{[1\bar{1}0]}/R_{[110]} \approx 3500$, whereas they are substantially smaller for conventional Hall bar ($R_{[1\bar{1}0]}/R_{[110]} \approx 10$) [64].

In square sample, when the current is injected along the easy direction, the current flow is strongly channeled in a narrow region of the sample, as schematically illustrated in Fig. 4.2b. The current density along the sample boundaries is small, and so is the longitudinal resistance measured between two terminals at the boundary parallel with the current flow direction. However, when the current is injected along the hard direction, the current spreads across the entire device (see Fig. 4.2c). Current flows closer to the boundaries and hence, the longitudinal resistance is greatly enhanced, as seen in the experiment.

The bubble phase is susceptible to pinning by the ubiquitous disorder potential. Therefore, its transport properties are dominated by the insulating character of the incompressible sea of integer filling in which the bubbles are immersed. The transport properties are isotropic and identical to those of the nearest integer quantum Hall state.

4.2.2 Electronic Liquid-Crystal Phases

The previous Hartree-Fock-based charge density wave approach suffers from overestimating the temperature at which the correlated phases should form. In such a picture, the stripes, which are assumed to be the origin of the transport anisotropy observed in the experiment, are predicted to melt at a few Kelvin [15, 59]. This contrasts with the experimental observation that the anisotropy appears only below about 150 mK [13, 14]. A more sophisticated treatment of the problem that came to reconcile this discrepancy with experiment was put forward by Fradkin and Kivelson [8]. They suggest that quantum and thermal fluctuations restore the broken translational symmetry in a smectic or striped-state. The resulting phase is a quantum

[2] Zhu et al. observed a density-induced 90^o rotations of the anisotropy axes in transport. The transition density is $2.9 \times 10^{11}\ cm^{-2}$ at $\nu = 9/2$. [66]

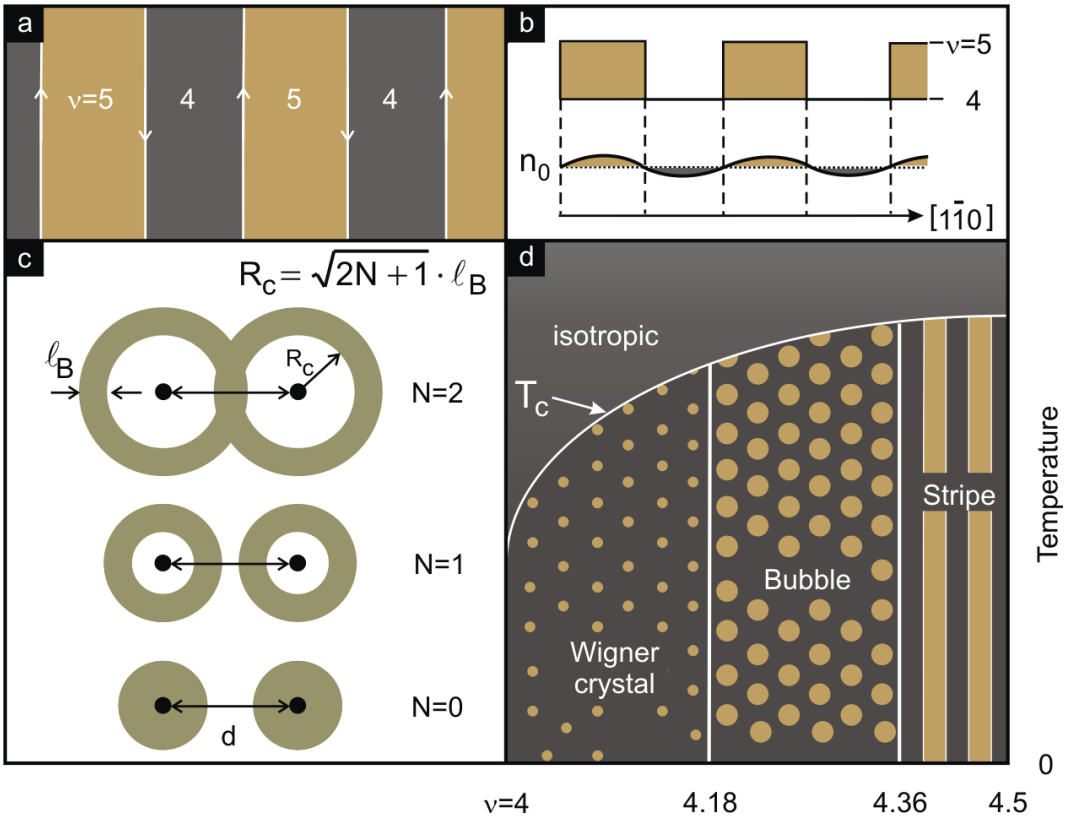

Figure 4.3: Charge density wave picture (CDW). (a) Schematic illustration of striped-state at $\nu = 9/2$ predicted by Hartree-Fock theory. This state can be viewed as a periodic repetition of stripes with integer filling. (b) Modulation of the filling factor (top), and the resulting electron density variation (bottom) along the $[1\bar{1}0]$ crystal direction (hard-direction). (c) Cartoons of the electron wave function in the symmetric gauge. As the LL index increases, the wave function turns into a ring with larger diameter and smaller width. The ring-like shape of the wave functions become more evident as the Landau level index increases. Taking into account the average interparticle distance, the wave functions start to overlap significantly. (d) Phase diagram according to the CDW-picture for the $N = 2$ Landau level. The correlated phases in this level are the stripe phase, the bubble phase and the Wigner crystal. They cease to exist above a critical temperature T_c, and turn into an isotropic liquid.

nematic state with uniform charge density. Although in a nematic state the translational symmetry is recovered, the rotational symmetry remains broken and is sufficient to account for anisotropic transport due to the orientational ordering of local regions with pre-existent stripe order. Wexler and Dorsey [76] found that a nematic-to-isotropic phase transition occur at a temperature of 200 mK, which is not far from what is observed in the experiment. Within the model of Fradkin and Kivelson, moving away from half-filling, an insulating stripe-crystal phase composed of pinned stripe segments is also predicted. A subtle characteristic of the stripe-crystal phase is its anisotropic nature, which is difficult to disclose by using simple transport studies because this phase is insulating in nature. One of main results of our studies concerning these states is precisely the anisotropic nature of the stripe-crystal phase. For the sake of completeness, we note that all these new states of matter [77] predicted by the so-called electron-liquid crystal model have symmetries intermediate between those of a homogeneous isotropic liquid and a crystalline solid [78, 79](see Fig. 4.4e).

Fradkin and Kivelson considered the existence of the striped-CDW state as starting point. The regions of alternating integer filling factor $\nu = 2N + 1$ and $\nu = 2N$ have Hall resistances quantized to the values $h/e^2(2N + 1)$ and $h/e^2(2N)$, respectively. It follows from the Büttiker formalism that 1D conducting edge states form at the boundary between two regions of differently quantized Hall resistance. Because of the magnetic field, these edge states are chiral (see Fig. 4.4a). In contrast to the edge states at the boundaries of a quantum Hall device which are generated by the confinement potential at the boundaries of the sample (see section 2.2.1), the chiral edge states of the ELC phases form self-consistently by virtue of the Coulomb interaction.

Since the ELC edge states are separated by a distance on the order of the cyclotron radius, their mutual interaction cannot be ignored. As shown in Fig. 4.4a, the distance between the ELC edge states of opposite chirality is D_{2N+1} and D_{2N} for edges bordering a $\nu = 2N + 1$ and $\nu = 2N$ region respectively. For a half filled Landau level both distances are equal. Away from exact half filling one distance increases at the expense of the other. It is advantageous to pair up nearest neighbor ELC edge states and represent each pair as a single non-chiral Luttinger liquid. This type of liquid is a strongly correlated electron systems that are described by an internal interaction parameter D [80], which is derived from the distance between the pair of chiral ELC edges states that form the one-dimensional liquid.

Due to the Coulomb interactions among the electrons in the Luttinger liquid, a Luttinger

liquid displays charge-density fluctuations along its extended axis, i.e., along the x-axis in Fig. 4.4b. These charge-density fluctuations are characterized by a wavelength, $\lambda_{Lutt.}$ given by the internal interaction parameter according to

$$\lambda_{Lutt.} = \frac{4\pi\ell_B^2}{D}. \tag{4.1}$$

As mentioned before, D depends on the distance between the ELC edges states and hence the wavelength $\lambda_{Lutt.}$ depends directly on the filling factor.

In the ELC-picture, there are two types of quantum fluctuations that change fundamentally the character of the ground state of the system. The first type of fluctuations corresponds precisely to the charge-density fluctuation along the Luttinger liquids. The second type of quantum fluctuations are related with the fact that the striped-phase is spontaneously generated. This introduces transverse fluctuations on the shape of each stripe, whose physical origin are the Goldstone modes that appear whenever a continuous symmetry is spontaneously broken [81]. These shape fluctuations are characterized by their magnitude given by ΔY (see Fig. 4.4b).

The phase diagram of the ELC is schematically depicted in Fig. 4.4d. Along the horizontal axis the evolution of the phases is plotted as a function of partial filling of the highest occupied Landau level. The evolution of the phases with increasing the magnitude of the transverse fluctuations is plotted along the vertical axis. In the absence of shape fluctuations, the state of the system is crystalline. Charge fluctuations are responsible for the appearance of the smectic phase. The strong interaction between neighboring Luttinger liquids, causes a phase locking of the shape fluctuations. This may enhance the fluctuations until the stripes break up into segments and the stripe-crystal state forms. Since this crystalline state is bound to be pinned by impurities, it will be insulating. In the vicinity of $\nu = 2N$ the triangular Wigner crystal emerges.

Along the vertical axis, the strength of the fluctuations increases. The smectic order is destroyed in a sequence of two transitions. The first transition occurs when the magnitude of the transverse motion of the stripes becomes comparable to their spacing. It triggers a transition to a quantum nematic phase. The nematic phase has short-range stripe order and broken rotational symmetry (see Fig. 4.4e). Such a smectic-to-nematic phase transition is driven by dislocations which destroy the stripe long-range ordering. These topological defects are produced when two stripes merge or a single one terminates (see Fig. 4.4c). A second transition to an isotropic liquid takes place when the shape fluctuations become sufficiently strong so

that the density of dislocations reaches a point where the stripes have no preferred direction anymore. In this case, the system has recovered both translational and rotational symmetries (see Fig. 4.4e).

Finally, let us mention some of the salient experimental signatures of these electronic liquid-crystal phases in transport studies: The transport through the smectic phase is highly anisotropic. The smectic state is compressible and does not exhibit a quantized Hall resistance. In the nematic phase, the transport remains anisotropic due to the local orientational order of the stripes. This phase is also compressible. The stripe and Wigner crystal phases are insulating since they are pinned by disorder. Experimentally, the stripe-crystal phase shows a re-entrant integer quantized Hall resistance because the transport properties are determined by the incompressible $\nu = 2N$ liquid.

4.3 Correlated Phases in HLL under Driven Conditions

4.3.1 Introduction

The correlated electronic phases in high Landau levels (HLL) predicted in the CDW and ELC models near half and quarter fillings will be referred to, from now on, as the equilibrium or nondriven phases of the system. Here, we investigate these correlated phases in transport under non-equilibrium conditions by imposing an external dc current drive[3]. These studies were motivated by a number of questions: Is it possible to induce a different order or a reorientation of the anisotropy upon driving the system? Can evidence be found in favor of the anisotropic stripe crystal rather than the isotropic bubble phase to describe the system near quarter fillings?

In our experiments, the variable external dc current drive I_{dc} was imposed in a floating configuration either along the $[110]$ or the $[1\bar{1}0]$ crystal directions, i.e., the easy or hard direction of the stripe or nematic phase respectively. To probe for any dc current induced anisotropies or modifications to the order or orientation of these phases, the resistances along and perpendicular to the dc current were compared. To measure these resistances, an additional small sinusoidal current I_{ac} with a frequency of 13 Hz and an amplitude of 10 nA was applied in either direction. The drain contact for the ac current was connected to ground. The

[3]The ac current is comparatively small, and barely disturbs the system. Hence, in the absence of the dc current drive the system exhibits the "equilibrium" phases.

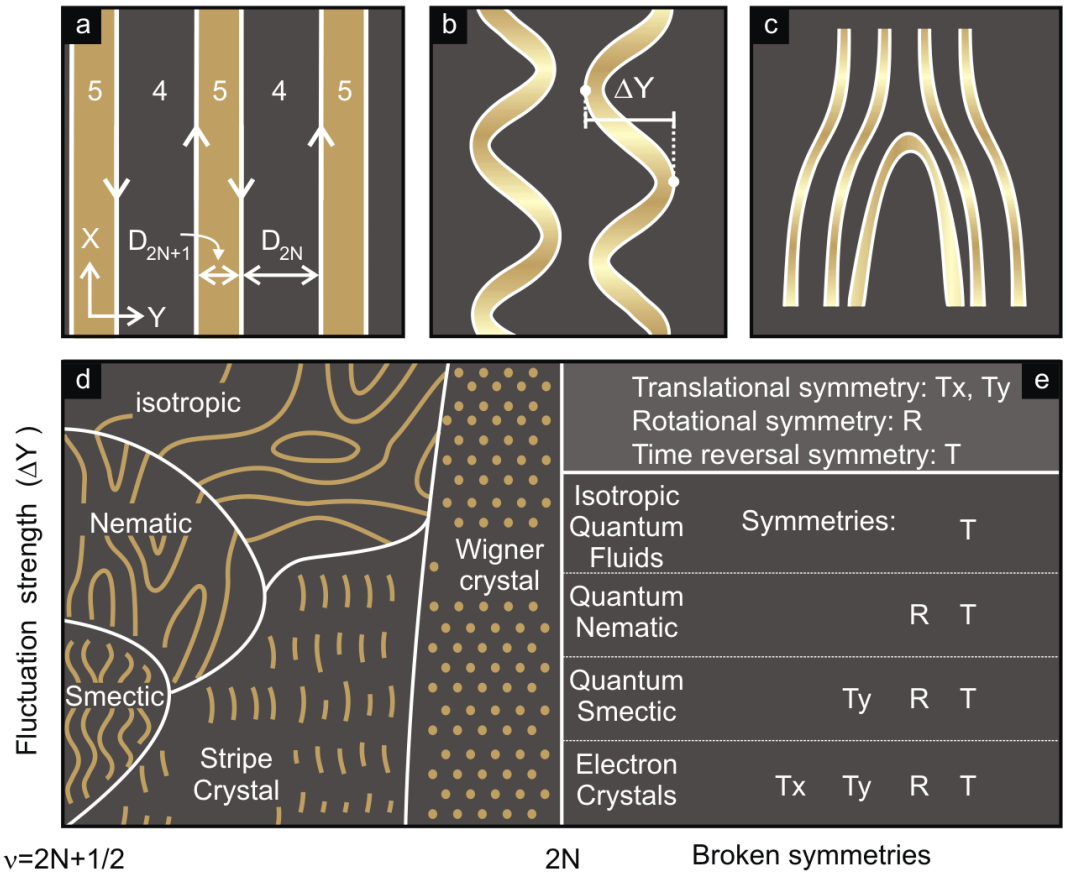

Figure 4.4: Electronic liquid-crystal picture (ELC). (a) Schematic view of the stripe phase with filling factor somewhere between $\nu = 9/2$ and $\nu = 4$. Here, edge channels bordering a $\nu = 5$ region become strongly coupled, while the interaction between the edge channels running along the border of the $\nu = 4$ region weakens. (b) The quantum fluctuations of two neighboring edge channel pairs. The amplitude of the transverse deformations of the stripes are denoted by ΔY. (c) A dislocation in a nematic phase. (d) Phase diagram at $T = 0$ as predicted by the ELC-picture. Here, we plot the strength of the transverse motion of the stripes on the vertical axis. The horizontal axis is the filling factor axis and covers the filling range between $2N$ and $2N + 1/2$ of the N-th partially filled Landau level. The gold colored lines represent the non-chiral Luttinger liquids, which form away from $\nu = 2N+1/2$ when the two chiral edge states surrounding the $\nu = 2N+1$ regions become strongly coupled. (e) Classification of the phases of a 2DES with a partially filled Landau level with index $N \geq 2$, according to their broken symmetries.

ac voltage V_{ac} which developed across two terminals along the ac current path was detected with a lock-in amplifier.

A typical outcome of our transport experiments under non-equilibrium conditions is displayed in Fig. 4.5. This color plot shows the resistance $R = V_{ac}/I_{ac}$ as a function of filling factor, ν, and dc current, I_{dc}, for a 500 μm square sample. Red corresponds to large resistance, and dark blue to zero resistance. The sample details are described in Sec. 2.1. These data were obtained when I_{ac} and I_{dc} are directed in the hard $[1\bar{1}0]$-direction, i.e., perpendicular to the stripes. The inset in the top left corner depicts schematically the current flow and voltage measurement arrangement. Data points making up this color graph were recorded by keeping I_{ac} fixed to 10 nA, while I_{dc} was ramped up from -500 to 500 nA in 5 nA steps. For each value of I_{dc} the magnetic field was swept between 1.4 and 3.85 T. For the next I_{dc} value the field was swept down and so on.

At first glance, the resistance around half and quarter fillings from $\nu = 4$ through $\nu = 15/2$ develops a dependence on the dc current drive that is absent in the $N = 1$ Landau level. This dramatic difference is an important indicator that something interesting is happening in partially filled high Landau levels when driving the system. To describe the influence of I_{dc} on the correlated phases in HLL more precisely, let us focus on the filling factor range between $\nu = 4$ and $\nu = 5$.

4.3.2 Basic Phenomenology

Fig. 4.6 shows a color map of the resistance $R = V_{ac}/I_{ac}$ in the (ν, I_{dc})-plane, for a 300 μm square sample. In this measurement the (I_{ac}, I_{dc})-configuration is such that both I_{ac} and I_{dc} run perpendicular to the direction of the stripes. Cartoons of the equilibrium or nondriven phases in the CDW and ELC models are plotted above the color rendering. When following the line $I_{dc} = 0$, one obtains the resistance profiles at the top. The large peak in R, which develops around $\nu = 4.5$, is attributed to the stripe or nematic phase since the hard direction is probed. The incompressible behavior of the bubble or stripe-crystal phase is manifested as vanishing resistance around $\nu = 4.25$ and $\nu = 4.75$. This region of vanishing resistance is separated from $\nu = 4$ and $\nu = 5$ quantum Hall minimum by a poorly and well-developed resistance peak respectively. Introducing I_{dc} as a parameter brings out clearly the phase boundaries. The stripe or nematic phases cover the filling interval $[4.36, 4.64]$. The adjacent bubble or stripe-crystal phases extend over filling intervals $[4.18, 4.36]$ and $[4.64, 4.82]$.

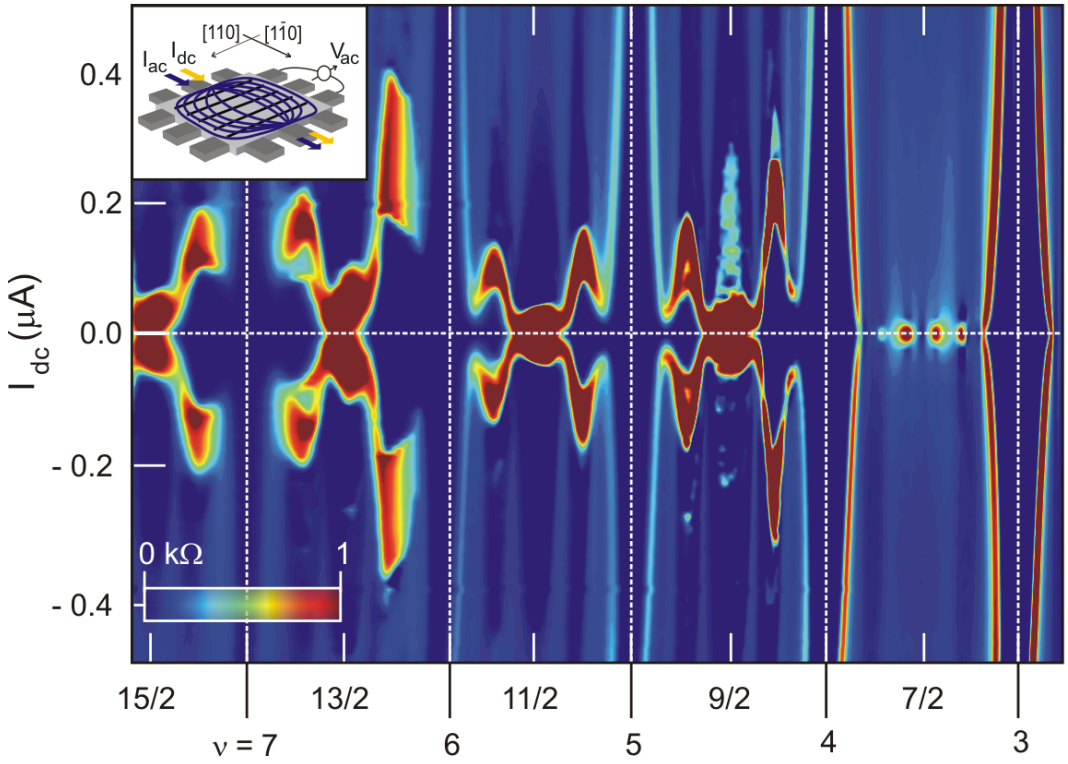

Figure 4.5: Color map of the resistance $R = V_{ac}/I_{ac}$ between filling factor $\nu = 3$ and $\nu = 15/2$ at a temperature less than 20 mK for a 500 μm square sample. The data were acquired when both I_{ac} and I_{dc} flow along the $[1\bar{1}0]$-direction (inset in top left corner). The behavior in the $N = 1$ Landau level (around $\nu = 7/2$) is very different in comparison with the higher Landau levels (around $\nu = 9/2, \cdots, 15/2$).The bar in the bottom left corner gives the color scale.

Stripe or Nematic Phase Regime

Let us first focus on the filling interval $[4.36, 4.64]$ where at zero I_{dc} the stripe or nematic phase forms. By monitoring R as I_{dc} is varied from zero, one can observe that the differential resistance collapses: transition from red to blue near $|I_{dc}| \approx 50 - 60$ nA. Subsequently, at higher current levels, the resistance remains low across an area (dark blue) which resembles a diamond shaped region. This region is demarcated by a white dotted line. It is worth mentioning the abrupt change between high and low resistance. Though it is not a conclusive proof, it suggests that the observed behaviour does not simply originate from Joule heating.

Also note the behaviour of the resistance maximum in the stripe phase regime. This

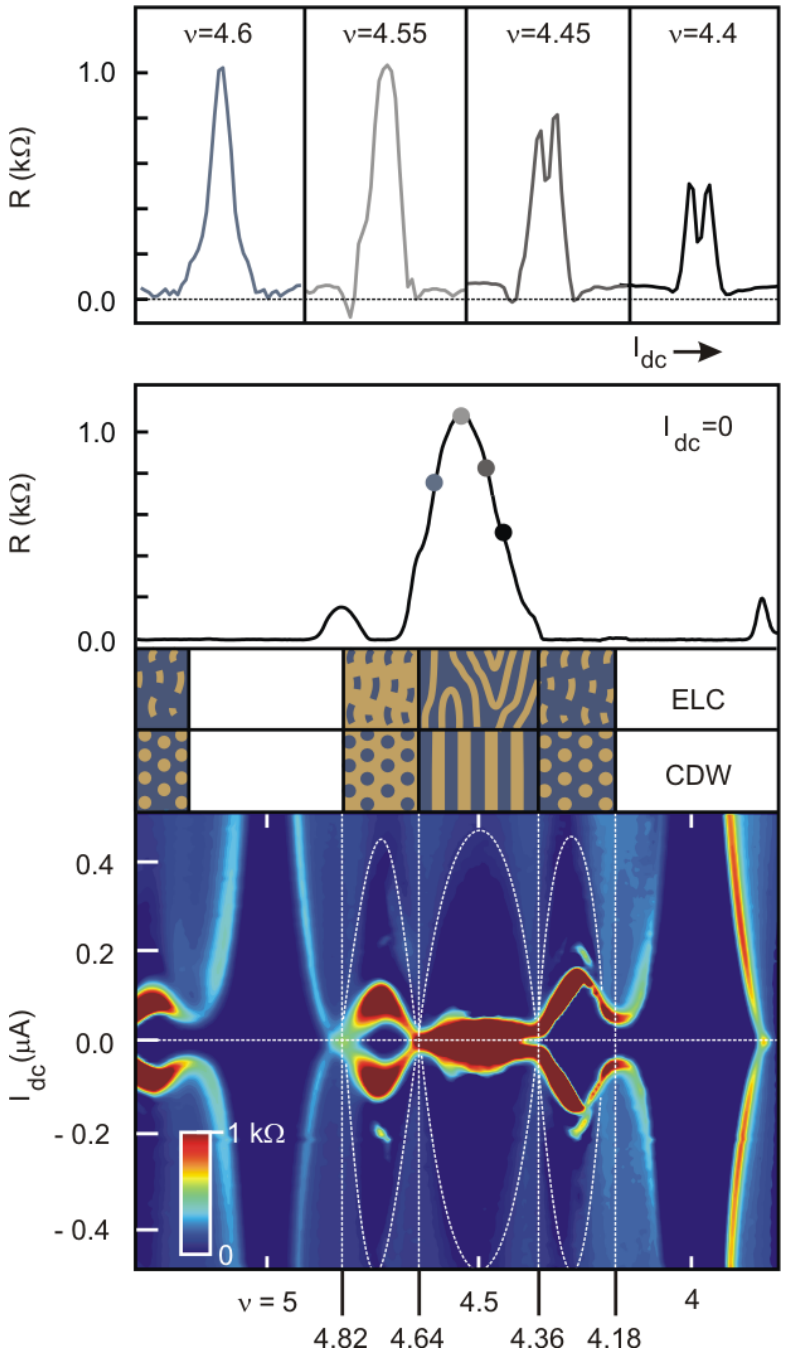

Figure 4.6: Color map of the resistance $R = V_{ac}/I_{ac}$ in the (ν, I_{dc})-plane at a temperature less than 20 mK for a 300 μm square sample. Red corresponds to high resistance, blue to zero resistance. Here, both I_{ac} and I_{dc} flow along the hard $[1\bar{1}0]$-direction. Cartoons of the equilibrium phases in the CDW and ELC pictures are drawn above the color map. Middle: Resistance at $I_{dc} = 0$ as a function of filling factor. Top: Resistance versus I_{dc} for four different filling factors near $\nu = 9/2$. In each case, I_{dc} varies from -100 to 100 nA.

observation is summarized in the top panels of Fig. 4.6. For each panel, the dc current is swept from $-100nA$ to $+100nA$. One can observe a splitting of the resistance maximum for partial filling factors above $\nu = 9/2$. This observation is conform to early studies carried out by Eisenstein's group at Caltech [82].

Bubble or Stripe Crystal Phase Regime

We now focus on the electron and hole-bubble phase regimes, which cover the filling intervals $[4.18, 4.36]$ and $[4.64, 4.82]$ respectively. In these regions, the resistance remains close to zero until I_{dc} reaches approximately 110 nA in the electron-bubble phase and 40 nA in the hole-bubble phase. At these currents, the resistance in the system increases abruptly and develops a nearly identical value compared with the resistance in the striped phase around $\nu = 4.5$ at zero I_{dc}. Large resistance is only observed in a narrow region bordering a rhomb. This red region coalesces together with high resistance region near $\nu = 4.5$ into a frog shape. Upon increasing the dc-current further, the resistance collapses in a similar fashion to the drastic drop which occurred around $\nu = 4.5$. After this drop, the resistance remains small (dark blue) within a diamond shape nearly identical in height to the large diamond within the stripe phase. These diamond shaped regions are demarcated by a white dotted line.

The physics of the 2DES within a given Landau level is expected to be symmetric with respect to half filling because of particle-hole symmetry [83]. An important sign for particle-hole symmetry in HLL is that bubble phases are present for electrons and holes. We note, however, that the particle-hole symmetry is not obeyed well in the data when we compare the dc current at which the insulating behavior around one-quarter and three-quarter fillings disappears: $I_{dc} \approx 110$ nA and $I_{dc} \approx 40$ nA respectively. This asymmetry is also visible in the activation energies, Δ, of the electron and hole-bubble phases: $\Delta_{1/4} \approx 100$ μeV and $\Delta_{3/4} \approx 60$ μeV [84]. Also other examples where particle-hole symmetry is not fulfilled at a quantitative level will be encountered later.

4.4 Current-Induced Phenomena in the System

The abrupt changes in the resistance observed in Fig. 4.6 around half and quarter fillings point to current-induced modifications in the order or orientation of the correlated phases. In this section we present the results of a systematic study carried out on devices fabricated

from the same heterostructure as the one used to obtain the data presented in Fig. 4.6. To carry out these investigations, the independent choice of the drive (I_{dc}) and probe (I_{ac}) current directions in the experimental setup has been crucial. The experimental setup was described in Sec. 3.2.

Fig. 4.7 depicts color renderings of the measured resistance $R = V_{ac}/I_{ac}$ between integer filling 4 and 5 for the four possible (I_{ac},I_{dc})-configurations in a 300 μm square sample. At zero I_{dc}, the anisotropic behaviour in transport of the stripe phase near $\nu = 9/2$ manifests itself as a large color difference: red when I_{ac} flows in the hard $[1\bar{1}0]$-direction perpendicular to the stripes (panel A and D) and light blue when I_{ac} is injected along the easy $[110]$-direction, i.e., along the stripes (panel B and C). For the incompressible bubble or stripe-crystal phase near $\nu = 4.25$ and $\nu = 4.75$ vanishing resistance is obtained irrespective of the ac current orientation (dark blue) and the phases appear the same way as the adjacent integer quantum Hall states do.

4.4.1 Stripe or Nematic Phase Regime: Description

As in Sec. 4.3, we first focus on how I_{dc} affects the system in the filling interval $[4.36, 4.64]$, where the stripe or nematic phase appears. The bottom panels show data when I_{dc} is injected along the easy $[110]$-direction. A diamond shaped region of low resistance demarcated by a whitish halo and extending up to $I_{dc} > +300nA$ and $< -350nA$ is observed when monitoring R along the easy direction (panel C). When the system is probed along the hard $[1\bar{1}0]$-direction, high resistance persists in a nearly identical diamond shaped region (panel D). We now turn to the top panels. These color maps show data when I_{dc} is injected along the hard $[1\bar{1}0]$-direction. Here, the resistance measured along the hard direction (panel A) collapses much earlier near $I_{dc} \approx 50 - 60$ nA and subsequently remains low across an area which resembles the above mentioned diamonds. The drop in resistance is accompanied by a small area of negative differential resistance. Such regions are marked by white contours (The color scale has been clipped at 0 Ω). Even though less clear, when the system is probed along the easy direction the data in panel B imparts similar information: some transition takes place at small I_{dc}.

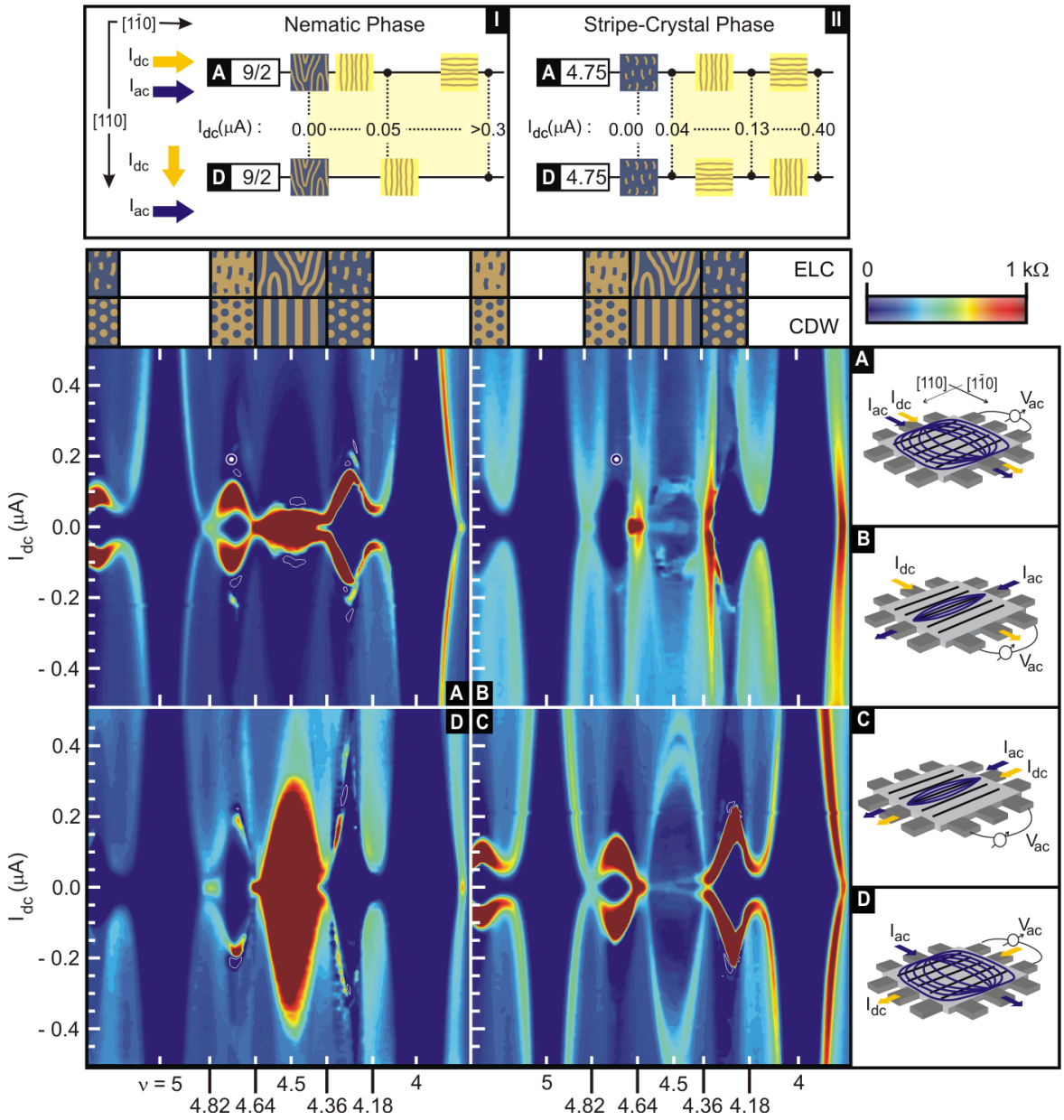

Figure 4.7: Current induced anisotropy and reordering in the ELC-phase. The 2D colour graphs depict the differential resistance V_{ac}/I_{ac} as a function of filling factor, ν, and the dc current, I_{dc} for the four (I_{ac}, I_{dc})-configurations in a 300 μm square sample. White contours enclose regions of negative $R = V_{ac}/I_{ac}$. Cartoons of the equilibrium phases in the CDW and ELC pictures are drawn in the relevant filling factor regions at the top. The right insets indicate the experimental configurations for each measurement. Panels I and II highlight for two (I_{ac},I_{dc})-configurations (configuration A and D) where anisotropy occurs (pale yellow). The yellow pictograms are only intended to indicate schematically how the easy axis is oriented.

4.4.2 Interpretation: Current-Induced Reordering and Stabilization in the Nematic Phase

Taken all together, the data lend strong support for the following scenario: Imposing I_{dc} along the easy direction stabilizes the original anisotropic phase. It survives up to a large critical $|I_{dc}| > 300nA$ where it melts. This is reflected in panel C and D with the nearly identical diamonds of low (blue) and high (red) resistance around $\nu = 9/2$. It is tempting to link the stabilizing influence in the easy direction to a suppression of the transverse shape fluctuations in the ELC picture, i.e., the dc-drive would render the original undriven nematic phase more orderly as addressed theoretically in Ref [85]. Conversely, dc-current flow perpendicular to the easy direction (panel A and B), destabilizes and flips the anisotropy phase at low dc-current to make the easy direction align with I_{dc}. After reorientation this phase persists up to the same critical I_{dc}. The reorientation of the easy axis is likely not global but only local where I_{dc} is channeled once a low resistance dc-current path shorting the dc source and drain contacts is established. The ac-resistance along the I_{dc} direction drops drastically as seen in panel A. The ac-resistance perpendicular to I_{dc} would only change weakly, since the orientational order is only affected in the area where the dc-current is channeled. This is consistent with panel B and the weaker anisotropy seen between panel A and B. Since a stripe or smectic phase is not-uniform and breaks translational symmetry (see Fig. 4.4e), strongly non-linear or pinning associated behaviour such as hysteresis is anticipated for such phases. Early studies carried out in our group disclosed that when driving the system along the hard direction, no hysteresis is observed at $\nu = 9/2$ between R-traces recorded during up and down sweeps of the drive current [84]. The absence of hysteresis too suggests that the less anisotropic and uniform nematic ELC phase better describes the behaviour of the system. The dc current modifies the rotational symmetry and rotates the easy direction of conduction to make it align with the dc-current.

4.4.3 Possible Mechanism of Reordering

At this point one of the most pressing question is: what is the driving force that causes the reordering: the dc Hall electric field or the current itself? To answer this question we have carried out a study of the sample size dependence. Fig. 4.8 depicts the outcome of this investigation. These color maps represent the resistance $R = V_{ac}/I_{ac}$ between integer

filling 4 and 5 for two (I_{ac},I_{dc})-configurations. The experiments were carried out on three different sample sizes: 180, 300, and 500 μm. These samples were fabricated from the same heterostructure used previously. The data in the top panels were acquired when both I_{ac} and I_{dc} are injected along the hard $[1\bar{1}0]$-direction. The bottom panels corresponds to data obtained when I_{ac} and I_{dc} are directed along the hard $[1\bar{1}0]$ and the easy $[110]$-direction respectively. Schematic illustrations of these two (I_{ac},I_{dc})-configurations are displayed in the bottom right panel.

Note that the critical dc-current at which the easy axis rotates to make itself align with I_{dc} (see filling interval $[4.36, 4.64]$ in the top panels of Fig. 4.8) does not scale with the sample size but stays constant. The observation can be understood if one assumes that most of the current flowing through the sample is confined to narrow current paths, whose width remains constant irrespective of the sample size. In this case, it would be reasonable to argue that a critical current density triggers the reorientation. A schematic summary of the easy axis orientation near $\nu = 9/2$ as a function of I_{dc} is shown on the top of Fig. 4.7 (panel I).

4.4.4 Bubble or Stripe Crystal Phase Regime: Description

We now address how I_{dc} affects the incompressible pinned bubble or stripe-crystal phases in filling regions $[4.18, 4.36]$ and $[4.64, 4.82]$ in Fig. 4.7. At small I_{dc} the resistance initially remains isotropic, i.e., independent of the ac current direction, and essentially zero in all the configurations. As I_{dc} reaches approximately 40 nA (near $\nu = 4.75$) and 110 nA (near $\nu = 4.25$) a very pronounced resistance anisotropy develops reminiscent of the anisotropy near $\nu = 9/2$. The resistance rises to a large value (red) in a narrow region bordering a rhomb when I_{ac} flows parallel to I_{dc} (panel A and C) and remains small when imposing I_{ac} perpendicular to I_{dc} (panel B and D). Hence, the hard direction of this emerging anisotropic phase coincides with the direction of the dc-current flow. Upon increasing I_{dc} further, a second transition takes place. In panels A and C the resistance drops back to a low value (from red back to deep blue) near $I_{dc} = 130$ nA for $\nu = 4.75$ and $I_{dc} = 170 - 225$ nA for $\nu = 4.25$ and remains small within a large diamond shape extending all the way up to $I_{dc} = 400$ nA. Conversely, in panels B and D the resistance now suddenly increases (dark blue to light blue) and remains essentially the same within a nearly equally large rhomb. The resistances in panels B and D do not reach as high value (light blue instead of red), but do exceed for instance at the marked spot the resistances in panel A and C by nearly a factor of

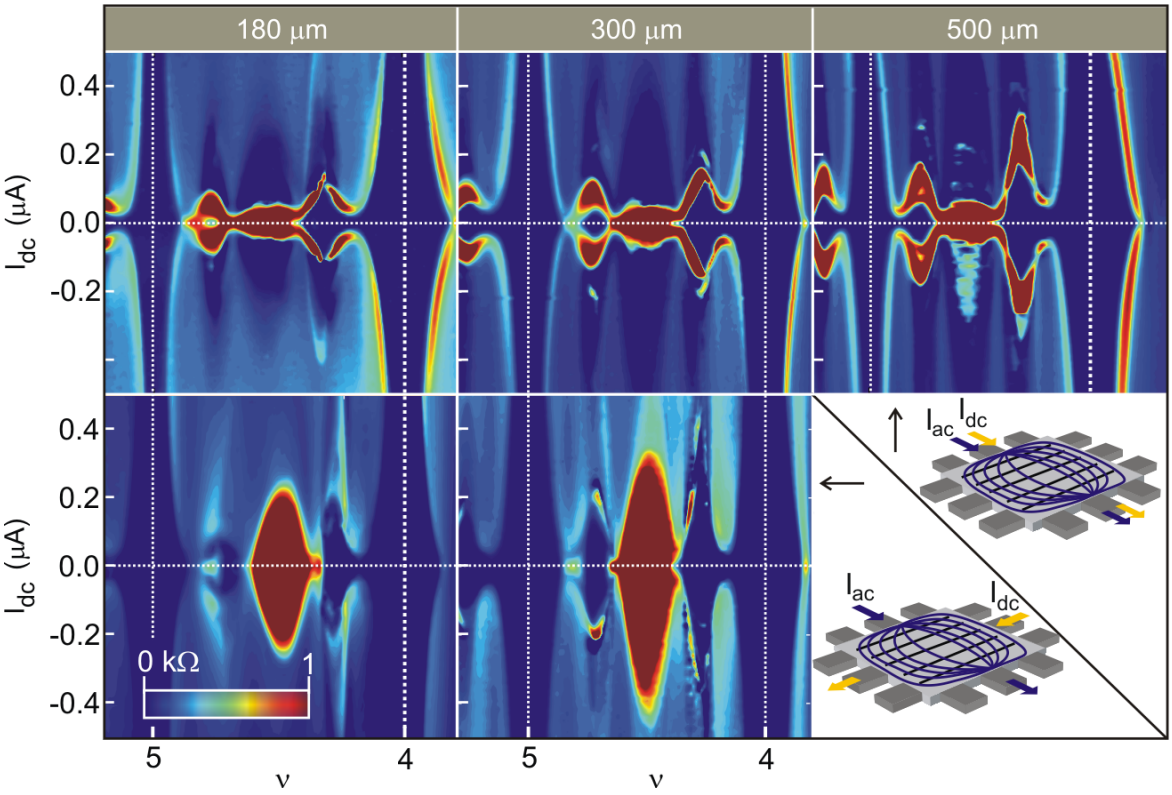

Figure 4.8: Color renderings of $R = V_{ac}/I_{ac}$ in the (ν, I_{dc})-plane for samples with different side lengths: 180, 300, and 500 μm. The data were taken at a temperature less than 20 mK. The bar insert in the bottom left corner gives the color scale. Top: Data acquired when both probe I_{ac} and drive I_{dc} currents are directed along the hard $[1\bar{1}0]$-direction. Bottom: Data acquired when the system is probed along the hard $[1\bar{1}0]$-direction and is driven along the easy $[110]$-direction. The two (I_{ac},I_{dc})-configurations are schematically drawn in the bottom right panel.

3. Hence, the anisotropy persists, but the hard and easy directions interchange. The easy-axis becomes aligned with the dc-current direction.

4.4.5 Interpretation: Current-Induced Anisotropy in the Stripe-Crystal Regime

In a macroscopic transport experiment the bubble and the rectangular or stripe-crystal phases appear isotropic, because they are insulating. At the microscopic level, only the stripe-crystal is anisotropic with the stripe sections extending in a particular direction. It turns this phase into the more natural starting point for constructing an explanation for the observed anisotropy. The data lend support for the following scenario. When imposing a dc drive, the stripe sections become oriented along the dc Hall electric field. i.e., the easy direction is perpendicular to the dc-current. This reminds of the orientation of conventional liquid crystals in an external applied electric field. Depinning by this Hall field combined with the existing stripe order would be in line with the appearance of anisotropic transport. In fact, the nearly identical resistance values of this dc-current induced anisotropic phase and the anisotropic phase near $\nu = 9/2$ as well as the smooth transition between the high resistance areas associated with both phases in panel A (coalescing to the frog shaped red colored area) are indications for an intimate connection between the two. They do differ in that the easy-axis of the nematic phase at $\nu = 9/2$ is prescribed by the underlying crystal axis orientation, whereas here the dc Hall electric field serves as the symmetry breaking field. Up and down sweeps of I_{dc} at fixed filling reveal a pronounced hysteresis near quarter fillings in this regime (see early studies performed in our group [84] and also in Eisenstein's group [86]). The hysteresis is consistent with the depinning of an non-uniform state [87, 88] such as the stripe-crystal. This hysteresis and the sharp threshold to conduction appear identical to the previously reported hysteresis in the dc-experiments of Ref. [86], since the critical current values are comparable when they are normalized to the sample width.

The sample size dependence plotted in Fig. 4.8 shows that the critical I_{dc}, where anisotropic transport emerges, scales roughly linearly with the sample side length. As mentioned above, some of the dc-current is carried by the edge channels of the completely filled Landau levels and produces a bulk dc Hall electric field. The linear scaling of the critical I_{dc} implies an approximately constant dc-Hall field at the depinning transition. This plausible results fur-

ther support the assertion that this transition is triggered by the dc Hall electric field rather than I_{dc} itself. As in Ref. [86], traces taken during up and down sweeps of I_{dc}, such as those obtained in early studies in our group [84], remain quite sensitive to temperatures down to below 20 mK. While the dissipation due to I_{dc} may be responsible for melting near 400 nA (large rhomb) in all panels of Fig. 4.7, it unlikely accounts for this transition nor for the reordering observed at $I_{dc} = 50$ nA around $\nu = 9/2$. Microwave studies in the absence of a dc current disclosed a resonance near quarter fillings, which was attributed to a pinning mode [89]. The strength of this mode was comparable for polarization along the $[110]$ and $[1\bar{1}0]$ crystal directions. This polarization independence is however not necessarily inconsistent with the anisotropic behaviour observed here, since the dc-Hall field determines the easy axis.

4.4.6 Reordering in the Stripe-Crystal Phase

If the above scenario applies, one may then anticipate a reorientation at quarter fillings similar to the reordering seen and discussed previously near $\nu = 9/2$. Indeed, at larger dc drive the orientation of the anisotropic phase seems to make the easy direction align with I_{dc}. After reorientation this phase persists up to $I_{dc} > 400$ nA, where presumably it melts. The much weaker anisotropy again indicates that reorientation of the easy axis only takes place locally. The ac resistance perpendicular to I_{dc} in panels B and D only rises moderately as it is a serial connection of contributions from regions which still have low resistance and from a region to which the dc current is mainly confined with large resistance where reorientation took place. The panel II in Fig. 4.7 summarizes the transformation near $\nu = 4.75$ as the dc drive amplitude grows: Anisotropy develops near $I_{dc} = 40$ nA, which we interpret as originating from a depinned stripe crystal with stripe order that has been aligned along the dc-Hall field. At large I_{dc} (130 nA), the easy-axis of the depinned, anisotropic phase rotates to end up parallel to I_{dc}.

4.5 Alternation in the Resistance along the Hard Direction

Up to this point, all the experiments discussed have been carried out at temperatures below 20 mK. Fig. 4.9 shows magnetotransport data in the third $N = 2$ and higher Landau levels for current flowing along $[1\bar{1}0]$ (the hard direction). These data were acquired at a temperature of 90 mK. Usually, at the lowest temperature, one observes that the resistance peaks near half-filling of the Landau level (LL) gradually decay as the LL index increases. In this experiment, however, one observes that for LL with index $N = 2$ a large peak in resistance occurs around $\nu = 9/2$, but only a small peak develops near $\nu = 11/2$. In a similar fashion in the $N = 3$ LL a large peak occurs at $\nu = 13/2$ and a small peak around $\nu = 15/2$. Although not shown here, this alternation manifests itself starting from temperatures above 50 mK.

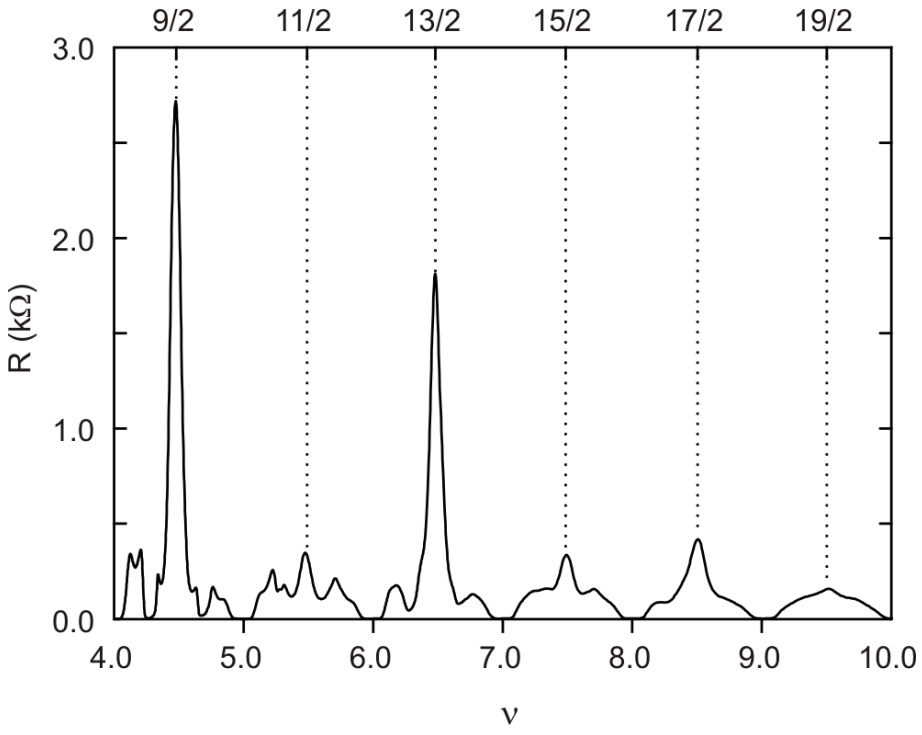

Figure 4.9: Magnetotransport data when the system is probed in the hard direction at a temperature of 90 mK. Note the difference between the resistance peak which develops around $\nu = 9/2$ and $\nu = 11/2$. The same behaviour is observed around $\nu = 13/2$ and $\nu = 15/2$.

We recall that the striped state predicted around half fillings in high LLs consist of alternating stripes with integer filling factor $\nu = 2N + 1$ and $\nu = 2N$ (see Sec. 4.2). It was also

discussed that 1D conducting edge states exist at the boundaries between two regions with different filling factor. MacDonald and Fisher [90] assumed that the current along the easy direction of the striped phase flows in these conducting edge states and formulated a transport theory. In their model, dissipation and transport orthogonal to the stripes occurs via scattering events between adjacent 1D conducting edge channels. Adopting the language introduced by Müller et al. [91], we have denoted the regions with higher filling factor as the well regions, while the regions with lower filling factor are called the barrier regions.

Phenomenologically, the observation can be understood as follows: At filling factor $\nu = 9/2$, the barrier has a height equal to the cyclotron gap. However, for filling factor $\nu = 11/2$, the barrier corresponds to the Zeeman gap. At higher temperatures, the barrier defined by the Zeeman gap will become more transparent than the barrier governed by the cyclotron gap. Backscattering at $\nu = 11/2$ will be suppressed as the probability for tunneling between adjacent 1D conducting edge channels increases. However, at $\nu = 9/2$, the backscattering remains strong. This produces a larger resistance near $\nu = 9/2$ than at $\nu = 11/2$ as observed in the experiment. The same arguments apply to Landau levels with higher index.

Chapter 5

Spin Phase Transition in the Quantum Hall Regime

5.1 Introduction

In recent years it has been recognized that the spin degree of freedom plays an important role for fractional quantum Hall liquids [92, 93]. In early fractional quantum Hall (FQH) studies, it was usually assumed that the electron system is fully polarized. At very strong magnetic field $B_\perp$ all electron spins are aligned and the spin degree of freedom is indeed effectively frozen out. The appearance of the fractional quantum Hall effect is then due solely to Coulomb interactions. However, it was pointed out by Halperin [10] that the assumption of full spin polarization initially used by Laughlin [2] to account for the FQH-states may not be valid at small densities due to the fact that in GaAs-based 2DESs the Zeeman splitting is small. By lowering n_e the FQH regime can be shifted to fields, where spin remains an important extra dynamical degree of freedom, because the Zeeman splitting drops linearly with magnetic field and hence more rapidly than the Coulomb interaction ($\sqrt{B_\perp}$) [10,94,95]. Rich phase transition physics may ensue, since multiple FQH ground states that differ only in their spin configuration compete. Recent photoluminescence measurements confirmed that indeed many of the fractions such as $2/3$ and $2/5$ are not necessarily spin polarized [96].

Transport experiments have disclosed signatures for spin phase transitions at, for example $\nu = 2/3$ and $\nu = 2/5$, from a spin-unpolarized to a fully spin-polarized FQH states as for instance when the density is increased. Tilted-field experiments performed by Eisenstein et

al. [97] showed the first evidence for a spin phase transition in the $\nu = 2/3$ FQH-state. They observed that the resistance at $\nu = 2/3$ exhibited reentrant behavior, i.e., the state would weaken, then later revive as the sample was rotated further. Qualitatively, the interpretation of these experiments is that the $\nu = 2/3$ state undergoes a phase transition from an unpolarized ground state at small tilt angles to a fully polarized state at larger angles. In addition to the tilted-field technique, there are others possibilities to study spin phase transitions. Exploiting the fact that the spin phase transition takes place at a critical ratio $\tilde{g}_{crit}$ of the Zeeman and Coulomb energies E_Z/E_C, is possible to drive this transition conveniently in different ways. A manner consists in the application in-situ of a hydrostatic pressure, which produces changes in the band structure and the spin-orbit coupling. This in turn will lead to a reduction in the magnitude of the electronic g-factor and therefore a lowering of the Zeeman energy [98, 99, 100, 101, 102] which favors the formation of spin-unpolarized states. A second manner to study this transition is by sweeping the electron density maintaining fixed filling factor $\nu = 2/3$. In this case, the functional dependencies of the Zeeman and Coulomb energies on magnetic field or density, allow the possibility to alter $\tilde{g}_{crit}$ and trigger the spin phase transition.

5.1.1 Motivation

Recent experiments carried out in our group have explored in more detail this spin phase transition at $\nu = 2/3$ and uncovered very interesting physics pertaining to the nature of the transition. In particular, the magnetotransport experiments at low temperatures $T < 20mK$ performed by Smet et al. [9, 103] showed that the phase transition between the unpolarized and fully spin polarized $\nu = 2/3$ FQH state is ferromagnetic in nature. This 2/3 spin phase transition is accompanied by hysteresis in transport, which suggests 2D Ising ferromagnetism and domain formation. NMR studies performed by Stern et al. [104] have supported this domain formation. Experiments at higher temperatures $T = 0.4K$ and large currents in narrow quantum wells $(15nm)$ carried out by Kronmüller et al. [105] disclosed an anomalously large increase of the resistance peak at $\nu = 2/3$ [106]. Although at $\nu = 2/3$ there is already a small resistance peak at small currents, it is strongly enhanced when driving larger currents through the sample [107, 108, 109]. Experiments have also showed that the interaction between electrons and the nuclei of the GaAs host plays an important role in the transition regime [110].

Here, we studied the spin transition at $\nu = 2/3$ from a microscopic viewpoint. Using a

single-electron transistor, we follow the evolution of localized states across this spin phase transition by measuring the local electronic compressibility (see Sec. 3.2). These studies were mainly motivated by the transport experiments in Ref. [9, 103], and NMR experiments [104] which suggested a domain formation at the transition.

5.2 Spin Phase Transition at $\nu = 2/3$

5.2.1 Origin of the Spin Transition

The spin phase transitions from an unpolarized to a fully polarized state can be elegantly explained in the composite Fermion (CF) model [4, 3]. As mentioned in chapter 2, composite Fermions are quasi-particles that may be visualized as being composed of one electron and an even number of magnetic flux quanta Φ_0 [17]. This model allows us to understand the FQHE in terms of the IQHE of these quasi-particles. In the composite Fermion language, $\nu = 2/3$ corresponds to having two filled composite Fermion Landau levels (CF-LL). Each CF-LL is characterized by its orbital $(n = 0, 1, 2, \cdots)$ and spin quantum number ($\uparrow$ or $\downarrow$). When $\nu = 2/3$ occurs at low enough magnetic fields, the two occupied levels correspond to the two possible spin orientations of the particles: levels $(0, \uparrow)$ and $(0, \downarrow)$, and the system is unpolarized. As the perpendicular magnetic field $B_\perp$ increases, the separation between these two different spin states increases more rapidly (linearly) than the energy separation to the next orbital level does ($\sqrt{B_\perp}$). Therefore, a coincidence between the spin down state of the lowest CF-LL $(0, \downarrow)$ and the spin up of the second CF-LL $(1, \uparrow)$ will occur, as illustrated in Fig. 5.1. At this coincidence, $B_\perp = B_C$, the system will undergo a quantum phase transition to a fully polarized state.

5.2.2 Signature in Transport for the Spin Transition

At the coincidence of these two spin-resolved levels with different index and opposite spin the quantum Hall effect disappears since the gap closes. Figure 5.2 shows a transport experiment near $\nu = 2/3$. The longitudinal resistance R_L is plotted as a function of $B_\perp$ and $\Delta n_{2/3}$. Here $\Delta n_{2/3}$ is the deviation of the density from the electron density at which the average filling factor in the sample equals $2/3$, $\Delta n_{2/3} = n_{av} - 2/3 \cdot B_\perp/\Phi_0$. When moving along the line $\Delta n_{2/3} = 0$, the resistance is close to zero, then increases and subsequently drops back to

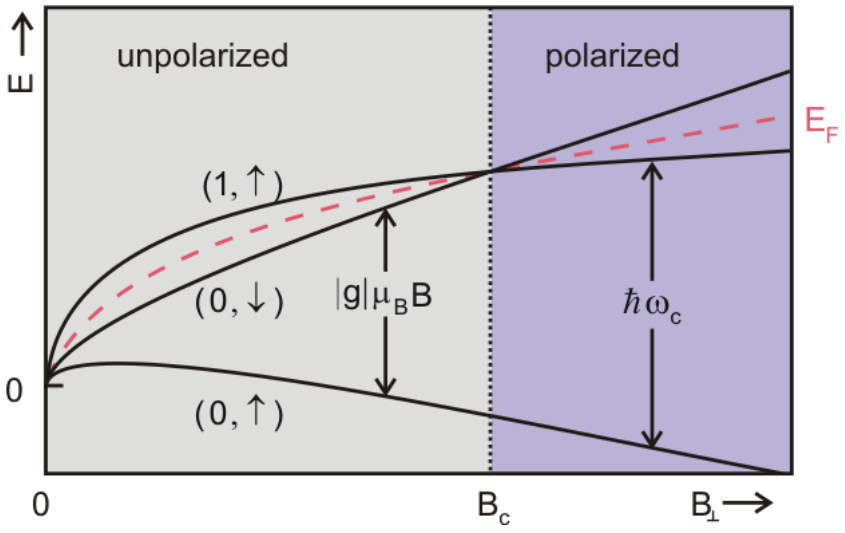

Figure 5.1: Evolution of the composite-fermion Landau level diagram as a function of applied perpendicular magnetic field $B_\perp$ at fixed filling factor $\nu = 2/3$, i.e., when two composite-fermion Landau levels are completely filled. The dashed red curve indicates the Fermi energy, E_F. The composite-fermion Zeeman energy increases linearly with $B_\perp$ while the cyclotron energy of composite-fermions $\hbar\omega_c$ increases only as $\sqrt{B_\perp}$. As a result, a crossing of the $(0, \downarrow)$ and $(1, \uparrow)$ levels occurs as $B_\perp$ is raised. At the coincidence, $B_\perp = B_C$, a quantum phase transition from an unpolarized ground state with an equal number of spin up and spin down composite fermions, to a fully polarized ground state occurs.

zero as $B_\perp$ is increased further. This reentrant behavior is the signature in transport for the spin phase transition [97, 111, 112]. Figure 5.3 illustrates clearly this reentrant behavior. The longitudinal resistance R_L is plotted as a function of $\Delta n_{2/3}$ at the fixed field $B_C = 4.85T$. Also shown in Fig. 5.3 is the hysteretic behavior of the resistance near the transition. The dashed line was taken while sweeping up the density whereas the solid line was recorded during a down sweep of the density. The observation of hysteresis evidences that the spin phase transition is ferromagnetic in nature [9, 103]. Since first-order phase transition may be accompanied by hysteresis, it follows that the spin phase transition may be occurring as a first-order phase transition. In the following section the ferromagnetic character of this quantum phase transition is discussed.

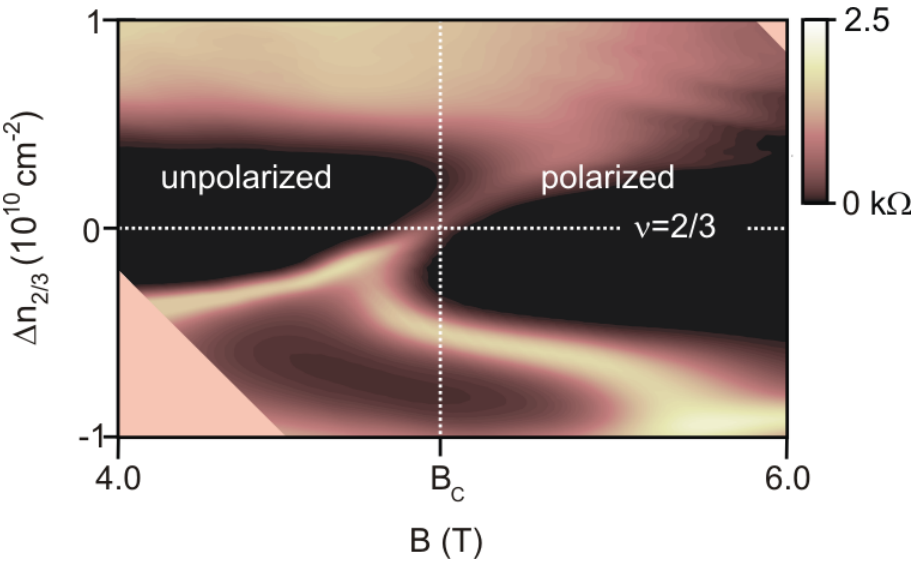

Figure 5.2: Ferromagnetic phase transition with easy-axis anisotropy between the spin-unpolarized and fully spin-polarized $2/3$ fractional quantum Hall state. This plot shows a color map of the longitudinal resistance R_L as a function of magnetic field B and carrier density. The density is measured relative to $n_{2/3} = (2/3)(B/\Phi_0)$. During this experiment R_L was acquired only when the magnetic field was swept down. At B_C and $\nu = 2/3$ the quantum Hall effect disappears and the resistance becomes finite as the system undergoes the spin phase transition.

5.2.3 Ferromagnetic Nature of the Spin Transition

When two Landau levels are brought energetically close to alignment, correlations frequently force a transition of the system towards an ordered many-particle ground state similar to that of a low dimensional ferromagnet [101, 102, 9, 103, 113, 114, 115]. Since the spin phase transition at $\nu = 2/3$ in the composite fermion picture involves the alignment of two composite-fermion Landau levels, one may except that this transition too belongs to the realm of ferromagnetism. At the transition, the degeneracy gives rise to domains of different spin polarizations that are separated by domain walls. In this case, the exchange energy cost for spin misalignment forces quasiparticles initially distributed among the two CF-LL with opposite spin orientation to take on identical spin orientations as one CF-LL overtakes the other. Indeed, the hysteresis in the resistance as seen in Fig. 5.3 is conform with Ising ferromagnetism [101, 9, 114].

To explain the formation of domains with different spin polarization from a phenomeno-

logical viewpoint, one has to consider the effect of the hitherto neglected disorder in the system. On the one hand, we stressed in Section 2.3 that a spatially random disorder potential introduces density fluctuations within the sample. On the other hand, the spin phase transition from an unpolarized to a polarized state takes place at a critical ratio $\tilde{g}_{crit}$ of the Zeeman and Coulomb energies E_Z/E_C and therefore at a critical density or $B_\perp$. Hence, regions within the sample with a lower density than this critical value will be unpolarized while those regions with higher densities will be polarized giving rise to domains or areas with opposite spin configurations.

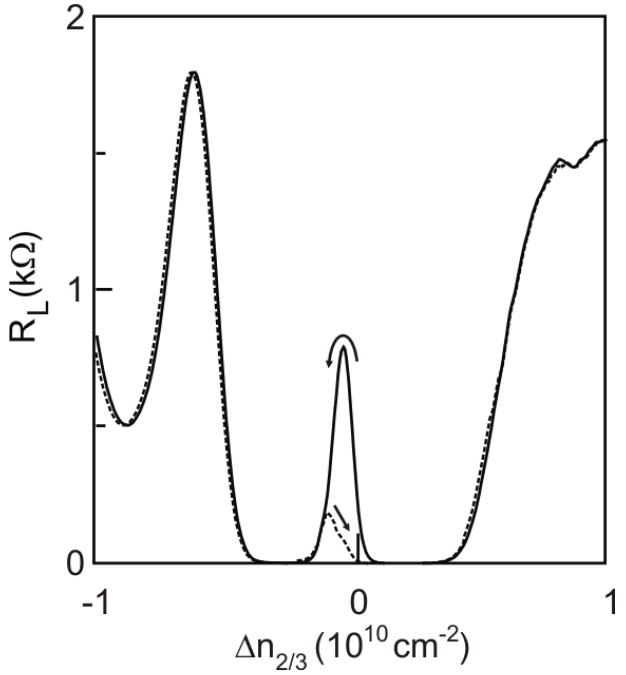

Figure 5.3: The longitudinal resistance R_L in the vicinity of the spin phase transition at $\nu = 2/3$. When comparing data acquired during up sweeps (line dashed) with data recorded during down sweeps (solid line) of the density, hysteresis is observed in R_L.

Hysteresis is usually tied to the physics of domain walls. In Ising quantum Hall ferromagnets, domain wall motion may be hindered by imperfections and different domain configurations may appear as the path to approach the transition is varied. These microscopic differences influence the resistance detected on a macroscopic scale as it is sensitive to the configuration of the medium where the charge-carrying quasiparticles travels through. This likely is the source for the observed hysteresis.

5.3 Microscopic Manifestation of the Spin Phase Transition

Figure 5.4 shows the result of a typical measurement of the compressibility in the vicinity of $\nu = 2/3$ obtained with a single-electron transistor (SET). A description of the SET-technique can be found in Sec. 3.3. The data were taken at a temperature less than 20 mK. As the figure clearly shows, a large set of dark lines departs from the left as well as the right. These lines or spikes in the compressibility run parallel to the horizontal $\Delta n_{2/3} = 0$, marking constant average filling $2/3$. Consistent with the model of localization in the quantum Hall regime outlined in Sec. 2.3, each line corresponds to the evolution in the $(B, \Delta n_{2/3})$-plane of the charging of an individual localized state in a dot or anti-dot close to the SET. Dots or anti-dots correspond to those regions of the sample where the degeneracy of the Landau level being filled is exhausted and the system fails to screen the bare disorder potential. Because the disorder potential is rigid as we tune the B-field, the configuration of dots or anti-dots remains identical at different B-fields and spikes recur at the same $\Delta n_{2/3}$ irrespective of the B-field. The resulting horizontal charging lines continue until the spin phase transition is approached. Once the transition is reached, the gap closes and the important prerequisite for observing localization, namely the existence of a gap, is no longer fulfilled. When this occurs, the screening ability of the system is improved and the localized states disappear. Hence, as the spin transition is approached the localized states or charging lines fade or vanish altogether rather abruptly. The disappearance of localized states represents the microscopic signature of the spin phase transition.

5.3.1 Comparison of the Spectra on both Sides of the Spin Transition

According to the localization picture governed by Coulomb interactions (see Sec. 2.3), the spectrum of localized states depends solely on the bare disorder potential and the presence of a gap. Therefore, the presence of a gap below and above the spin transition should produce identical spectra of localized states on both sides of the transition, as is schematically shown in Fig. 5.5.

Fig. 5.4 allows to compare the localized-state spectrum at fields below the spin transition, namely in the unpolarized regime, with the spectrum at fields above the spin transition, where the electron system is fully spin polarized. Contrary to expectation highlighted in Fig. 5.5, the spectra on both sides of the transition do not match. Some localized states in the unpolarized

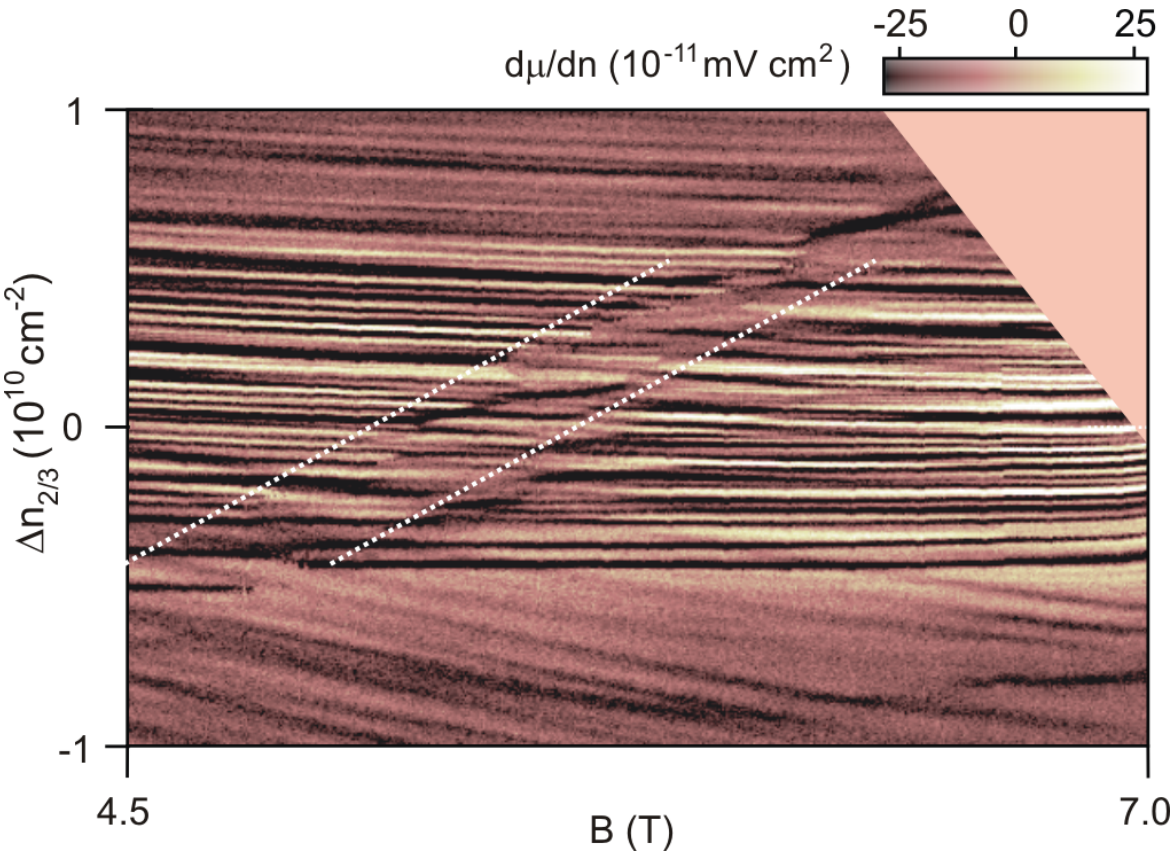

Figure 5.4: Spectra of localized states measured near the $2/3$-spin phase transition. The plot shows a colour map of the local inverse compressibility acquired as function of B field and carrier density (measured relative to $n_{2/3} = (2/3)(B/\Phi_0)$). Data points making up this colour graph were recorded by stepping B from 4.5 to 7 T in 5 mT steps and sweeping the density from high values to low values for each value of the B-field. Dark lines or spikes in the inverse compressibility run parallel to the horizontal $\Delta n_{2/3} = 0$. Each dark line corresponds to the charging of an individual localized state near the SET. The spectra of localized states below the transition and above it are clearly different, suggesting a change in the underlying screened potential across the spin phase transition. Conversely, below and above the transition the spectra are nearly invariant to changes in magnetic field. The white dotted lines serve as guides to the eye. Roughly within a 0.2 T field interval separating these two white lines, the charging lines fade, bend or disappear and the transition takes place. This experiment was carried out in a top-loading dilution fridge with a base temperature < 20 mK.

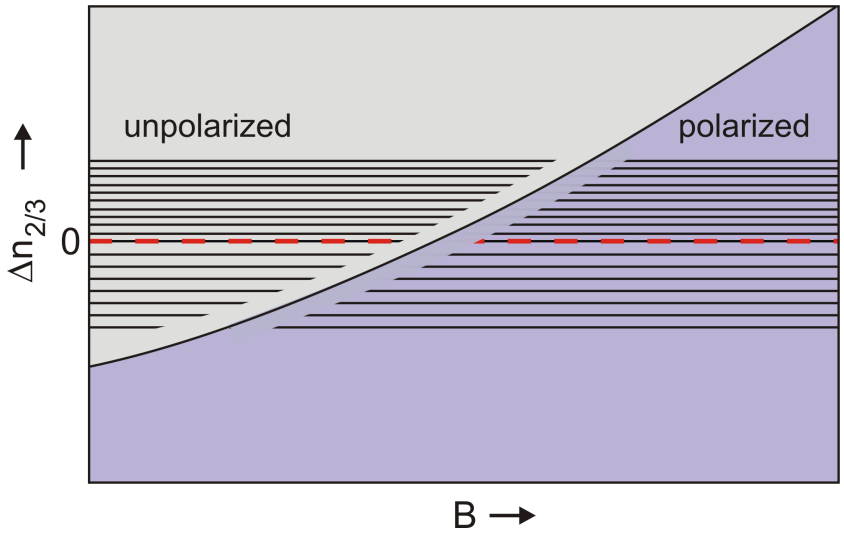

Figure 5.5: Schematic illustration of the expected behaviour for the localized states as a function of B field and carrier density (measured relative to $n_{2/3} = (2/3)(B/\Phi_0)$) on both sides of the spin phase transition at filling factor 2/3 within the screening model of localization. Here, identical sets of horizontal black lines appear at fields below and above the transition. Because the bare disorder potential is not expected to change with B-field, identical spectra are anticipated on both sides of the transition.

side vanish as the spin phase transition is approached, but they do not re-emerge on the other side of the transition. Instead, new localized states at different values of $\Delta n_{2/3}$ appear with no apparent correlation between the new and old values. In addition, the expected gradual disappearance of localized states when the gap closes is not observed. Rather, the spectrum disappears abruptly and is replaced by a new one. This observation cannot be reconciled with the localization picture described in the dot model.

In the localization picture based on non-linear screening, the mismatch between the spectrum of localized states above and below the spin transition suggests that the configuration of anti-dots and dots is modified. However, this would imply a change in the bare disorder potential across the spin transition which is very unlikely. A more likely scenario is that the nature of Coulomb interaction and screening behaviour alters when crossing the transition, because there Landau levels with different spin and orbital quantum numbers become occupied (see Fig. 5.1). A comparison of localized spectra with different spin and orbital quantum numbers can also be made for integer filling factors. However, there the spectra for differ-

ent integer fillings would be collected at substantially different densities or magnetic fields. For instance, in Ref. [42] charging spectra at different integer filling factors were published. There, qualitatively similar spectra were found with only some modifications to them. These modifications may be a result of the change in quantum numbers. The spin phase transition at filling factor $2/3$ provides a unique opportunity of comparing localized-state spectra of different spin and orbital quantum numbers at the same magnetic field and carrier density.

Screening enters in the physics of the spin phase transition because it sets up a density profile that compensates the bare disorder potential when the system is compressible (see section 2.3). It determines the size and shape of the dots and anti-dots, which form when screening breaks down. The discrepancy in the spectra of localized states on both sides of the spin transition suggests that the screening-induced density profile is different well above and well below the transition. Because spikes follow horizontals, we conclude that the screening-induced density profile, and therefore the configuration of dots and anti-dots, remains largely unaltered when staying on the same side of the transition. We conjecture that the difference in the density profile below and above the transition stems from modified screening conditions encountered when Landau levels with different quantum numbers are occupied. Differences in orbital wave function spreading as well as the gap due to exchange enhancement may produce differences in the polarizability of the electronic system [116].

5.4 Hysteresis in Local Compressibility Measurements

The local compressibility shares another important signature of the spin transition with transport data, namely hysteresis. Hysteresis, as already mentioned, is indicative of glassy behaviour in the disordered electron system when it undergoes a ferromagnetic first order quantum phase transition from the unpolarized fractional quantum Hall liquid to the completely polarized fractional quantum Hall liquid. It was also discussed that impediments to free domain walls motion lead to different domain configurations. Since the local electronic compressibility measured by a single-electron transistor (SET) is sensitive to the spatial location of charging events, the microscopic differences in the domain configurations bring about hysteresis depending on the path taken to approach the transition.

Figure 5.6 plots the local compressibility in the magnetic field range where the spin phase transition happens, and compares data acquired during upward sweeps of density n

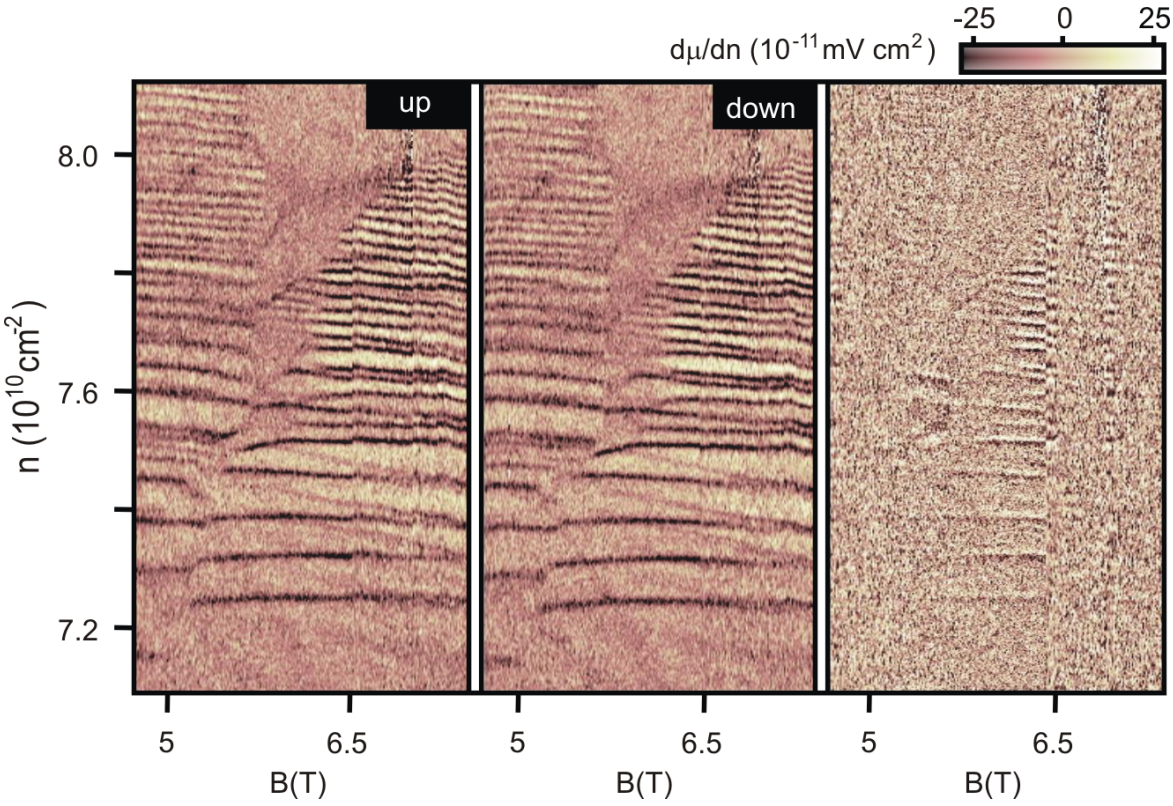

Figure 5.6: Hysteretic behaviour in the local electronic compressibility. These two-dimensional graphs show the local electronic compressibility data acquired during up sweeps (left panel) of density n and down sweeps (middle panel) as well as a subtraction of both (right panel) in the range of magnetic field where the spin phase transition at filling factor $2/3$ happens.

(left panel) with data recorded during downward sweeps (right panel). The right panel was generated by subtracting these two sets of data. In the left and middle panel the spectrum of localized states follows a behaviour very similar to that displayed in Fig. 5.4, i.e., a set of charging lines departs from the left vanishing as the transition region is reached and re-emerging on the other side of the transition. The observation emphasized in the previous section, namely different spectra of localized states on both sides of the transition, is also present here. In general, far away from the spin phase transition, domains will be absent and no hysteretic behaviour is observed in the compressibility deep in the polarized or unpolarized regime. However, in the transition region where domains are relevant, the local compressibility unveils hysteretic behaviour. This observation represents the first microscopic experimental evidence of hysteresis for the spin phase transition at filling factor $2/3$.

For completeness, we note that in transport studies it has been argued that changes in the nuclear spin polarization of the GaAs host can also contribute to hysteretic behaviour. Dynamic nuclear polarization by the externally imposed current, for instance, may produce such changes in the nuclear spin polarization near the transition [105, 117, 107]. The local-compressibility experiments here, have been carried out in the absence of an imposed current.

5.5 Extracting the Typical Domain Size

Unlike transport, which inevitably senses a macroscopic area, local probe studies can focus on only a microscopic area. If the hysteresis is tied to domain formation, it is tempting to argue that if one scales down further and further the active area monitored by the single-electron transistor the hysteresis will disappear when the area probed by the SET is comparable to the typical size of the domains. In order to scale down the size of the sample undergoing the transition, we utilize an electrostatic gating technique. The stationary SET is used as a top gate in addition to its main role as a detector.

By applying a voltage difference, $V_{TG} = V_{SET} - V_{2D}$, between the single-electron transistor (SET) and the two-dimensional electron system, the electron density directly underneath the SET can either be enhanced or depleted compared to the surrounding bulk. Fig. 5.7 illustrates schematically the situation at fixed magnetic field where the electron density underneath the SET is partly depleted. In this case, the externally imposed density difference between the local density n_{local} under the SET and the bulk density n_{bulk}, ensures that the

bulk is still compressible, while in the region underneath the SET the density is closer to filling factor 2/3. The compressibility becomes negligible and the screening in the region underneath the SET is no longer capable of entirely compensating the bare disorder potential. Under these conditions, the bulk will not contribute any $2/3$ compressibility spikes and the observed features will correspond solely to the artificial electron pocket or anti-dot defined by V_{TG}.

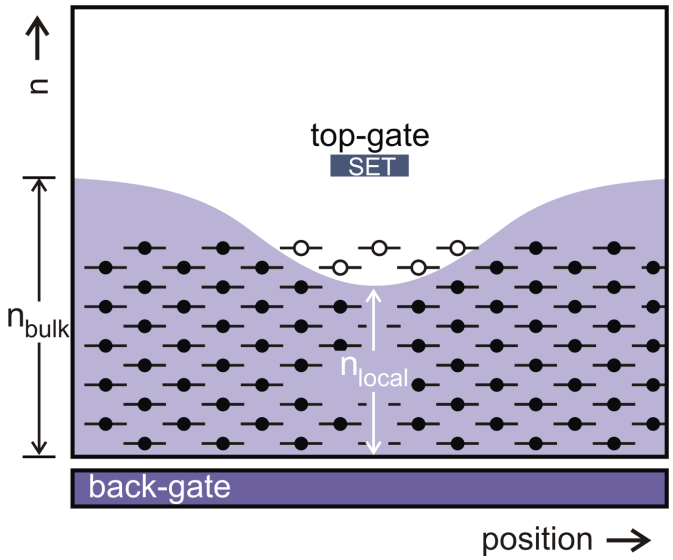

Figure 5.7: Schematic illustration of the spatial density profile in the two-dimensional electron system, when a voltage difference between the SET and the 2DES V_{TG} is applied in such a way that the electron density is lowered directly underneath the SET. The local electron density under the SET is denoted as n_{local}. Far from the SET the electron density is the bulk density n_{bulk}. In contrast to the V_{TG}, which influences the density locally, the V_{BG} affects the density uniformly in space.

An example of compressibility data in the (B, n)-plane when a large V_{TG} bias voltage is applied is shown in Fig 5.8. Under these conditions a pocket of electrons underneath the SET is created by using a $V_{TG} = -120$ mV. During this experiment, in order to maintain a working point of the SET with high sensitivity, V_{TG} was corrected slightly as a function of B. Hence, it is not really constant but the correction is on the 1% level. In this plot, the wide span of n allows to compare the spectrum of localized states of the surrounding regions and the spectrum of localized states of the electron pocket created under the SET.

The set of horizontal lines at densities above $7.5 \times 10^{10}\ cm^{-2}$ corresponds to the spectrum of localized states in the surrounding bulk region. The more distant charging events are detected by the SET, but with diminished amplitude. At densities around $6 \times 10^{10}\ cm^{-2}$, the spectrum of localized states corresponding to the region under the SET is well defined. In the next subsection, a study of the hysteresis at the spin phase transition under these conditions has enabled us to obtain a lower bound for the domain size.

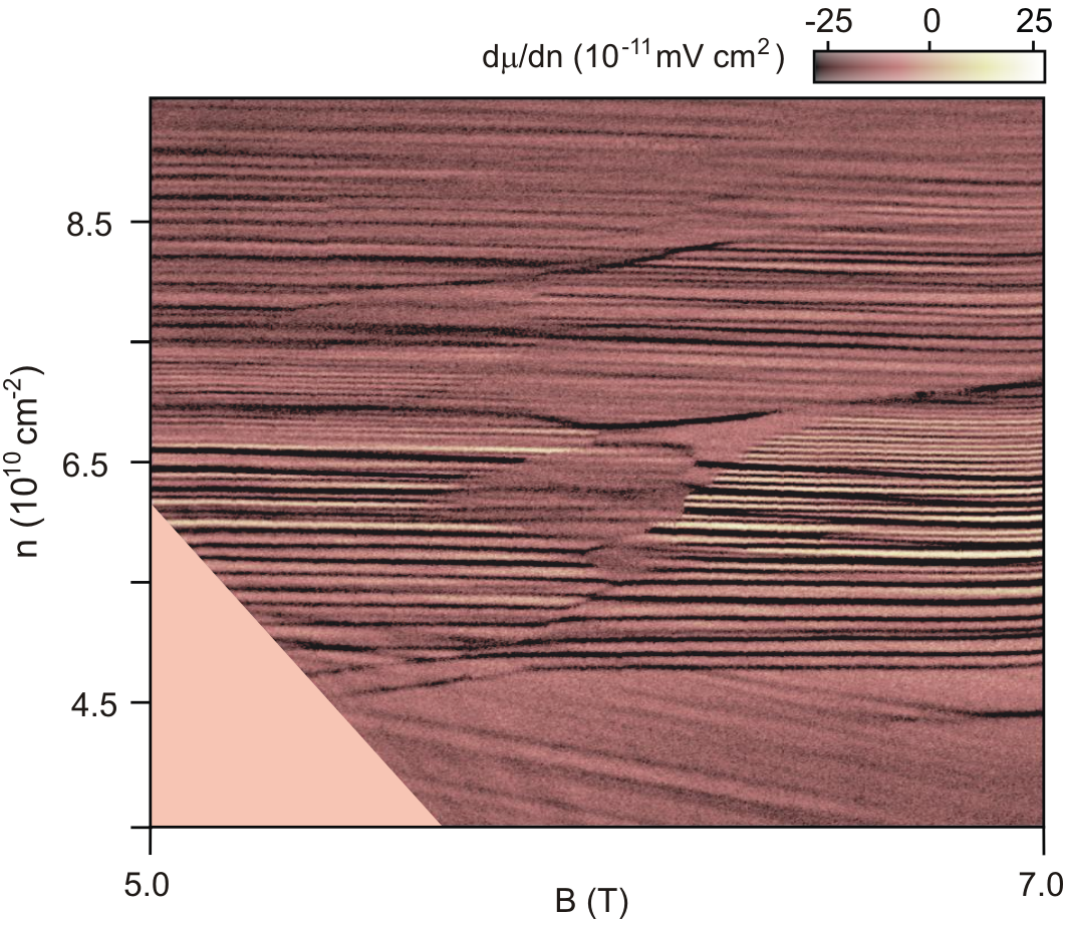

Figure 5.8: Color map of the local electronic compressibility in the (B, n)-plane when a voltage difference is applied between the single-electron transistor and the two-dimensional electron system, $V_{TG} = V_{SET} - V_{2D} = -120$ mV. By spanning a large range of n the spin phase transition at $\nu = 2/3$ can be seen both under the SET as well as in the surrounding bulk. The transition in the surrounding region occurs at higher density, while the transition under the SET occurs at lower densities.

5.5.1 Domain Structure Size

Fig. 5.9 shows a color map of the electronic compressibility in the (B, n)-plane at a bias voltage difference V_{TP} of -120 mV for up and down sweeps of the density. The left and middle panels depict the compressibility when the density is swept up and down respectively. The third panel has been obtained by subtracting the up and down sweeps. The hysteretic behavior has vanished (compare with Fig. 5.6). This observation conforms to our expectations for a glassy system studied on a length scale comparable or smaller than the typical domain size. Because the monitored region is comparable to the SET size (50 nm$\times 500$ nm), it is reasonable to conclude that domain structure occurs on a scale larger than 500 nm.

Finally, the discrepancy between the spectra on either side of the transition survives when zooming in on a small enough area, as in Fig. 5.9, for which the absence of hysteresis signals the absence of domains. This observation substantiates that the mismatch between the localized-spectra on the two sides of the spin transition is unrelated to domain physics near the transition itself.

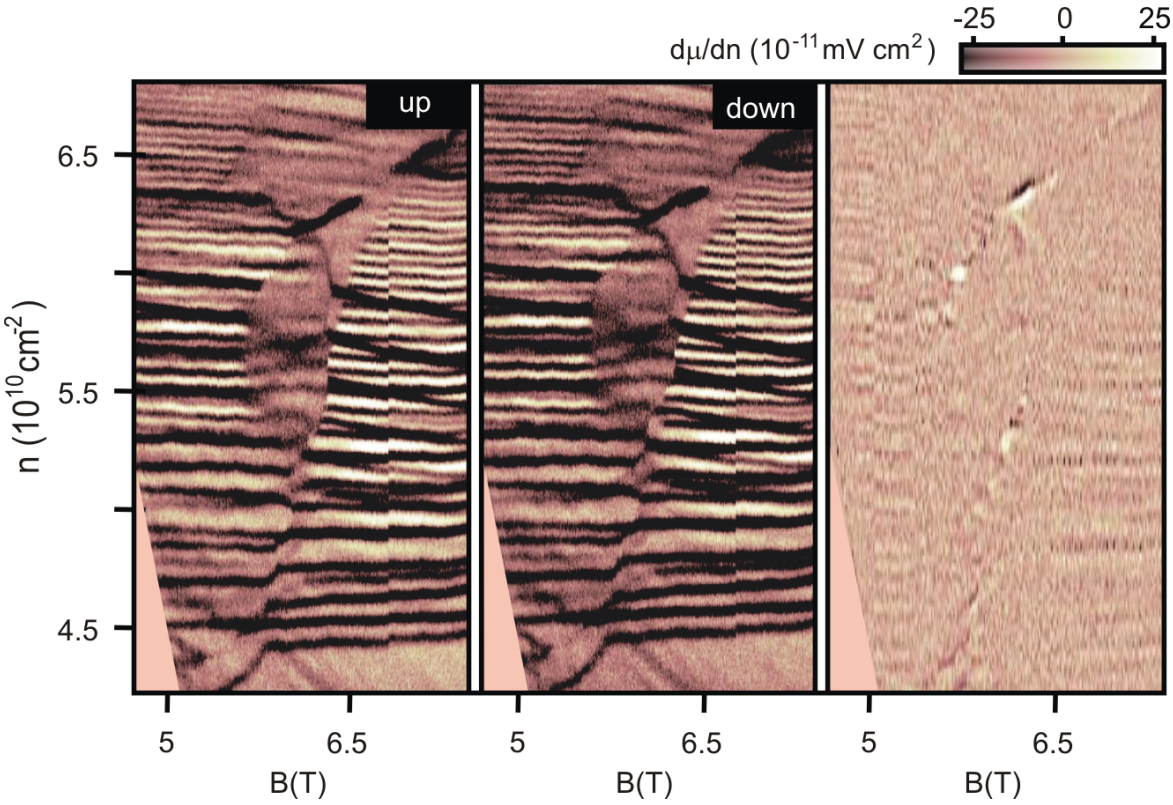

Figure 5.9: Local electronic compressibility data in the (B, n)-plane when a voltage difference between the single-electron transistor and the two-dimensional electron system, $V_{TG} = V_{SET} - V_{2D}$, of -120 mV is applied. Left: The local compressibility data acquired during up sweeps of the density n in the magnetic field regime where the spin phase transition at filling factor $2/3$ happens. Middle: Local electronic compressibility data acquired when the density is swept down. Right: Color map generated by subtracting the sweep up and sweep down data. Hysteresis has vanished.

Chapter 6

Conclusions

This dissertation presents experimental research on phenomena that emerge from electron-electron interactions in the quantum Hall regime. These studies were performed on high quality GaAs-based heterostructures. Magnetotransport studies at very low temperatures (below 20 mK) were carried out on the electronic liquid-crystal phases that appear in partially filled high index Landau levels ($N \geq 2$). Local probe studies, using a stationary single-electron transistor, were performed near the spin phase transition at filling factor $\nu = 2/3$. In the following, we present the conclusions of these studies.

6.1 Electronic Liquid-Crystal Phases

Chapter 4 presents transport measurements carried out in the regime where electronic liquid-crystal (ELC) phases are expected. These experiments were performed on square van der Pauw geometries with side lengths of 90, 180, 300, and 500 μm, which were lithographically defined. The square geometry is preferred over a Hall bar configuration for these studies, because any resistance anisotropy is exponentially enhanced due to current channeling and spreading. These studies are either performed in the presence or absence of a dc current, driven or nondriven conditions respectively.

Transport studies under nondriven conditions

- We observed clear evidence for the existence of the correlated phases in high index Landau levels [13]. Large anisotropic transport appeared around half-fillings and reen-

trant Hall quantization near quarter-fillings of Landau levels with index $N \geq 2$.

- The majority of our transport studies were performed at temperatures less than 20 mK. Usually, at this temperature, the resistance maximum at half-filling gradually decays as the LL index increases. However, at higher temperatures (90 mK) the resistance maximum alternates between large and small values for $(2N + 1/2)$ $(2N + 3/2)$ filling, respectively. We explain this observation by differences in the barrier height for tunneling across the stripes.

Transport studies under driven conditions

- We have observed a stabilizing effect on the orientation of the anisotropic phase at half filling when dc current drive and easy direction coincide. We speculate that this stabilizing influence of dc current is linked to a suppression of the transverse shape fluctuations of the nematic phase in the ELC picture.

- We found some evidence for a reordering in the anisotropic phase around half filling. The easy direction is rotated to point along the dc current direction. If initially the dc current is perpendicular to easy direction, by increasing the dc current they align. Furthermore, we found evidence that indicate that the dc current flowing through the anisotropic correlated phase around half-filling could be triggering the reorientation of this phase.

- We have found that a dc current drive also induces anisotropic transport near one-quarter and three-quarter filling consistent with stripe order. The result favors the stripe-crystal phase rather than the isotropic bubble phase to describe the system near quarter fillings in the high Landau levels.

- We have found evidence suggesting that the depinning of the stripe-crystal phase is due to the dc Hall electric field. The depinned phase exhibits anisotropy. Initially the easy direction of the emergent anisotropic phase coincides with the direction of the dc Hall electric field, i.e., perpendicular to the dc current direction. At larger dc-current, eventually easy-direction and dc-current align in a similar fashion as the reordering that takes place near half-filling.

Based on these observations, we can say that a dc current drive plays the role of an external breaking symmetry field. The data provide compelling evidence for the liquid crystal picture of the collective states in high Landau levels.

6.2 Spin Phase Transition at Filling Factor 2/3

In this section we present the conclusions derived from the local probe studies performed near the spin phase transition at filling factor $\nu = 2/3$. Although this transition has been investigated using other techniques before, this work is the first microscopic study.

- We were able to probe and follow the evolution of individual localized states as one crosses the spin phase transition by measuring the local electronic compressibility. Furthermore, we observed that the localized states appear in a band parallel to the line of constant filling factor $\nu = 2/3$.

- We observed that the spectra of localized states below and above the spin transition are different. According to the current understanding of localization in which screening plays a crucial role, this discrepancy between spectra either implies that the bare disorder potential varies with density or the details of screening change. Since it is unlikely that the bare disorder potential changes, modified screening behavior when Landau levels with different spin quantum numbers become populated is the most likely explanation.

- We have observed hysteretic behavior accompanying the spin transition when comparing data acquired during up sweeps of density with data acquired during down sweeps. Hysteresis is indicative of domains formation.

- Using electrostatic gating we were able to vary the size of the sample undergoing the phase transition. For submicrometer dimensions the hysteresis disappeared. We can conclude that the domain size is in excess of 500 nm.

- We found evidence that indicate that the mismatch between the localized-spectra on either side of the transition is unrelated to domain physics near the transition. This relies on the fact that the discrepancy between the spectra on the two sides of the spin

transition survives when zooming in on an area where the absence of hysteresis signals the absence of domains.

6.3 Outlook

The correlated phases in high Landau levels (HLL) have not been investigated at a microscopic level. Measurements with a single-electron transistor mounted on the tip of a scanning probe microscope as well as scanning tunneling microscopy are among the most promising techniques to accomplish this task.

Measurements of the Hall potential distribution in the quantum Hall regime are very useful to infer the current distribution within the two-dimensional electron system. In the course of this work, experiments using inner ohmic contacts to measure the Hall voltage distribution in the correlated phases in HLL were carried out but require improvements. To eliminate the contribution of the dc-Hall voltage from the dc-current flowing through the edge channels of the completely filled levels, it is necessary to measure the Hall voltage distribution at a temperature high enough that the correlated phases are absent. A substraction of the results obtained at high and low temperature may provide valuable additional information on the reordering and the accompanied changes in the current distribution.

Appendix A

Sample Preparation

A.1 Materials

All the devices used in this thesis were defined by optical lithography on high quality AlGaAs/GaAs heterostructures grown with molecular beam epitaxy by collaborators at Bell Labs (USA), the Walter Schottky Institute (Germany), and the Weizmann Institute of Science (Israel).

The data presented in this thesis were acquired from the samples grown at Bell labs (chapter 4) and the Walter Schottky Institute (chapter 5). However, the samples fabricated at the Weizmann Institute were crucial in the first stages of the investigations described in chapter 4.

The following table shows the most important characteristics of the material used.

Wafer Name	Density	Mobility	Laboratory
LP8-9-01.2	$2.5 \cdot 10^{11}\ \mathrm{cm}^{-2}$	$18 \cdot 10^{6}\ \mathrm{cm}^{2}/\mathrm{Vs}$	Bell Labs
VU4-97	$2.1 \cdot 10^{11}\ \mathrm{cm}^{-2}$	$10 \cdot 10^{6}\ \mathrm{cm}^{2}/\mathrm{Vs}$	Weizmann Institute
W11-27-01.1	$0.8 \cdot 10^{11}\ \mathrm{cm}^{-2}$	$- \cdot 10^{6}\ \mathrm{cm}^{2}/\mathrm{Vs}$	Walter Schottky

A.2 Optical lithography

This section outlines the steps used to prepare the devices in the experiments presented in chapter 4.

A.2.1 Mesa definition

The mesa is defined during the following steps:

1. Clean sample, first with acetone, then with propanol.
2. Coat the sample with photoresist. Apply a few drops of Shipley S1805 photoresist on the sample previously adjust on the plate of the spinner, and spin for 30 seconds at 4.5 krpm.
3. Bake for 2 seconds on top of a hotplate set to 90 °C.
4. Expose the photoresist to 6 seconds of UV light with the mask aligner.
5. Develop photoresist. Immerse and shake the sample in AZ 726 developer for 35 seconds. Then rinse in a stream of deionized water for about 3 minutes. Blow dry well with dry N_2. In this step, exposed areas of the photoresist are removed.
6. Prepare the etch solution. The etch solution is prepared by mixing together the following chemical components:
   - 50 ml of H_2O
   - 1 ml of H_2O_2
   - 50 ml of H_3PO_4

   Stir the etch solution using a magnetic stirrer until the temperature of the solution is between 20-25 °C.
7. Etch the exposed areas. Immerse the sample in the etch solution by using a Kimex dish for the appropriate amount of time. The typical etch rate of the solution is 250 nm/min).
8. Clean the sample, first with deionized water, then acetone, then with propanol. Finally, blow dry sample with N_2.

A.2.2 Electrical contacts

Electrical contacts to the 2DES are made by alloying a gold-germanium-nickel (Au/Ge/Ni) sequence of metals, which have been deposited on the top of the mesa with thermal evaporation. The process is carried out following the next steps:

1. Coat the sample with photoresist AZ5214E and spin for 30 seconds at 6 krpm.
2. Bake for 4 seconds on top of a hotplate set to 90 °C.
3. Expose the photoresist for 60 seconds with UV light in the mask aligner.
4. Bake for 60 seconds on top of a hotplate set to 120°C.
5. Expose the sample for 70 seconds without mask (flood exposure).
6. Develop photoresist. Immerse and shake the sample in AZ 726 developer for 40 seconds. Rinse in a stream of deionized water and blow dry the sample with N_2.
7. Clean the sample before introducing it into the evaporator in the following manner:
   - Clean the sample in an O_2 plasma for 30 seconds.
   - Immerse the sample in Semicoclean for 2 minutes.
   - Immerse the sample in HCl for 5 seconds.
   - Immerse the sample in deionized water for 1 second.
   - Blow dry the sample with N_2
8. Evaporate contact materials. The metals (Au/Ge/Ni) are evaporated with the following thickness and rates:
   - 320 nm of Au at a rate of ≈ 0.2 nm/s
   - 160 nm of Ge at a rate of ≈ 0.2 nm/s
   - 120 nm of Ni at a rate of ≈ 0.1 nm/s
9. Alloying the contact material in an oven with forming gas at a pressure of 300 mbar, as follows:
   - 370 °C for 120 seconds, without gas flow.

- 440 °C for 120 seconds, without gas flow.
- rapid cool down to room T, with gas flow.

A.2.3 Bonding pads

The bond pads facilitate the wire-bonding to the sample. The pads are made of Cr/Au and are deposited as follows:

1. Coat the sample with photoresist AZ5214E and spin for 30 seconds at 6 krpm.
2. Expose the photoresist with UV light in the mask aligner.
3. Develop photoresist.
4. Deposit metal. The metals (Cr/Au) are evaporated in the following order:
   - 20nm of Cr at a rate of ≈ 0.1 nm/s
   - 100nm of Au at a rate of ≈ 0.2 nm/s
5. Lift off.

Bibliography

[1] D. C. Tsui, H. L. Störmer, and A. C. Gossard, Phys. Rev. Lett. **48**, 1559 (1982).

[2] R. B. Laughlin, Phys. Rev. Lett. **50**, 1395 (1983).

[3] S. Das Sarma and A. Pinczuk (eds),*Perspectives in Quantum Hall Effects*, (John Wiley & Sons, New York, 1997).

[4] O. Heinonen (ed), *Composite Fermions: A Unified View of the Quantum Hall Regime*, (World Scientific, Singapore, 1998).

[5] J. P. Eisenstein and H. L. Störmer, Science **248**, 1510 (1990).

[6] P. K. Lam and S. M. Girvin, Phys. Rev. B **30**, 473 (1984).

[7] D. Levesque, J. J. Weis, and A. MacDonald, Phys. Rev. B **30**, 1056 (1984).

[8] E. Fradkin and S. Kivelson, Phys. Rev. B **59**, 8065 (1999).

[9] J. H. Smet, R. A. Deutschmann, W. Wegscheider, G. Abstreiter, and K. von Klitzing, Phys. Rev. Lett. **86**, 2412 (2001).

[10] B. I. Halperin, Helv. Phys. Acta **56**, 75 (1983).

[11] J.P. Eisenstein, K. B. Cooper, L.N. Pfeiffer, and K.W. West, Phys. Rev. Lett. **88**, 076801 (2002).

[12] J. S. Xia, W. Pan, C. L. Vicente, E. D. Adams, N. S. Sullivan, H. L. Stormer, D. C. Tsui, L. N. Pfeiffer, K. W. Baldwin, and K. W. West, Phys. Rev. Lett. **93**, 176809 (2004).

[13] M.P. Lilly, K.B. Cooper, J.P. Eisenstein, L.N. Pfeiffer, and K.W. West, Phys. Rev. Lett. **82**, 394 (1999).

[14] R.R. Du, D.C. Tsui, H.L. Stormer, L.N. Pfeiffer, K.W. Baldwin, and K.W. West, Sol. Stat. Comm. **109**, 389 (1999).

[15] A.A. Koulakov, M.M. Fogler, and B.I. Shklovskii, Phys. Rev. Lett. **76**, 499 (1996).

[16] K. S. Novoselov, Z. Jiang, Y. Zhang, S. V. Morozov, H. L. Stormer, U. Zeitler, J. C. Maan, G. S. Boebinger, P. Kim, and A. K. Geim, Science **315**, 1379 (2007).

[17] J. K. Jain, *Composite Fermions*, (Cambridge University Press, New York, 2007).

[18] C. Weisbuch and B. Vinter, *Quantum Semiconductor Structures: Fundamentals and Applications*, (Academic, San Diego CA, 1991).

[19] A. Y. Shik, *Quantum Wells: Physics and Electronics of Two-Dimensional Systems*, (World Scientific Publishing, Singapore, 1997).

[20] E. H. C. Parker, *The Technology and Physics of Molecular Beam Epitaxy*, (Plenum, New York, 1985).

[21] M. R. Melloch, Thin Solid Films **231**, 74 (1993).

[22] H. L. Störmer, R. Dingle, A. C. Gossard, W. Wiegmann, and M. D. Sturge, Solid State Commun. **29**, 705 (1979).

[23] J. H. Davies, *The Physics of Low-Dimensional Semiconductors*, (Cambridge University Press, Cambridge, 1998).

[24] S. Ilani, A. Yacoby, D. Mahalu, and H. Shtrikman, Science **292**, 1354 (2001).

[25] K. v. Klitzing, G. Dorda, and M. Pepper, Phys. Rev. Lett. **45**, 494 (1980).

[26] H. Kamimura and H. Aoki, *The Physics of Interacting Electrons in Disorder Systems*, (Clarendon Press, Oxford, 1989).

[27] V. F. Gantmakher, *Electrons and Disorder in Solids*, (Clarendon Press, Oxford, 2005).

[28] S. Trugman, Phys. Rev. B **27**, 7539 (1983).

[29] M. Büttiker, Phys. Rev. B **38**, 9375 (1988).

[30] R. Landauer, IBM-J. Res. Dev. **1**, 223 (1957).

[31] Klaus von Klitzing, Physica B **184**, 1 (1993).

[32] Horst Ludwig Störmer, Rev. Mod. Phys. **71**, 875 (1998).

[33] H. Bruus and K. Flensberg, *Many-Body Quantum Theory in Condensed Matter Physics*, (Oxford University Press, New York, 2004).

[34] P. W. Anderson, *Basic Notions of Condensed Matter Physics*, (Benjamin, London, 1984).

[35] X.-G. Wen and Q. Niu, Phys. Rev. Lett. **41**, 9377 (1990).

[36] X.-G. Wen, Advances in Physics **44**, 405 (1995).

[37] D. Yoshioka, *The Quantum Hall Effect*, (Springer-Verlag, Berlin, 1998).

[38] F.D.M. Haldane, Phys. Rev. Lett. **51**, 605 (1983).

[39] B. I. Halperin, Phys. Rev. Lett. **52**, 1582 (1984).

[40] R. B. Laughlin, Surface Sci. **142**, 163 (1984).

[41] J. J. Sakurai, *Modern Quantum Mechanics*, (Addison-Wesley Publishing, New York, 1994).

[42] S. Ilani, J. Martin, E. Teitelbaum, J. H. Smet, D. Mahalu, V. Umansky, and A. Yacoby, Nature **427**, 328 (2004).

[43] T. A. Fulton and G. J. Dolan, Phys. Rev. Lett. **59**, 109 (1987).

[44] G. K. White and P.J. Messon, *Experimental Techniques in Low-Temperature Physics*, (Clarendon Press, Oxford, 2002).

[45] A. L. Fetter and J. D. Walecka, *Quantum Theory of Many-Particle Physics*, (McGraw-Hill, New York, 1971).

[46] J. P. Eisenstein, L. N. Pfeiffer, and K. W. West, Phys. Rev. B **50**, 1760 (1994).

[47] S. Shapira, U. Sivan, P. M. Solomon, E. Buchstab, M. Tischler, and G. Ben Yoseph, Phys. Rev. Lett. **77**, 3181 (1996).

[48] A. Yacoby, H. F. Hess, T. A. Fulton, L. N. Pfeiffer, and K. W. West, Solid State Commun. **111**, 1 (1999).

[49] N. W. Ashcroft and N. D. Mermin, *Solid State Physics*, (W. B. Saunders, Philadelphia, 1976).

[50] G. D. Mahan, *Many-Particle Physics*, (Kluwer Academic/Plenum Publishers, New York, 2000).

[51] D. Averin and K. K. Likharev, J. Low. Temp. Phys. **62**, 345 (1986).

[52] Y. Y. Wei, J. Weis, K. v. Klitzing, and K. Eberl, Appl. Phys. Lett. **71**, 2514 (1997).

[53] Y. Y. Wei, J. Weis, K. v. Klitzing, and K. Eberl, Phys. Rev. Lett. **81**, 1674 (1998).

[54] J. M. Tranquada, B. J. Sternlieb, J. D. Axe, Y. Nakamura, and S. Uchida, Nature **375**, 561 (1995).

[55] J. M. Tranquada, H. Woo, T. G. Perring, H. Goka, G. D. Gu, G. Xu, M. Fujita, and K. Yamada, Nature **429**, 534 (2004).

[56] D. Reznik, L. Pintschovius, M. Ito, S. Ikubo, M. Sato, H. Goka, M. Fujita, K. Yamada, G. D. Gu, and J. M. Tranquada, Nature **440**, 1170 (2006).

[57] M. Seul and D. Andelman, Science **267**, 476 (1995).

[58] S. A. Kivelson and V. J. Emery, Synth. Met. **80**, 151 (1996).

[59] R. Moessner and J. Chalker, Phys. Rev. B **54**, 5006 (1996).

[60] M. M. Fogler, *High Magnetic Fields Applications in Condensed Matter Physics and Spectroscopy*, Edited by C. Berthier, L. -P. Levy and G. Martinez (Springer-Verlag, Berlin, 2002).

[61] R. L. Willett, J. W. P. Hsu, D. Natelson, K. W. West, and L. N. Pfeiffer, Phys. Rev. Lett. **87**, 126803 (2001).

[62] K.B. Cooper, M.P. Lilly, J.P. Eisenstein, T. Jungwirth, L.N. Pfeiffer, and K.W. West, Solid State Commun. **119**, 89 (2001).

[63] K. B. Cooper, J. P. Eisenstein, L. N. Pfeiffer, and K. W. West, Phys. Rev. Lett. **92**, 026806 (2004).

[64] M.P. Lilly, K.B. Cooper, J.P. Eisenstein, L.N. Pfeiffer, and K.W. West, Phys. Rev. Lett. **83**, 824 (1999).

[65] W. Pan, J.-S. Xia, V. Shvarts, D. E. Adams, H. L. Stormer, D. C. Tsui1, L. N. Pfeiffer, K. W. Baldwin, and K. W. West, Phys. Rev. Lett. **83**, 3530 (1999).

[66] J. Zhu, W. Pan, H. L. Stormer, L.N. Pfeiffer, and K. W. West, Phys. Rev. Lett. **88**, 116803 (2002).

[67] J.P. Eisenstein, Solid State Comm. **117**, 123 (2001).

[68] E.H. Reyazi, F.D.M. Haldane, and Kun Yang, Phys. Rev. Lett. **83**, 1219 (1999).

[69] S. A. Kivelson, E. Fradkin, and V. J. Emery, Nature **393**, 550 (1998).

[70] C. Wexler and O. Ciftja, Int. J. Mod. Phys. B **20**, 747 (2006).

[71] H. Fukuyama, P.M. Platzman, and P.W. Anderson, Phys. Rev. B **19**, 5211 (1979).

[72] E.P. Wigner, Phys. Rev. **46**, 1002 (1934).

[73] N. Shibata and D. Yoshioka, Phys. Rev. Lett. **86**, 5755 (2001).

[74] G. F. Giuliani and G. Vignale, *Quantum Theory of the Electron Liquid*, (Cambridge University Press, Cambridge, 2005).

[75] S.H. Simon, Phys. Rev. Lett. **83**, 4223 (1999).

[76] C. Wexler and A. T. Dorsey, Phys. Rev. B **64**, 115312 (2001).

[77] V. J. Emery, S. A. Kivelson, and J. M. Tranquada, Proc. Natl. Acad. Sci. U.S.A **96**, 8814 (1999).

[78] P. M. Chaikin and T. C. Lubensky, *Principles of Condensed Matter Physics*, (Cambridge University Press, New York, 1995).

[79] P. G. de Gennes and J. Prost, *The Physics of Liquid Crystals*, (Oxford University Press, New York, 1995).

[80] D. C. Mattis, *The Many Body Problem*, (World Scientific Publishing Co., 1992).

[81] N. Nagaosa, *Quantum Field Theory in Condensed Matter Physics*, (Springer-Verlag, Berlin Heidelberg, 1999).

[82] K. B. Cooper, *New Phases of Two-Dimensional Electrons in Excited Landau Levels*, (PhD Thesis, California Institute of Technology, Pasadena CA, 2003).

[83] S.M. Girvin, Phys. Rev. B **29**, 6012 (1984).

[84] J. Göres, *Correlations Effects in 2-Dimensional Electron Systems: Composite Fermions and Electron Liquid Crystals*, (PhD Thesis, Max-Planck-Insitut für Festkörperforschung, Stuttgart, 2004).

[85] C. J. Olson Reichhardt, C. Reichhardt, I. Martin, and A. R. Bishop, Physica D **193**, 303 (2004).

[86] K.B. Cooper, M.P. Lilly, J.P. Eisenstein, L.N. Pfeiffer, and K.W. West, Phys. Rev. B **60**, R11285 (1999).

[87] G. Grüner, Rev. Mod. Phys. **60**, 1129 (1988).

[88] G. Nachtwei, Physica E **4**, 79 (1999).

[89] R.M. Lewis, P.D. Ye, L.W. Engel, D.C. Tsui, L.N. Pfeiffer, and K.W. West, Phys. Rev. Lett. **89**, 136804 (2002).

[90] A.H. MacDonald and M.P.A. Fisher, Phys. Rev. B **61**, 5724 (2000).

[91] G. Müller, D. Weiss, K. von Klitzing, P. Streda, and G. Weimann, Phys. Rev. B **51**, 10236 (1995).

[92] T. Chakraborty and P. Pietiläinen, *The Quantum Hall Effects*, (Springer-Verlag, Berlin, 1995).

[93] Z. F. Ezawa, *Quantum Hall Effects*, (World Scientific, Singapore, 2000).

[94] X. C.Xie, Y.Guo, and F. C. Zhang, Phys. Rev. B **40**, R3487 (1989).

[95] T. Chakraborty and P. Pietiläinen, Phys. Rev. B **41**, 10862 (1990).

[96] I. V. Kukushkin, K. von Klitzing, and K. Eberl, Phys. Rev. Lett. **82**, 3665 (1999).

[97] J. P. Eisenstein, H. L. Störmer, L. N. Pfeiffer, and K. W. West, Phys. Rev. B **41**, R7910 (1990).

[98] N. G. Morawicz, K. W. J. Barnham, A. Briggs, C. T. Foxon, J. J. Harris, S. P. Najada, J. C. POrtal, and M. L. Williams, Semicond. Sci. Technol. **8**, 333 (1993).

[99] S. Holmes, D. K. Maude, M. L. Williams, J. J. Harris, J. C. Portal, K. W. J. Barnham, and C. T. Foxon, Semicond. Sci. Technol. **9**, 1549 (1994).

[100] W. Kang, J. B. Young, S. T. Hannahs, E. Palm, K. L. Campman, and A. C. Gossard, Phys. Rev. B **56**, R12776 (1997).

[101] H. Cho, J. B. Young, W. Kang, K. L. Campman, A. C. Gossard, M. Bichler, and W. Wegscheider, Phys. Rev. Lett. **81**, 2522 (1998).

[102] J. Eom, H. Cho, W. Kang, K. L. Campman, A. C. Gossard, M. Bichler, and W. Wegscheider, Science **289**, 2320 (2000).

[103] J. H. Smet, R. A. Deutschmann, F. Ertl, W. Wegscheider, G. Abstreiter, and K. von Klitzing, Nature **415**, 281 (2002).

[104] O. Stern, N. Freytag, A. Fay, W. Dietsche, J. H. Smet, K. von Klitzing, D. Schuh, and W. Wegscheider, Phys. Rev. B **70**, 75318 (2004).

[105] S. Kronmüller, W. Dietsche, J. Weis, K. von Klitzing, W. Wegscheider, and M. Bichler, Phys. Rev. Lett. **81**, 2526 (1998).

[106] G. Davies, Physics World **September**, 20 (1999).

[107] S. Kraus, O. Stern, J. G. S. Lok, W. Dietsche, K. von Klitzing, M. Bichler, D. Schuh, and W. Wegscheider, Phys. Rev. Lett. **89**, 266801 (2003).

[108] S. Kraus, *Untersuchung von Wechselwirkungen in zweidimensionalen Elektronsystemen mit Transport- und Drag-Messungen*, (PhD Thesis, Max-Planck-Insitut für Festkörperforschung, Stuttgart, 2003).

[109] O. I. Stern, *Spin Phenomena in the Fractional Quantum Effect: NMR and Magnetotransport Studies*, (PhD Thesis, Max-Planck-Insitut für Festkörperforschung, Stuttgart, 2005).

[110] S. Kronmüller, W. Dietsche, K. von Klitzing, G. Denninger, W. Wegscheider, and M. Bichler, Phys. Rev. Lett. **82**, 4070 (1999).

[111] L. W. Engel, S. W. Hwang, T. Sajoto, D .C. Tsui, and M. Shayegan, Phys. Rev. B **45**, 3418 (1992).

[112] R. G. Clark, *Localization and Confinement of Electrons in Semiconductors*, F. Kuchar, H. Heinrich, G. Bauer, Eds. (Springer-Verlag, Berlin, 1990), pp. 168-182.

[113] G. F. Giuliani and J. J. Quinn, Phys. Rev. B **31**, 628 (1985).

[114] Vicenzo Piazza, Vittorio Pellegrini, Fabio Beltram, Werner Wegscheider, Tomas Jungwirth, and Allan MacDonald, Nature **402**, 638 (1999).

[115] E. P. DePoortere, E. Tutuc, S. J. Papadakis, and M. Shayegan, Science **290**, 1546 (2000).

[116] I. L. Aleiner and L. I. Glazman, Phys. Rev. B **52**, 11296 (1995).

[117] K. Hashimoto, K. Muraki, T. Saku, and Y. Hirayama, Physica B **298**, 191 (2001).

Acknowledgments

It is with pleasure and sincere gratitude that I acknowledge the help, support and encouragement that I have received during the realization of this thesis. In particular I would like to thank the following people:

- Prof. Klaus von Klitzing, for the opportunity to work on this exciting project and to be a member of his research group, as well as for being always open to discussions. His way of discussing problems and results have had a strong and positive influence on me.

- Dr. Jurgen Smet, for introducing me in the field of the electron correlation phenomena. His help and support during the time that I spent in the laboratory and the critical reading of the manuscript were crucial for the completion of this work.

- Prof. Daniela Pfannkuche, Prof. Detlef Heitmann, and Dr. Alexander Chudnovskiy, who kindly accepted to be part of the distinct committees of my graduation at the University of Hamburg. A special thanks goes to Prof. Pfannkuche for being my contact in Hamburg and my guide throughout the graduation process.

- Prof. Amir Yacoby (now at Harvard University) and all the members of his group at the Weizmann Institute of Science in Israel. In particular I would to thank Dr. Basile Verdene for introducing me in the use of single electron transistors.

- Dr. Jörn Göres, for his help during the early stage of this work and for a lot of useful technical hints.

- Dr. Lütz Höppel, for giving me a first insight in the world of cryostats and for a lot of helpful discussions.

- Dr. Martin Geisler, for helping me in many software problems.

- Monika Riek for helping me with the processing of samples.
- Manfred Schmid, Ingo Hagel, and Walter Schmidt for their excellent technical support.
- Frank Schartner for helping me with tricky-bonding samples.
- Lars Tiemann for helping me in the German translation of the abstract of this thesis.
- All my colleagues in the von Klitzing's group as well as from the institute that directly or indirectly help me during the realization of this thesis.
- Dr. Hans-Georg Libuda, for opening the first door into the Max Planck Institute, by inviting me to the interview and for his help to attain the IMPRS fellowship.
- Ruth Jenz, for helping me with all the paperwork necessary for my graduation, and mainly for her nice conversation.
- Ulrike Waizmann, for all the nice outing, dinners, conversations and the time we spent together, but most of all for being always a trusting friend.
- Dr. Omar Stern, for his friendship and for helping me to overcome uneasy times.
- I want to acknowledge the loss of a great man, Gildardo Acosta Ruiz. I will miss his wisdom and brilliance. My earnest appreciation for always pushing me to go beyond a "quasi", and because he never failed to see the humor of any situation.
- My gratitude also goes to my Sisters and Brothers, for their never ending support and for being my inexhaustible source of inspiration during all these years.
- My profoundest thanks to my incomparable Little Sunflower Girl, with whom I am forever strongly correlated. Her love and patience illuminated moments in which all the lights seemed to be off. She has lived this story with me, and for that I am deeply grateful. To her I dedicate this thesis.
- A special thanks goes to my mother, Genoveva Corrales, whose love and blessings have given me courage and confidence to grow beyond comfortable boundaries. Gracias mamá por estar siempre a mi lado aun en la distancia y por ser mi talismán infalible. A ti dedico esta tésis.

This work was supported by the International Max Planck Research School for Advanced Materials (IMPRS-AM), and the German-Israeli Foundation.